REACTION-BASED MODELING AND CONTROL OF AN ELECTRICALLY BOOSTED DIESEL ENGINE

By

Yifan Men

A DISSERTATION

Submitted to
Michigan State University
in partial fulfillment of the requirements
for the degree of

Mechanical Engineering – Doctor of Philosophy

2019

ABSTRACT

REACTION-BASED MODELING AND CONTROL OF AN ELECTRICALLY BOOSTED DIESEL ENGINE

By

Yifan Men

This dissertation presents the reaction-based modeling of diesel combustion and model-based control of diesel engine air path.

The dissertation first presents a control-oriented reaction-based diesel combustion model that predicts the time-based rate of combustion, in-cylinder gas temperature and pressure over one engine cycle. The model, based on the assumption of a homogeneous thermodynamic combustion process, utilizes a two-step chemical reaction mechanism that consists of six species: diesel fuel ($C_{10.8}H_{18.7}$), oxygen (O_2), carbon dioxide (CO_2), water (H_2O), nitrogen (N_2), and carbon monoxide (CO). The temperature variation rate is calculated based on the rate of change of species concentrations, and the heat loss correlation is also used to study the model performance. The accuracy of the model is evaluated using the test data from a production GM 6.6 L, 8-cylinder, turbocharged engine. The model is calibrated over large engine speed and load range as well as different injection timings and exhaust gas recirculation (EGR) rates by solving the optimization problem. The calibrated reaction-based model accurately predicts the indicated mean effective pressure, while keeping the errors of in-cylinder pressure and temperature small, and at the same time, significantly reduces the calibration effort, especially when the engine is operated under multiple fuel injection operations, comparing to Wiebe-based combustion models. The calibrated model parameters have a strong correlation to engine speed, load and injection timings, and as a result, a universal parameter calibration structure is proposed for entire operational conditions.

The second part of the dissertation is to obtain a parametric understanding of diesel combustion by developing a physics-based model that is able to predict the combustion metrics, such as in-cylinder pressure, burn rate, and indicated mean effective pressure (IMEP)

accurately, over a wide range of operating conditions, especially with multiple injections. In the proposed model, it is assumed that the engine cylinder is divided into three zones: a fuel zone, a reaction zone, and an unmixed zone. The formulation of reaction and unmixed zones is based on the reaction-based modeling methodology, where the interaction between them is governed by Fick's law of diffusion. The fuel zone is formulated as a virtual zone, which only accounts for mass and heat transfer associated with fuel injection and evaporation. The model is validated using test data under different speed and load conditions, with multiple fuel injections and EGR. It is shown that the three-zone model outperformed the single-zone model in in-cylinder pressure prediction and calibration effort with a mild penalty in computational time. One set of calibration parameters are used for all engine operating conditions.

The third part of the dissertation is modeling and control of engine air path with an electrically assisted boosting system. A physics-based control-oriented engine air path model with electrical assistance has been developed. The model is validated with steady-state engine test data and standard driving cycle data. Through one-dimensional simulation, it is found that the electrically assisted boosting system is able to improve engine performance under both steady-state and transient conditions. A model-based controller has been developed for the electric booster (eBoost) and bypass valve to improve the transient performance of engine load response. Experiments have been performed on a Ford 6.7 L, 8-cylinder, turbocharged diesel engine equipped with a prototype eBoost and a standard EGR valve as the bypass valve. Steady-state test results have shown that eBoost is capable of improving engine efficiency by reducing pumping loss, due to reduced turbine speed when eBoost is providing additional boost energy. In the transient process, eBoost is able to significantly reduce the response time of boost pressure tracking, as validated by load step tests.

ACKNOWLEDGEMENTS

This dissertation would not have been possible without the help from so many people who provided me with guidance, support, and encouragement. I would like to express my sincere appreciation to all of them.

Foremost, I would like to express my deepest gratitude to my advisor, Prof. Guoming (George) Zhu. It is my great privilege to study and work under his persistent support and extraordinary guidance. His comprehensive knowledge of control theory and extensive automotive application experience continually and convincingly motivated a spirit of exploration in regard to my Ph.D. research. As an advisor, his guidance is never limited to academic requirements. He set an excellent example of how to better communicate with people, manage time, and be a man of value.

I would like to express my most sincere appreciation to the committee members: Dr. Harold Schock, Dr. Hassan Khalil, and Dr. Zhaojian Li, for their guidance and insightful comments for my coursework and dissertation. Their excellent undergraduate and graduate courses provided me with valuable knowledge and a solid foundation for my research work.

I would also like to send my heartfelt thanks to the graduate students, lab engineers and visiting scholars, with whom I'm honored to have worked in our lab. My first gratitude goes to Yingxu (Ocean) Wang, who is always there to help me out. I'd like to express my appreciation to Dr. Tao Zeng who generously devoted his time guiding me through my research project. My special gratitude goes to our electrical engineer, Kevin Moran, and mechanical engineer, Tom Stuecken, without whose help it would be impossible for me to complete the experiments. Many thanks to Dr. Shupeng Zhang, Dr. Jie Yang, Dr. Ruitao Song, Dafa Yan, Mengyan Gu, Dr. Huan Li, Dr. Chengsheng Miao, Tianyi He, Ruixue Li, Shen Qu, Yu He and Dawei Hu, for their kindly help and the time we spent together.

Lastly, I am overly grateful to my parents who have been a great source of support and encouragement throughout my life.

TABLE OF CONTENTS

LIST OF TABLES

LIST OF FIGURES

CHAPTER 1

INTRODUCTION

1.1 Motivation

Internal combustion (IC) engines have been widely used in the automotive industry. Both gasoline and diesel engines have been built in passenger and commercial cars, that heavily affect in people's everyday life. It has been shown that in many developed countries, personal cars get very popular with about or even more than 0.5 cars per person [1]. The huge market size of global car fleet and the increase in the access to cars lead to potentially serious problems, such as world oil depletion [2], CO_2 emissions and climate change [3], and pollutant (NOx, HC and particulate matter) production [4]. In this scenario, changes in both the market and regulatory policies have accelerated the development of new technologies for the IC engines in the past decades. On the combustion concepts, spark-ignition (SI) engines are being developed with lean-burn combustion, stratified gasoline combustion, etc. New compression ignition (CI) combustion concepts include low-temperature combustion (LTC), homogeneous charge compression ignition (HCCI), premixed charge compression ignition (PCCI) and reactivity controlled compression ignition (RCCI). Regarding boosted engine technologies, turbochargers with variable geometry turbines (VGT) have been widely used with exhaust gas recirculation (EGR) for downsized engines. New boosting methods have been developed by combining the existing technologies, either in series or parallel. The resulting system introduces opportunities for improving efficiency and performance but also becomes more complicated to control. As the new engine technologies are developed, it is clear that the importance of engine control is growing for today and future IC engines [5].

Modern diesel engines are widely equipped with common rail direct fuel injection system, variable geometry turbocharger (VGT) and exhaust gas recirculation (EGR). Control strategies associated with these physical systems are designed to meet driver's torque demand, with

the constraints on fuel economy and emissions. Multiple injections are commonly used to control combustion phasing and duration and reduce noise, which may lead to desired output torque, peak pressure, and exhaust temperature. VGT and EGR are able to provide diesel engine with fresh air and required exhaust gas fraction, which makes it possible to meet the requirement of the engine emission standard, fuel economy, and transient performance. The control and optimization issue within this field is important and challenging. For example, the widely used combustion model for diesel engines requires a tremendous amount of calibration effort, while the accuracy of such a model does not meet the requirement under extreme operating conditions. To better control the diesel combustion under multiple injections and heavy EGR, a new modeling concept for diesel combustion dynamics is needed to replace the traditional map-based model. On the other hand, VGT and EGR are naturally coupled, leading to more challenges for robust and optimal control design of the diesel engine air charge system [6].

Model-based control is very attractive in the engine research community. With this approach, the development cycle and effort can be significantly reduced by avoiding massive engine tests. However, the key factor that determines the effectiveness of a model-based controller is the quality of the control-oriented model. It is required that the control-oriented model can reflect the plant behavior with an acceptable error while costing moderate computational resources. Most of the current methods for engine combustion and air path use manufacturer-based maps, leading to a large amount of calibration, non-physical extrapolation, and modeling errors. Physics-based modeling of engine combustion and air path dynamics may mitigate the requirement of accurate representation of a complex physical system and simply structured modeling. Considering the engine combustion with two injections, a single Wiebe function is not even able to represent the second peak of heat release rate generated by the second injection. The physics-based combustion model, on the other hand, is able to adapt to different injection events and predict the in-cylinder properties based on instantaneous condition. Considering the VGT-EGR system with an extra compressor

driven by an electric motor at the upstream of the main compressor, the main compressor may operate at a very low-pressure ratio where the map-based model could not work due to significant error. A physics-based model for the compressor, in this case, is needed for both normal operating conditions and conditions with an extremely low-pressure ratio.

A traditional calibration process for diesel combustion model can be described as follows. First, the open-loop engine test is carried out over entire engine operating conditions, as functions of engine speed, mass of fuel injection, injection timing and duration, EGR rate, etc. Then the calibration process is essentially curve/surface-fitting, with predefined functions and parameters. Each calibration parameter will result in at least one three-dimensional (3-D) lookup table. The final combustion model will be a simple function but with multiple 3-D lookup tables. A physics-based combustion model is able to reduce the modeling error at extreme conditions and eliminate the need for most lookup tables. A traditional engine controller calibration process can be described as follows. First, a feedforward map that provides the desired fuel command as a function of engine speed and driver's acceleration pedal position is developed. The second step is to optimize the VGT vane position and EGR valve position at each speed and torque condition, targeting the best performance/fuel economy with the constraints on emissions. The third step is transient calibration. During transient operations, the coupling between VGT and EGR is neglected, which indicates that the VGT vane position is used to control boost pressure and EGR valve position is used to control EGR rate separately. To achieve better tracking performance, coordinated control for VGT and EGR is made possible by multi-input-multi-output (MIMO) control theory. Assisted boosting technique has introduced more degree of freedom in control and opportunity in improving transient performance. Based on the existing modeling and control structure of VGT-EGR system, a new model and control design of the engine air charge system with an assist device can be developed to achieve better performance and fuel economy.

1.2 Research overview

The research work is divided into two parts in this dissertation: reaction-based combustion modeling, modeling and control of air charge system.

There are many types of engine combustion models. Multi-zone 3-D computational fluid dynamics (CFD) models with detailed chemical kinetic mechanisms are capable of precisely predicting the thermodynamics, flow, heat transfer, and pollutant formation during the combustion process. However, these high-fidelity models are not suitable for model-based control because they are too complicated to be used for real-time simulation. Traditionally, zero-dimensional (0-D) mean-value models are widely used for engine control and hardware-in-the-loop (HIL) simulation. The disadvantage of the mean-value model is that it does not provide detailed information about the combustion on a crank-angle base, such as in-cylinder pressure and temperature. A more widely used combustion model, called Wiebe function, is popular because it is a simple function of the current crank angle. After calibration, the Wiebe function can provide an acceptable prediction of burn rate for engine operating at normal conditions. However, Wiebe function requires significant calibration effort, especially when the operation is out of the normal range, e.g. multiple fuel injections and high EGR rate. The scope of this dissertation is to adopt a new concept of combustion modeling so that the current combustion model could be more physics-based. The adopted concept is called reaction-based modeling, i.e. using chemical kinetics to describe combustion dynamics, but maintain the model in zero dimension. The challenges of this study include: 1) implementation of thermochemistry and chemical kinetics in diesel combustion; 2) development of proper calibration structure to extend the feasible range of conditions; 3) Reduction of calibration effort by introducing key dynamics. Thus, combustion modeling work is further separated into two parts. The first part mainly deals with the calibration of the existing reaction-based model. The second part introduces the new modeling concept that completely eliminates the need for lookup tables.

There have been studies on the assisted turbocharger systems, such as regenerative hy-

draulically assisted turbocharger (RHAT) and electrically assisted turbocharger (eTurbo). It is shown that assisted devices improve engine steady-state and transient performance. The numerical and experimental study on RHAT and eTurbo is extensive. However, the study of the electrically assisted boosting system (eBoost) is not quite comprehensive. The system analysis of eBoost has been carried out with very sparse operating conditions. Study on transient performance is even rarer. The challenges of eBoost modeling and control include modeling of the compressor under very low-pressure ratio and coordinated control of eBoost compressor and bypass valve during transient operation.

1.2.1 Model-based calibration of reaction-based diesel combustion dynamics

Although crank-based Wiebe function filled the gap between mean-value model and 3-D CFD model, the drawbacks, such as large calibration effort and extrapolation error limit its application. To overcome these drawbacks, this dissertation proposes the adoption of reaction-based approach to diesel combustion. The reaction-based approach is essentially using chemical kinetics to model combustion process in zero dimension. It has already been validated in homogeneous charge compression ignition (HCCI) engines, where the combustion behavior is mainly controlled by chemical reactions. Diesel combustion, similar to HCCI, is compression ignition, although the fuel-air mixing process is much more complicated. Thus, it is promising to implement the reaction-based approach on the diesel combustion model, with moderate modifications. In order to implement the reaction-based model, the in-cylinder thermodynamics is transferred from macroscopic dimension to microscopic dimension. Every thermodynamic property is described on a molecular base. To determine which chemical kinetic mechanism to adopt, a one-step mechanism, also called global mechanism, is tested first. Then a two-step and four-step mechanism is evaluated accordingly. Considering the computational constraint and modeling error, a two-step mechanism is integrated in the model. Two parameters are identified through a sensitivity analysis of the developed single-zone two-step reaction-based model. The two parameters are the activation

energy coefficients in the first and second reaction, respectively, which is quite intuitive. It indicates that the diesel combustion is mostly dominated by chemical reactions. The model is then calibrated and validated using engine test data. It is shown that the two rate coefficients vary as the engine operating condition changes. To reduce the requirement for lookup tables, a calibration structure is developed so that the two coefficients can be fit to polynomial as a function of injection timing and EGR rate. The calibration structure has extend the applicable range of reaction-based model for diesel engines. It also improves the in-cylinder pressure prediction accuracy and reduces number of calibration parameters, compared to Wiebe function.

1.2.2 Multi-zone reaction-based modeling of diesel combustion

Multi-zone approach is widely used in diesel combustion models. Combining the reaction-based method and multi-zone approach introduces a new opportunity to improved accuracy and calibration efficiency.

Although the developed single-zone two-step reaction-based diesel combustion model has shown potential for improving prediction accuracy and less calibration, there are two issues that are not addressed yet: 1) the burn rate is overpredicted due to homogeneous assumption; 2) there are still lookup tables. To address the above issues, it is necessary to account for in-cylinder inhomogeneity but still maintain the model in zero-dimensional. A multi-zone approach is a natural option. There are many types of multi-zone approaches that are applicable to diesel combustion, such as droplet breakup model, multiple identical reaction zones, charge mixing model, turbulence model, etc. This dissertation proposes a three-zone model significantly different than the above-mentioned models. In the proposed model, there are three 0-D thermodynamic zones: fuel zone, reaction zone, and unmixed zone. Each zone undergoes a unique physical process. The zone-to-zone interaction mitigates the sensitivity in reaction coefficients and consequently eliminates the need for lookup tables. The burn rate is less overpredicted due to relaxation of rate coefficients for the start of combustion. The

model has been validated with engine test data under multiple fuel injections and different EGR rates. It is shown that the three-zone model is valid over a wide range of operating conditions, which is a significant improvement compared to the single-zone model. The developed reaction-based model cost only moderate computational resources and can be used for model-based control. Furthermore, the calibration parameters can be fixed over the entire engine operational map, which significantly simplifies the calibration process.

1.2.3 Modeling and control of an electrically assisted boosting system

To improve engine performance and fuel economy with eBoost, modeling and control of engine air path with eBoost are essential. This dissertation adopts a standard 0-D engine air path model with VGT and EGR. An eBoost model, which consists of an electric compressor and a bypass valve, is added at the upstream of the main compressor. The physics-based model has been validated with steady-state engine test data and driving cycle data. The system behavior has been studied through 1-D simulations. It is shown that with eBoost activated, engine steady-state performance (fuel economy) can be improved, mostly at low speed and high load conditions. The corresponding optimal VGT and EGR positions change as well. In addition, different configurations (upstream and downstream) have been studied and compared over the entire engine map. It is found that the downstream is preferred in most engine speed and load conditions except the driving cycle range. In the transient process, with a load step commanded, eBoost is able to track the target boost pressure much faster than VGT alone. The reduction in boost pressure response directly leads to improved engine torque response. A full-order multi-input-multi-output (MIMO) linear quadratic (LQ) controller has been designed for set point regulation. With the weighting matrices well tuned, the LQ controller outperformed the baseline decoupled PID controller. The improvement in both steady-state and transient operation of the eBoost assist has been validated with engine tests.

1.3 Dissertation contributions

The major contribution of this dissertation can be summarized as follows:

1. A reaction-based modeling methodology has been formulated and implemented in diesel combustion model. The proposed model successfully predicts the in-cylinder pressure with acceptable error. The sensitivity study shows that only two calibration parameters are required to accurately calibrate the model. A calibration structure has been developed so that the number of required lookup tables is reduced significantly. The finalized combustion model can be a potential candidate to replace the existing Wiebe function.

2. A three-zone modeling approach has been proposed specifically for diesel combustion. The developed model improves the prediction accuracy and eliminates the lookup tables, which are the main drawbacks of the single-zone model, especially with multiple injections. The three-zone reaction-based model has only a slight increase in computational time and can still be implemented for model-based control and real-time simulation. The calibration parameters are fixed over the entire engine operational range, which eliminates the need for lookup tables. It is a promising model for future combustion control.

3. A physics-based engine air path model with eBoost has been developed. The proposed model has been validated with steady-state engine test data and standard cycle data. The system behavior has been studied through 1-D simulations. It is found that eBoost improves steady-state and transient performance. Both an error-based and a model-based controller has been developed to verify the capability of eBoost. It turned out that the model-based controller, with well-tuned gain, has a better performance than the error based controller. Experiments have been performed for validating the simulation results.

1.4 Dissertation outline

The content of the dissertation is organized as follows. In Chapter 2, a comprehensive review of the development and applications of engine combustion models is presented. The mathematical formulation of the reaction-based model for engine combustion has been derived. The construction of calibration of reaction-based diesel combustion model makes it possible for the model to be feasible for diesel engines. The model and calibration approach is validated with experimental data. In Chapter 3, a multi-zone approach is introduced to account for inhomogeneities in the engine combustion chamber, which eliminates the modeling error compared to the single-zone model. It turned out that the three-zone model significantly reduces the prediction error over a wider range of operating conditions and also eliminates calibration parameter sensitivity, leading to fixed calibrations over the entire engine operating range. In Chapter 4, modeling and control of an electrically assisted boosting system will be presented. The eBoost system improves engine steady-state and transient performance, which is validated both numerically and experimentally. Chapter 5 concludes the dissertation and suggests some future work.

CHAPTER 2

REACTION-BASED MODELING OF COMBUSTION DYNAMICS

2.1 Introduction

Modern internal combustion engines are equipped with sophisticated systems to monitor and control various aspects of engine performance during ongoing operations to meet operator demands for performance (including torque and fuel economy) and to satisfy government regulations related to emissions, safety, and fuel economy. To enable model-based engine control, physics-based control-oriented engine models were developed to simulate the engine behavior in real-time. In order to accurately predict the engine output torque, a control-oriented in-cylinder pressure model is needed. Various combustion models have been developed with different levels of accuracy and computational efficiency. Wiebe function was widely used in real-time engine simulations for pressure modeling due to its simplicity. It also has major limitations. More complicated combustion models are accurate but require too much computational resource. In this section, a review of different combustion models is presented. The reason why the reaction-based model is suitable for control is also addressed.

2.1.1 Engine combustion models

Engine combustion models are used for simulating in-cylinder dynamics of fuel-air reaction. In addition to the variation of species concentrations, the combustion process is always associated with temperature and pressure change. From a specific point of view, the combustion model only deals with how the chemical energy is released and it is often a simple curve of mass fraction burned (MFB). However, studying such type model alone is difficult because the combustion process is the result of interaction between the reacting substances and the environment. Therefore, a general point of view, where the combustion model consists of chemical heat release, mass and energy conservation, heat transfer and even fluid mechanics,

is needed. Under this architecture, the number of dimension for a combustion model could be 0, 1, 2 or 3. According to the published research on engine combustion models, the most popular models that have been developed to date may be grouped into four categories, as shown in Figure 2.1:

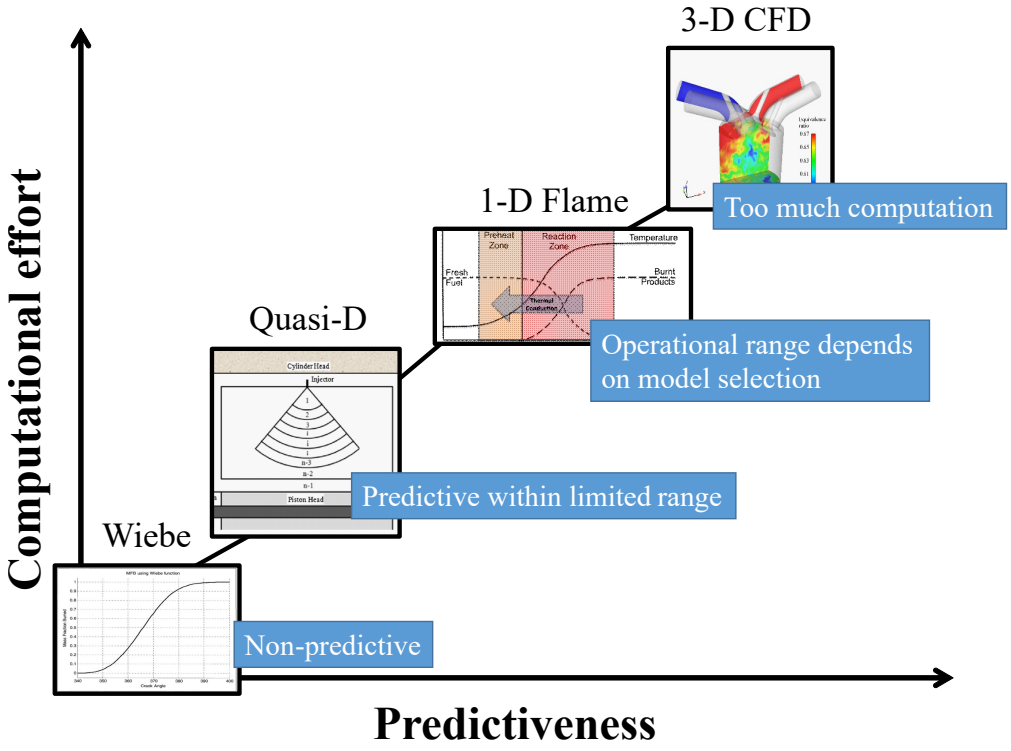

Figure 2.1: Category of engine combustion models

In the above classification, as the dimension of a model increases, both prediction accuracy and computational effort increase, leading to a trade-off between accuracy and computing efficiency. Different application situation will result in different type of model. For example, for accurate simulation of spatial flame characteristics, a 3-D computational fluid dynamics (CFD) model is needed. If the model is used for control design where accuracy is not strictly required, Wiebe function will work properly because it is easy to implement and runs fast.

Zero-dimensional (0-D) models are the simplest and most suitable to observe the effects of empirical variations in the engine operating parameters on overall heat release rates/cylinder

pressure schedules. These models are zero dimension in the sense that they do not involve any consideration of the flow field dimensions. Thus, for the purpose of real-time simulation, zero-dimensional models are most feasible.

Zero-dimensional models are further sub-divided into single zone models, two zone models, and multi-zone models. In single zone models, the working fluid in the engine is assumed to be a thermodynamic system, which undergoes energy and/or mass exchange with the surroundings and the energy released during the combustion process is obtained by applying the first law of thermodynamics to the system. In two-zone models, the working fluid is imaginarily divided into two zones, unburned and burned zones. These zones are actually two distinct thermodynamic systems with energy and mass interactions between themselves and their common surroundings, the cylinder walls. The mass-burning rate (or the cylinder pressure), as a function of crank angle, is then numerically computed by solving the simplified equations resulting from applying the first law to the two zones.

Most control-oriented models to date are implemented with so-called Wiebe function for the calculation of heat release rate due to combustion. The Wiebe function generally has the following format:

$$x_b = 1 - \exp\left[-a\left(\frac{\theta - \theta_s}{\Delta\theta_b}\right)^{m+1}\right] \tag{2.1}$$

where x_b is the mass-fraction-burned of fuel; a and m are experimentally calibrated coefficients; θ_s is the start of combustion (SOC), $\Delta\theta_b$ is the burning duration (BD), only these two parameters could affect the combustion process during the simulation.

While the function itself is simple and easy to use, it can only be affected by specified parameters during the combustion process, such as SOC, BD, etc., and experiment based fitting coefficients, because of its empirical feature.

2.1.2 Wiebe function

Since Wiebe function is well-known, investigating its origins can be an interesting act, which could provide insights in developing reaction-based combustion models.

In the mid-1950s, with Nikolay Semenov's work in the area of chemical kinetics and chain chemical reactions, engine researchers believed that a better model for internal combustion engine combustion could be constructed based on the theory of radical chain reactions. Wiebe linked chain chemical reactions with the fuel reaction rate in internal combustion engines and his approach was based on the assumption that a single-step rate equation will not be adequate to describe complex reacting systems such as those occurring in an internal combustion engine. On the other hand, developing and solving rate equations which account for the simultaneous and sequential interdependent chain and chain branching reactions would be prohibitive. He reasoned that, for engineering purposes, the details of chemical kinetics of all the reactions could be bypassed and a general macroscopic reaction rate expression could be developed based on the concept of chain reactions. The details of his modeling approach are described below [7].

In actual combustion systems such as in an internal combustion engine, chain reactions may proceed sequentially and in parallel with the formation of intermediate species comprising free atoms and radicals. Wiebe called these intermediate species *active centers*. Being highly reactive, active centers play a pivotal role in chemical kinetics reactions and are crucial to the reaction path. For the initiation of the reaction, a certain concentration of active centers (initial centers) is required and these centers can be generated by heating the air-fuel mixture or providing an electrical charge. During the combustion process, a very large number of active centers will exist in close proximity to the molecules of the main reacting substances. Combustion produces molecules of final products and more active centers that are capable of starting new reaction cycles. Excluded from this scheme are chain inhibiting centers resulting from radicals or free atoms colliding with a third body (any other radical, atom, or molecule in the system or the walls). As combustion progresses, the concentration of reactants decreases progressively, causing a corresponding decrease in the reaction rate.

In the oxidation of carbon monoxide, the global reaction is represented as

$$2\,\mathrm{CO} + \mathrm{O_2} \longrightarrow 2\,\mathrm{CO_2} \tag{2.2}$$

A leading role is played by the elementary process

$$OH + CO \xrightarrow{k1} CO_2 + H \qquad \text{(Reaction I)}$$

The most probable reaction of atomic hydrogen is

$$H + O_2 \xrightarrow{k2} OH + O \qquad \text{(Reaction II)}$$

which leads to the next reaction

$$O + CO \xrightarrow{k3} CO_2 \qquad \text{(Reaction III)}$$

The three elementary processes (I, II, and III) make up an *elementary reaction cycle* which is continuously repeated as the chain reactions propagate. The highly reactive radicals OH produced by process (II) are the active centers.

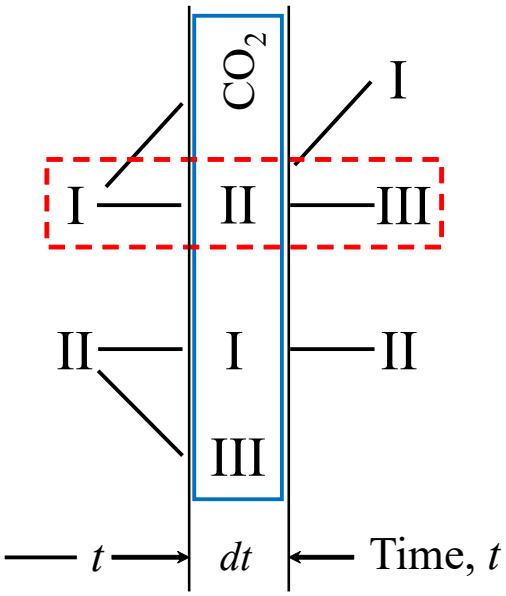

Figure 2.2: Schematic diagram of Wiebe's approach

These and other reactions may proceed in parallel or sequentially as shown schematically in Figure 2.2. The reactions within the dashed-line boxes are the elementary reaction cycles, whereas the reactions within the solid-line boxes are the *effective reaction events*. The latter represent ensembles of simultaneously occurring elementary reactions at time t resulting in

the formation of products of complete combustion (CO_2) within a very short time interval dt, and active centers (OH) capable of initiating subsequent *effective reaction events* unless they are destroyed upon collision with the walls of the reaction vessel. The active centers initiating the effective reaction events were referred by Wiebe as *effective centers*.

On the basis of this concept, Wiebe postulated that the incremental change in the number of molecules of the main reactants dN participating in the effective reaction events in the time interval t to $t + dt$ is directly proportional to the change in the number of effective centers dN_e (i.e. $-dN = ndN_e$), where n is the constant of proportionality. In differential form

$$-\left(\frac{dN}{dt}\right) = n\left(\frac{dN_e}{dt}\right) \tag{2.3}$$

The relative density of the effective centers is defined as

$$\rho = \left(\frac{dN_e}{dt}\right) \Big/ N \tag{2.4}$$

where N is the instantaneous number of molecules of the initial reactants. Equation (2.3) can now be written as

$$-\frac{dN}{N} = n\rho dt \tag{2.5}$$

from which

$$\ln \frac{N}{N_0} = -\int_0^t n\rho dt$$

$$N = N_0 e^{-\int_0^t n\rho dt} \tag{2.6}$$

where N_0 is the number of moles of the main reactant in the combustion system at the start of reactions.

If the burned fraction of the initial reactant at any moment in time t is defined as

$$x = \frac{N_0 - N}{N_0} \tag{2.7}$$

then

$$x = 1 - e^{-\int_0^t n\rho dt} \tag{2.8}$$

Wiebe assumed that the relative density of the effective centers can be expressed as $\rho = kt^m$, where k and m are constants, and if $nk = K$, equation (2.8) can be transformed into

$$x = 1 - e^{[K/(m+1)]t^{m+1}} \tag{2.9}$$

Wiebe named the parameter m "combustion characteristic exponent".

From equation (2.9) it is apparent that the chemical reactions cease when the burned fraction x tends to unity as time tends to infinity. However, in reality the combustion process in an internal combustion engine is finite and if the combustion duration is denoted by t_d, the burn fraction becomes

$$x_d = 1 - e^{[K/(m+1)]t_d^{m+1}} \tag{2.10}$$

from which

$$e^{[K/(m+1)]t_d^{m+1}} = 1 - x_d \tag{2.11}$$

Similarly at any time t

$$e^{[K/(m+1)]t^{m+1}} = 1 - x \tag{2.12}$$

Taking the logarithm of equations (2.11) and (2.12) and dividing one by the other yields

$$x = 1 - e^{C(t/t_d)^{m+1}} \tag{2.13}$$

where $C = \ln(1 - x_d)$. Wiebe assumed that $x_d = 0.999$ and rounded off the corresponding value of C to 6.908.

The Wiebe function for the non-dimensional burned fraction x as a function of crank angle degrees can be written as

$$x = 1 - \exp\left[-6.908\left(\frac{\theta}{\theta_d}\right)^{m+1}\right] \tag{2.14}$$

In deriving the burned fraction function, Wiebe made several assumptions that may not be true in reality. For example, for reactions I, II, and III, at any instant of time, the ensemble reaction is expressed as

$$(k_1 + k_3)\,\mathrm{CO} + k_2\,\mathrm{O_2} \longrightarrow (k_1 + k_3)\,\mathrm{CO_2} + (k_1 - k_2)\,\mathrm{H} + (k_2 - k_3)\,\mathrm{O} + (k_2 - k_1)\,\mathrm{OH}$$

where $dN = -(k_1 + k_2 + k_3)$, $dN_e = k_2 - k_1$. Wiebe assumed $-dN = ndN_e$, which means

$$k_1 + k_2 + k_3 = n(k_2 - k_1)$$

Note that this is not necessarily true.

In summary, Wiebe function is a good attempt to replace single-step global reaction with ideal chemical kinetics. However, it is over-simplified such that it loses the physical foundation behind the model.

2.1.3 Reaction-based model

Reaction-based combustion modeling technique has been used for off-line simulations in the past. Autoignition behavior with different diesel blends was model in references [8] and [9], where a reaction-based combustion model was used for predicting the autoignition. A reduced chemical kinetic model was developed in [10] to simulate the IC (internal combustion) engine combustion process with primary reference fuels and the model was fairly complicated and cannot be used for real-time simulations. A multistage combustion model for diesel engines is presented in [11], where three combustion stages, autoignition, premixed and diffusion combustion are considered in the combustion process for a typical medium speed diesel engine. Significant improvement in cylinder pressure and temperature prediction is achieved. A control-oriented two-zone thermal kinetic model for a single cylinder HCCI engine is presented in [12], where the combustion process was modeled using the first law of thermodynamics and mixture concentration inhomogeneity.

As a summary, chemical kinetic mechanisms and thermal kinetic combustion models have been developed in the past. However, the chemical kinetic mechanism is too complex to be used for real-time simulations; and the simple thermal kinetic model may not provide the accuracy needed for model-based control. For the proposed research, the chemical kinetic mechanism will be simplified and combined with the thermal kinetic model to achieve real-time simulations with desired modeling accuracy required for model-based control.

2.2 Chemical kinetics

In order to enable reaction-based models, a solid background in combustion chemistry and chemical kinetics is necessary. Thermochemistry deals with stoichiometry for chemical reactions and thus, information of reactants and products at the beginning and the end of combustion process can be obtained, while chemical kinetics explains the rates of reactions, which solves for the instantaneous concentration of each species. With such knowledge, one can calculate the concentration of any one of the species involved in the combustion at any instant of time. The detailed theory of combustion can be found in [13].

Chemical kinetics is a powerful tool to understand combustion. In many engine combustion processes, chemical reaction rates control the overall rate of combustion. Also, ignition and flame extinction are intimately related to chemical processes. Much progress has been made to date since chemists have been able to define the detailed chemical pathways leading from reactants to products and to measure or calculate their associated rates. It is hoped that we could apply the basic chemical kinetics concepts to engine combustion models to achieve reasonable precision but low computational complexity.

2.3 Reaction-based modeling approach

With all the background introduced in the previous section, the reaction-based modeling methodology can now be formulated. The developed model has been implemented for continuous-time simulations.

2.3.1 Overview of the modeled physics

There are two cycle types for the engine combustion model: closed cycle and full cycle. Closed cycle refers to the crank angle from intake valve closing (IVC) to exhaust valve opening (EVO). In the closed cycle model, there is no flow model. The conditions at IVC are the input to the model and can be estimated from experimental data. A full cycle model is the closed cycle model combined with the flow model, extending the crank angle range to

0-720 CAD. Figure 2.3 shows the architecture of the full-cycle model. To enable the closed cycle model we only need to turn off the flow feature in the full cycle model. The structure of the closed cycle model is shown in Figure 2.4.

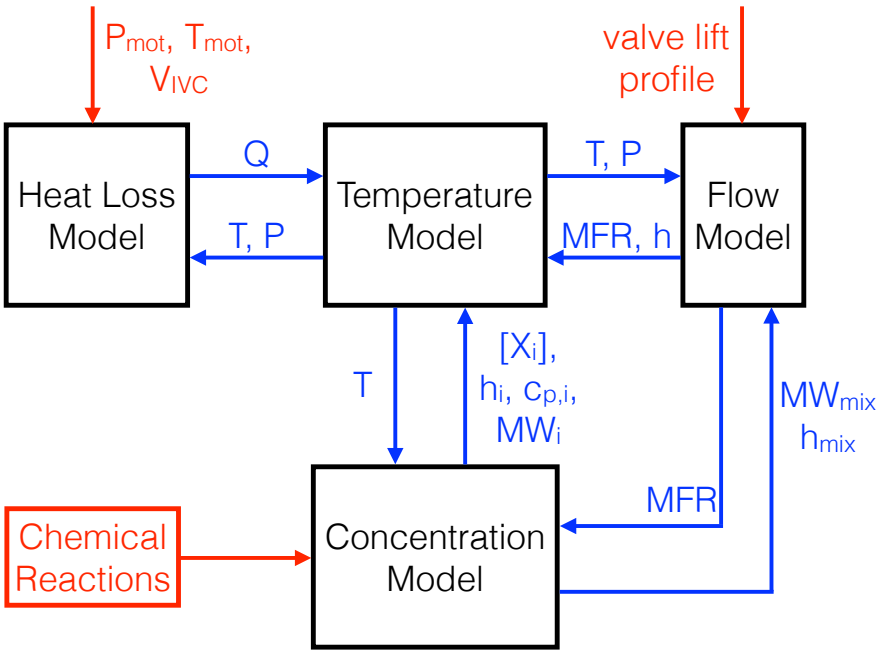

Figure 2.3: Full-cycle reaction-based modeling architecture

2.3.2 Molar concentration rate of species

The rate of change of concentration for species i, $[\dot{X}_i]$, is related to number of moles of species i in the cylinder, N_i, by:

$$[\dot{X}_i] = \frac{d}{dt}\left(\frac{N_i}{V}\right) = \frac{\dot{N}_i}{V} - \frac{\dot{V}N_i}{V^2} = w_i - \frac{\dot{V}}{V}[X_i] \tag{2.15}$$

where

$$w_i \equiv \frac{\dot{N}_i}{V} \tag{2.16}$$

The concentration production term w_i can be further divided into two parts:

$$w_i = w_{rxn,i} + w_{flow,i} \tag{2.17}$$

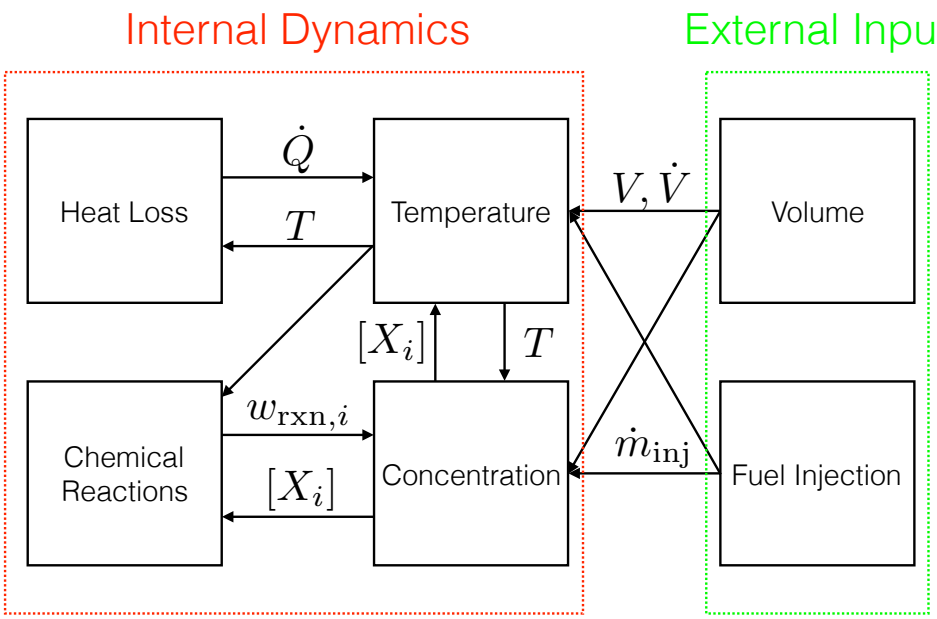

Figure 2.4: Closed-cycle reaction-based modeling architecture

where $w_{rxn,i}$ is the concentration production due to chemical reactions, which is determined through the use of a combustion chemistry mechanism (Section 2.3.5); $w_{flow,i}$ is the concentration change due to mass flow into and out of the control volume (Section 2.3.6).

2.3.3 Instant cylinder volume and volume rate

The instant volume V is dependent on the current crank angle and geometry of the cylinder. It is given by

$$V(t) = V_c + \frac{\pi B^2}{4}\left[l + a - a\cos\left(\frac{\pi}{30}N_e \cdot t\right) - \sqrt{l^2 - a^2\sin^2\left(\frac{\pi}{30}N_e \cdot t\right)}\right] \tag{2.18}$$

where V_c is the clearance volume; B is bore; l is connecting rod length; a is crank radius (half stroke); N_e is engine speed in r/min; t is time.

The volume rate $\dot{V}$ is given by

$$\dot{V} = \frac{a\pi^2 B^2}{120}N_e \cdot \sin\left(\frac{\pi}{30}N_e \cdot t\right)\left(1 + a\frac{\cos\left(\frac{\pi}{30}N_e \cdot t\right)}{\sqrt{l^2 - a^2\sin^2\left(\frac{\pi}{30}N_e \cdot t\right)}}\right) \tag{2.19}$$

2.3.4 Temperature rate

There are two different methods developed for calculation of in-cylinder temperature and pressure. The first method, called heat release rate method (see Figure 2.5a), is similar to that of Wiebe-based models. In general, this method firstly calculates the mass fraction burned (MFB) of fuel from either Wiebe function or chemical reactions. Noting that for Wiebe function, the MFB is directly calculated. But for reaction-based models, we must first get the concentration of fuel by solving the associated differential equation. Then we will be able to calculate the MFB of the fuel. Next, the heat release rate is calculated from the derivative of MFB. By the first law of thermodynamics, it is straightforward to get the temperature of the in-cylinder mixture. The in-cylinder pressure is calculated by the equation of state.

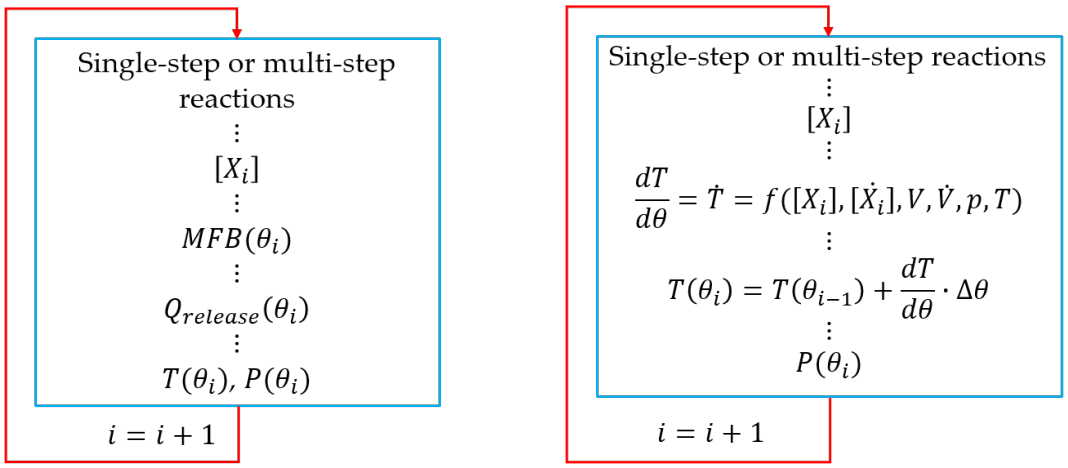

(a) Heat release rate method (b) Temperature rate method

Figure 2.5: Methods for in-cylinder temperature and pressure calculation

The second method, called temperature rate method (see in Figure 2.5b), follows a slightly different path, and note that is this method is not applicable for Wiebe function. Firstly, the concentration of each species participating in the chemical reactions is solved. Secondly, it is shown later that the temperature rate is a function of the concentration and concentration rate of all the species as well as current temperature and pressure. At last, the temperature for next time step is easily calculated numerically. The calculation of in-cylinder pressure is

the same as before. To be more specific, the mathematical derivation is given as follows [14]: The first law of thermodynamics for a closed system:

$$\frac{dU}{dt} = \dot{Q} - \dot{W} + \sum \dot{m}_j h_j \tag{2.20}$$

where U is the internal energy of the system; $\dot{Q}$ is the net heat transfer rate into the system; $\dot{W}$ is the net rate of work done by the system; and $\sum \dot{m}_j h_j$ is the energy change due to mass flow.

For the case of the piston cylinder, the work output rate is:

$$\dot{W} = P\dot{V} \tag{2.21}$$

where P is the pressure.

Now, given that the enthalpy is related to the internal energy as:

$$H = U + PV \tag{2.22}$$

Then the left hand side (LHS) of Equation (2.20) becomes

$$\frac{dU}{dt} = \frac{d(H - PV)}{dt} = \frac{dH}{dt} - \frac{d(PV)}{dt} = \frac{dH}{dt} - \dot{P}V - P\dot{V} \tag{2.23}$$

Equation (2.20) can be re-arranged as

$$\frac{dH}{dt} = \dot{Q} + \dot{P}V + \sum \dot{m}_j h_j \tag{2.24}$$

The extensive property H can be expressed as a sum of weighted molar enthalpies of all species

$$H = \sum N_i \bar{h}_i \tag{2.25}$$

where $\bar{h}_i$ is the molar enthalpy of species i.

Thus LHS of Equation (2.24) becomes

$$\frac{dH}{dt} = \frac{d(\sum N_i \bar{h}_i)}{dt} = \frac{d(V \sum [X_i]\bar{h}_i)}{dt} = \dot{V} \sum [X_i]\bar{h}_i + V \sum [\dot{X}_i]\bar{h}_i + V \sum [X_i]\dot{\bar{h}}_i \tag{2.26}$$

where

$$\dot{\bar{h}}_i = \bar{c}_{p,i}\dot{T}$$

Note that $\bar{c}_{p,i}$ is the contant-pressure specific heat; T is the temperature; $\dot{T}$ is the temperature rate. Thus,

$$\text{LHS} = \frac{dH}{dt} = \dot{V}\sum[X_i]\bar{h}_i + V\sum[\dot{X}_i]\bar{h}_i + V\dot{T}\sum[X_i]\bar{c}_{p,i}. \tag{2.27}$$

From the state equation of ideal gas, we have

$$P = \sum[X_i]R_uT \tag{2.28}$$

and

$$\dot{P} = R_uT\sum[\dot{X}_i] + R_u\dot{T}\sum[X_i], \tag{2.29}$$

where $R_u = 8314\,(\text{J/kmol}\cdot\text{K})$ is the universal gas constant.

The right hand side (RHS) of Equation (2.24) becomes

$$\text{RHS} = \dot{Q} + R_uTV\sum[\dot{X}_i] + R_u\dot{T}V\sum[X_i] + \sum\dot{m}_jh_j \tag{2.30}$$

Re-arranging the equation, we have the expression to calculate temperature rate

$$\dot{T} = \frac{\dot{Q} + R_uTV\sum[\dot{X}_i] - V\sum[\dot{X}_i]\bar{h}_i - \dot{V}\sum[X_i]\bar{h}_i + \sum\dot{m}_jh_j}{V\sum[X_i]\left(\bar{c}_{p,i} - R_u\right)}. \tag{2.31}$$

Equations (2.15), (2.19) and (2.31) represent the set of nonlinear differential equations for each of the states used in the model.

2.3.5 Rates of reactions

Three different modeling paths are studied: single-step reaction model [13], two-step reaction model [15, 16] and four-step reaction model [17]. The single-step reaction is simple thus we will start with this model to demonstrate our reaction-based modeling approach. Our final objective is to develop a reaction model with reasonable accuracy and simplicity. Up to this point, we attempted the two-step model with an additional reaction for CO oxidation, and formulated a four-step model by further including two additional reactions. For each

model, the stoichiometric reaction of diesel fuel (with pseudo formula $C_{10.8}H_{18.7}$) and air is assumed. The major products assumption is also made, such that the global reaction for combustion can be written as:

$$C_{10.8}H_{18.7} + 15.48\,O_2 + 58.19\,N_2 \longrightarrow 10.8\,CO_2 + 9.35\,H_2O + 58.19\,N_2 \tag{2.32}$$

The reaction rate for $C_{10.8}H_{18.7}$ oxidation in single step is given in the Arrhenius form as:

$$w_{C_{10.8}H_{18.7}} = A \exp\left(-\frac{E_A}{R_u T}\right) [C_{10.8}H_{18.7}]^m [O_2]^n \tag{2.33}$$

where A, E_A, m and n are the coefficients to be calibrated. There are also references for these coefficients in [13]. By inspection of Equation (2.32) the rates of reactions of other species can be calculated in terms of $w_{C_{10.8}H_{18.7}}$ directly:

$$w_{O_2} = 15.48 w_{C_{10.8}H_{18.7}} \tag{2.34a}$$

$$w_{N_2} = 0 \tag{2.34b}$$

$$w_{CO_2} = -10.8 w_{C_{10.8}H_{18.7}} \tag{2.34c}$$

$$w_{H_2O} = -9.35 w_{C_{10.8}H_{18.7}} \tag{2.34d}$$

where the minus sign indicated that while $C_{10.8}H_{18.7}$ and O_2 are being consumed, CO_2 and H_2O are being created.

This single-step reaction rate model utilizes the idea of chemical reaction and the associated rates. The advantages of this approach are obvious because only 4 are involved in the formulation. Since it is a linear function of the amount of fuel reacted, the heat release calculation is also quite simple. However, the time delay during the early stage caused by the formation of intermediate hydrocarbons and CO is not described by the formulation, which could not provide accurate information of hydrocarbon oxidation. In addition, the in-cylinder mixture is assumed to be perfectly mixed before the start of combustion, which is not the case for diesel engines. The rate of oxidation to CO_2 is expected to proceed very fast. One way to slow down the combustion is to add more reactions (steps) into the system,

such as breakdown of the fuel to the intermediate hydrocarbons, the oxidation of the intermediate hydrocarbons to CO, and the oxidation of CO to CO_2, so that the energy release is distributed in each step.

Consider the two-step chemical kinetic mechanism:

$$C_{10.8}H_{18.7} + 10.08\,O_2 + 58.19\,N_2 \longrightarrow 10.8\,CO + 9.35\,H_2O + 58.19\,N_2 \tag{2.35a}$$

$$CO + 0.5\,O_2 \rightleftharpoons CO_2 \tag{2.35b}$$

The reaction rates for $C_{10.8}H_{18.7}$ and CO oxidation are given as:

$$w_{C_{10.8}H_{18.7}} = A_1 \exp\left(-\frac{E_{A,1}}{R_u T}\right)[C_{10.8}H_{18.7}]^{m1}[O_2]^{n1} \tag{2.36a}$$

$$w_{CO_{ox}} = A_2 \exp\left(-\frac{E_{A,2}}{R_u T}\right)[CO]^{m2}[H_2O]^{k1}[O_2]^{n2} - A_3 \exp\left(-\frac{E_{A,2}}{R_u T}\right)[CO_2]^{k2} \tag{2.36b}$$

where A_1, A_2, A_3, $E_{A,1}$, $E_{A,2}$, $E_{A,3}$, m_1, m_2, n_1, n_2, k_1 and k_2 are the coefficients to be calibrated (for reference, see [13]). By inspection of equations (2.35a) and (2.35b), the other reaction rates follows as:

$$w_{O_2} = 10.08 w_{C_{10.8}H_{18.7}} + 0.5 w_{CO_{ox}} \tag{2.37a}$$

$$w_{N_2} = 0 \tag{2.37b}$$

$$w_{CO_2} = -w_{CO_{ox}} \tag{2.37c}$$

$$w_{H_2O} = -9.35 w_{C_{10.8}H_{18.7}} \tag{2.37d}$$

$$w_{CO} = -10.8 w_{C_{10.8}H_{18.7}} + w_{CO_{ox}} \tag{2.37e}$$

The two-step model basically separates the highly exothermic oxidation of CO to CO_2 from the less exothermic oxidation of the fuel to CO:

1) $C_{10.8}H_{18.7} \xrightarrow{\dot{Q}_1} CO$

2) $CO \xrightarrow{\dot{Q}_2} CO_2$

Since no prediction is made for the formation of intermediate hydrocarbons, this approach does not account for the time delay in the initial release of a significant amount energy. However, the two-step model is simple for implementation, thus the majority of the study has been done using the two-step model.

Consider the four-step chemical kinetic mechanism for hydrocarbon oxidation [18]:

$$\mathrm{C}_n\mathrm{H}_{2n+2} \longrightarrow \frac{n}{2}\mathrm{C}_2\mathrm{H}_4 + \mathrm{H}_2 \tag{2.38a}$$

$$\mathrm{C}_2\mathrm{H}_4 + \mathrm{O}_2 \longrightarrow 2\,\mathrm{CO} + 2\,\mathrm{H}_2 \tag{2.38b}$$

$$\mathrm{CO} + \frac{1}{2}\mathrm{O}_2 \longrightarrow \mathrm{CO}_2 \tag{2.38c}$$

$$\mathrm{H}_2 + \frac{1}{2}\mathrm{O}_2 \longrightarrow \mathrm{H}_2\mathrm{O} \tag{2.38d}$$

where the reaction rates are expressed as

$$w_{\mathrm{C}_n\mathrm{H}_{2n+2}} = -10^x \exp\left(-\frac{E_A}{R_u T}\right)[\mathrm{C}_n\mathrm{H}_{2n+2}]^a[\mathrm{O}_2]^b[\mathrm{C}_2\mathrm{H}_4]^c \tag{2.39a}$$

$$w_{\mathrm{C}_2\mathrm{H}_4} = -10^x \exp\left(-\frac{E_A}{R_u T}\right)[\mathrm{C}_2\mathrm{H}_4]^a[\mathrm{O}_2]^b[\mathrm{C}_n\mathrm{H}_{2n+2}]^c \tag{2.39b}$$

$$w_{\mathrm{CO}} = -10^x \exp\left(-\frac{E_A}{R_u T}\right)[\mathrm{CO}]^a[\mathrm{O}_2]^b[\mathrm{H}_2\mathrm{O}]^c 7.93\exp(-2.48\phi) \tag{2.39c}$$

$$w_{\mathrm{H}_2} = -10^x \exp\left(-\frac{E_A}{R_u T}\right)[\mathrm{H}_2]^a[\mathrm{O}_2]^b[\mathrm{C}_2\mathrm{H}_4]^c \tag{2.39d}$$

where ϕ is the equivalence ratio. The exponents x, a, b and c are different for each reaction. The reference value for these coefficients are available for propane ($\mathrm{C}_3\mathrm{H}_8$) in [13].

Note that by assigning negative values to $\mathrm{C}_n\mathrm{H}_{2n+2}$ and $\mathrm{C}_2\mathrm{H}_4$ exponents, the oxidation of $\mathrm{C}_2\mathrm{H}_4$ and H_2 could be inhibited. This indicates the potential of using the four-step model to reduce the overall burn rate.

2.3.6 Flow rate

The term "flow rate" in this section is a generalized concept, which includes both gas flow rate by valves and fuel injection rate. We will focus on development of the gas flow rate model

for the four cases during gas exchange. The fuel injection rate can be simply implemented if the fuel injection profile is known.

For unchoked flow, meaning

$$\frac{p_T}{p_0} > \left(\frac{2}{\gamma+1}\right)^{\frac{\gamma}{\gamma-1}},$$

we have

$$\dot{m} = \frac{C_D A_R p_0}{\sqrt{\frac{R_u}{MW} T_0}} \left(\frac{p_T}{p_0}\right)^{\frac{1}{\gamma}} \left[\frac{2\gamma}{\gamma-1}\left[1-\left(\frac{p_T}{p_0}\right)^{\frac{\gamma-1}{\gamma}}\right]\right]^{\frac{1}{2}}, \tag{2.40}$$

where p_T is the downstream pressure; p_0 and T_0 are the upstream stagnation pressure and temperature, respectively; γ is the specific heat ratio; C_D is the discharge coefficient; A_R is the reference open area for the valve.

For choked flow, meaning

$$\frac{p_T}{p_0} \leq \left(\frac{2}{\gamma+1}\right)^{\frac{\gamma}{\gamma-1}},$$

we have

$$\dot{m} = \frac{C_D A_R p_0}{\sqrt{\frac{R_u}{MW} T_0}} \sqrt{\gamma} \left[\frac{2}{\gamma+1}\right]^{\frac{\gamma+1}{2(\gamma-1)}}. \tag{2.41}$$

where γ, C_D and A_R to be determined.

2.3.7 Heat loss rate

The heat transfer rate $\dot{Q}$ can be expressed as

$$\dot{Q} = \frac{-A_c h_c (T - T_w)}{N_e}, \tag{2.42}$$

where A_c is the contact area between gas and cylinder wall; h_c is the heat transfer coefficient; T is the cylinder temperature; T_w is the cylinder wall temperature.

We can calculate the contact area by engine geometry and piston motion

$$A_c = A_{ch} + A_p + \pi B(l + a - s), \tag{2.43}$$

where A_{ch} is the cylinder head surface area; A_p is the piston crown surface area ($A_p = \frac{\pi B^2}{4}$ for flat-topped pistons); s is the distance between crank axis and the piston pin axis and is given as

$$s = a\cos\left(\frac{\pi}{30}N_e \cdot t\right) + \sqrt{l^2 - a^2\sin^2\left(\frac{\pi}{30}N_e \cdot t\right)}$$

Thus, the contact area can be written as

$$A_c = A_{ch} + \frac{\pi B^2}{4} + \pi B\left(l + a - a\cos\left(\frac{\pi}{30}N_e \cdot t\right) + \sqrt{l^2 - a^2\sin^2\left(\frac{\pi}{30}N_e \cdot t\right)}\right), \quad (2.44)$$

where $R = \frac{l}{a}$ is the ratio of connecting rod length to crank radius.

The heat transfer coefficient can be correlated as

$$h_c = \alpha B^{-0.2} P^{0.8} T^{-0.55}\left[C_1\bar{S}_p + C_2\frac{V_d T_r}{P_r V_r}(P - P_{mot})\right]^{0.8}, \quad (2.45)$$

where $\bar{S}_p$ is the mean piston speed (m/s); V_d is the displaced volume; T_r, P_r and V_r are the state properties at a reference point (e.g. IVC); P_{mot} is the motored in-cylinder pressure.

The mean piston speed is calculated as

$$\bar{S}_p = 2LN,$$

where N is the rotational speed of crankshaft (rad/s); α, C_1 and C_2 are calibration parameters.

2.4 Reaction-Based model validation

A single-step and two-step models are developed in Simulink based on the reaction-based modeling approach described in Section 2.3. To validate the modeling method, the developed models are first compared to a simple GT-POWER model. The models are first calibrated in an open-loop manner, which doesn't account for temperature feedback. After a set of reasonable parameters are obtained, the effect of temperature is considered. The preliminary calibration and validation process has shown that the two-step model is capable of accurately estimating combustion metrics under various engine operating conditions.

2.4.1 Continuous-time model

In the continuous-time simulation, it is convenient to run the simulation from IVC to EVO, where a closed thermodynamic model can be formulated. For the specific engine that has been simulated, the simulation duration is from 132CA BTDC to 132CA ATDC. The initial conditions such as initial temperature, initial pressure, initial gas mixture and its properties are coordinated with the data generated by the GT-POWER model. Instant volume and its derivative are given as input signals derived from Sine functions, and also depend on the engine geometry and engine speed. The fuel injection profile is given by the GT-POWER model, which is determined in terms of total mass of fuel injected, mass flow rate, and pulse width for each injection. This will ensure that the injection profiles for both reaction-based model and GT-POWER model are identical.

The calibration approach is illustrated in Figure 2.6. The reaction-based model is a highly coupled dynamic system. So the basic idea here is to decouple the whole system before we actually calibrate it. To be more specific, we divide the closed-loop system into two parts: 1) the open-loop reaction rate calculation and 2) the open-loop temperature calculation.

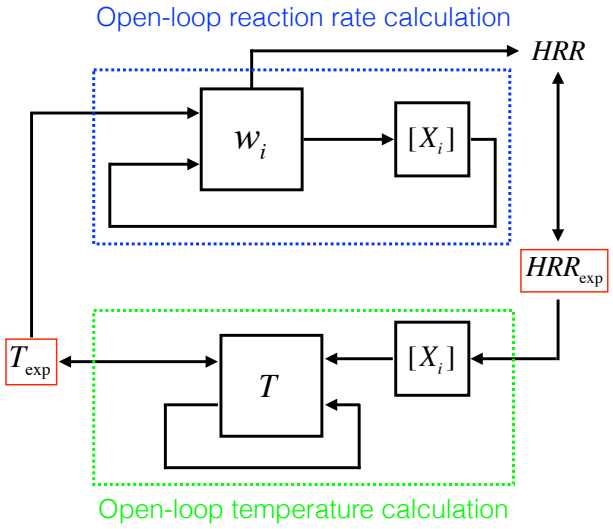

Figure 2.6: Model calibration approach

For the first part, we use the temperature data from the GT-POWER model as the

input signal and calculate the reaction rates. Then the heat release rate, which is a function of the reaction rates, will be compared to the "ideal" heat release rate, which is also from the GT-POWER model. In this way the coefficients in the reaction rate equations can be calibrated. This part will be illustrated in detail in the following sections. For the latter part, we can always perform the similar but reverse process to calibrate the temperature model. However, a more convenient way is to compare the temperature under motoring condition, so that the reaction rate won't affect the temperature calculation. Once the temperature model is calibrated for the motoring condition, no further calibration is necessary for models with different reaction steps. However, the model might need to be re-calibrated if a different engine is applied.

The single-step model has six states: the temperature, T, the concentrations of diesel fuel, $[C_{10.8}H_{18.7}]$, oxygen, $[O_2]$, nitrogen, $[N_2]$, carbon dioxide, $[CO_2]$, and water, $[H_2O]$. The general rate equations are given in Section 2.3. The first step is to apply the parameters from the references [13] to see if that works, and then to tune E_A/R_u so that the start of combustion coordinates with GT-POWER model. Finally A is tuned to maintain the magnitude of the rate to be within a reasonable range. m and n are essentially fixed. The calibrated coefficients in equation (2.33) are given in Table 2.1.

Table 2.1: Arrhenius rate parameters for single-step model

Parameters	Values
A	8000
E_A/R_u	17098
m	0.1
n	0.25

The single-step model verified that the reaction-based model is capable of estimating the combustion metrics over a certain range. However, the single-step model is too simple and doesn't provide acceptable predictions even for individual case. The peak heat release rate is always over-predicted if the combustion phasing is matched. Thus, our focus will be on the two-step model.

The two-step model includes seven states: the temperature, T, the concentrations of diesel fuel, [$C_{10.8}H_{18.7}$], oxygen, [O_2], nitrogen, [N_2], carbon dioxide, [CO_2], water, [H_2O], and carbon monoxide, [CO]. The general differential equations are given in Section 2.3. The calibration process is almost the same for the two-step model although there are two rate equations and more coefficients to consider. Note that A_1 and A_2 are chosen to vary for different engine operating conditions, such as engine speed, engine load and injection profile. The calibrated coefficients in equation (2.36) are given in Table 2.2.

Table 2.2: Arrhenius rate parameters for two-step model

Parameters	Values
A_1	varying
A_2	varying
A_3	5×10^8
$E_{A,1}/R_u$	15098
$E_{A,2}/R_u$	20130
m_1	0.1
m_2	1
n_1	1.65
n_2	0.25
k_1	0.5
k_2	1

The four-step model includes eight states: the temperature, T, the concentrations of diesel fuel, [C_nH_{2n+2}], oxygen, [O_2], nitrogen, [N_2], carbon dioxide, [CO_2], water, [H_2O], carbon monoxide, [CO], and hydrogen, [H_2]. The general differential equations are given in Section 2.3. The calibrated coefficients in equation (2.39) are given in Table 2.3 [13].

Table 2.3: Arrhenius rate parameters for four-step model (propane)

Rate equations	2.39a	2.39b	2.39c	2.39d
x	17.32	14.7	14.6	13.52
E_A/R_u	24962	25164	20131	20634
a	0.50	0.90	1.0	0.85
b	1.07	1.18	0.25	1.42
c	0.40	-0.37	0.50	-0.56

2.4.2 GT-POWER DIPulse model

A simple GT-POWER predictive diesel combustion model is developed and used for generating baseline simulation data for calibrating the developed model. The GT-POWER engine model describes a single cylinder direct injection diesel engine with a reaction-based combustion model (see Figure 2.7). The parameters are mostly set as default values.

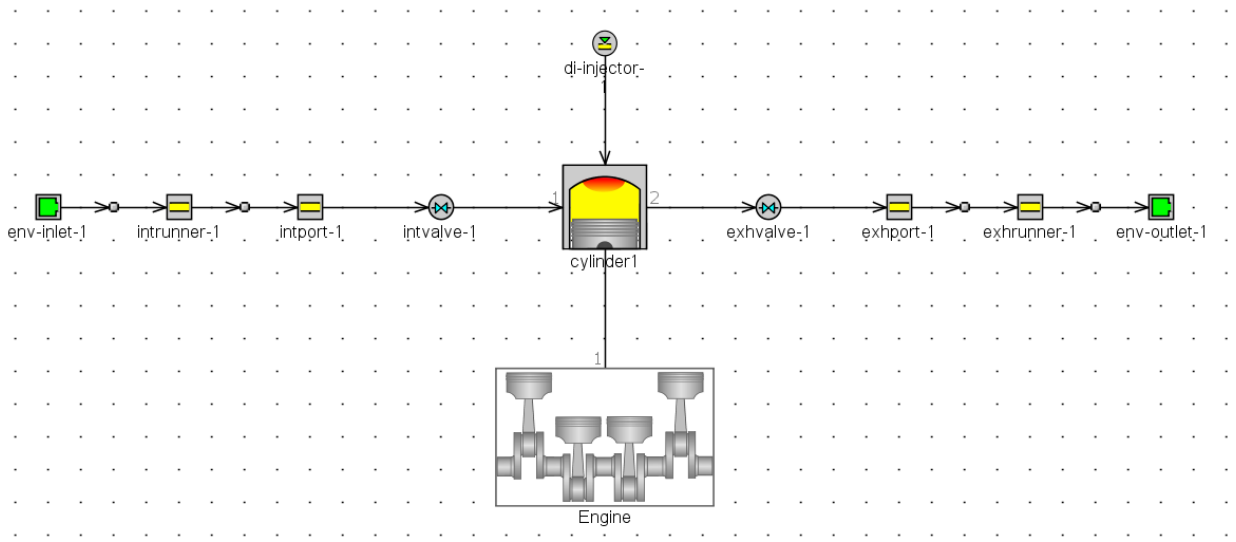

Figure 2.7: GT-POWER single-cylinder engine model with predictive combustion

The GT-POWER model is used to generate the engine combustion data over the entire engine operational map with different fuel injection properties, including injection timings and quantities of pre-injection, main injection, and multiple after injections. There are 4 calibration parameters in GT-POWER DIPulse predictive combustion model:

1) Entrainment Rate Multiplier

2) Ignition Delay Multiplier

3) Premixed Combustion Rate Multiplier

4) Diffusion Combustion Rate Multiplier

The combustion rate is calculated in a similar way as the Arrhenius function-based model:

$$\frac{dm_k}{dt} = CMBMULT * \phi * (3-\phi)^2 * p^{2.5} * \exp(-\frac{4000}{T}) \tag{2.46}$$

where m_k is the mass of fuel in the mixed zone, $CMBMULT$ is the combustion rate multiplier, ϕ is the equivalence ratio, p is the pressure and T is the temperature.

Table 2.4 shows the engine geometry and parameters used in GT-POWER model, which is coordinated with the experimental setup.

Table 2.4: GT-POWER engine geometry and model parameters

Parameters	Values
Bore (mm)	100
Stroke (mm)	100
Connecting Rod Length (mm)	180
Compression Ratio	18
TDC Clearance Height (mm)	0.5
CA at IVC	-132
Heat Loss Model	WoschniGT
Combustion Model	EngCylcombDIPulse

2.4.3 Preliminary calibration results

The reaction-based combustion model was validated in several steps. Firstly, we run simulations under different engine speeds and loads following a 5×5 engine calibration matrix. All the other control variables were fixed. Secondly, we studied the behavior of the model under different injection timing, for both main injection and the late-injection, for fixed engine speed and load. Thirdly, additional model validation were completed, including EGR sweep and air-fuel ratio sweep. In addition, the model was validated with experimental data, although only for 3 engine operating conditions. The results showed that A_1 and A_2 are closely related to these engine operating conditions, with smooth variations. Thus, it is possible to model A_1 and A_2 as functions of engine speed, engine load and injection timing.

2.4.4 Variable engine speed and load, fixed injection timing

This subsection studies the reaction-based model calibration over a given engine operational map. The main purpose is to find out what is the key calibration parameters required for calibrating the reaction-based model working over the engine map.

Figure 2.8 shows the calibration results for the 5×5 engine speed and engine load matrix. Table 2.5 shows the IMEP error for each operating condition. Table 2.6 shows the output torque error for each operating condition. All the errors are calibrated within 3%. Figure 2.9 shows the calibration coefficients to achieve this match.

Table 2.5: Relative error for IMEP from -132CA to 132CA (%)

	50 mg	60 mg	70 mg	80 mg	90 mg
1000 r/min	2.75	1.87	1.85	0.60	0.75
1500 r/min	2.50	0.31	2.70	1.51	2.50
2000 r/min	1.11	0.50	2.06	1.11	2.42
2500 r/min	1.46	2.48	1.46	2.68	2.37
3000 r/min	0.49	2.74	2.93	2.84	2.50

Table 2.6: Relative error for output torque (%)

	50 mg	60 mg	70 mg	80 mg	90 mg
1000 r/min	16.5	9.67	6.20	7.55	11.0
1500 r/min	15.5	6.39	2.21	5.22	1.04
2000 r/min	3.75	1.22	2.63	1.87	2.64
2500 r/min	3.12	1.83	3.10	2.86	3.68
3000 r/min	2.87	2.52	1.54	1.69	2.39

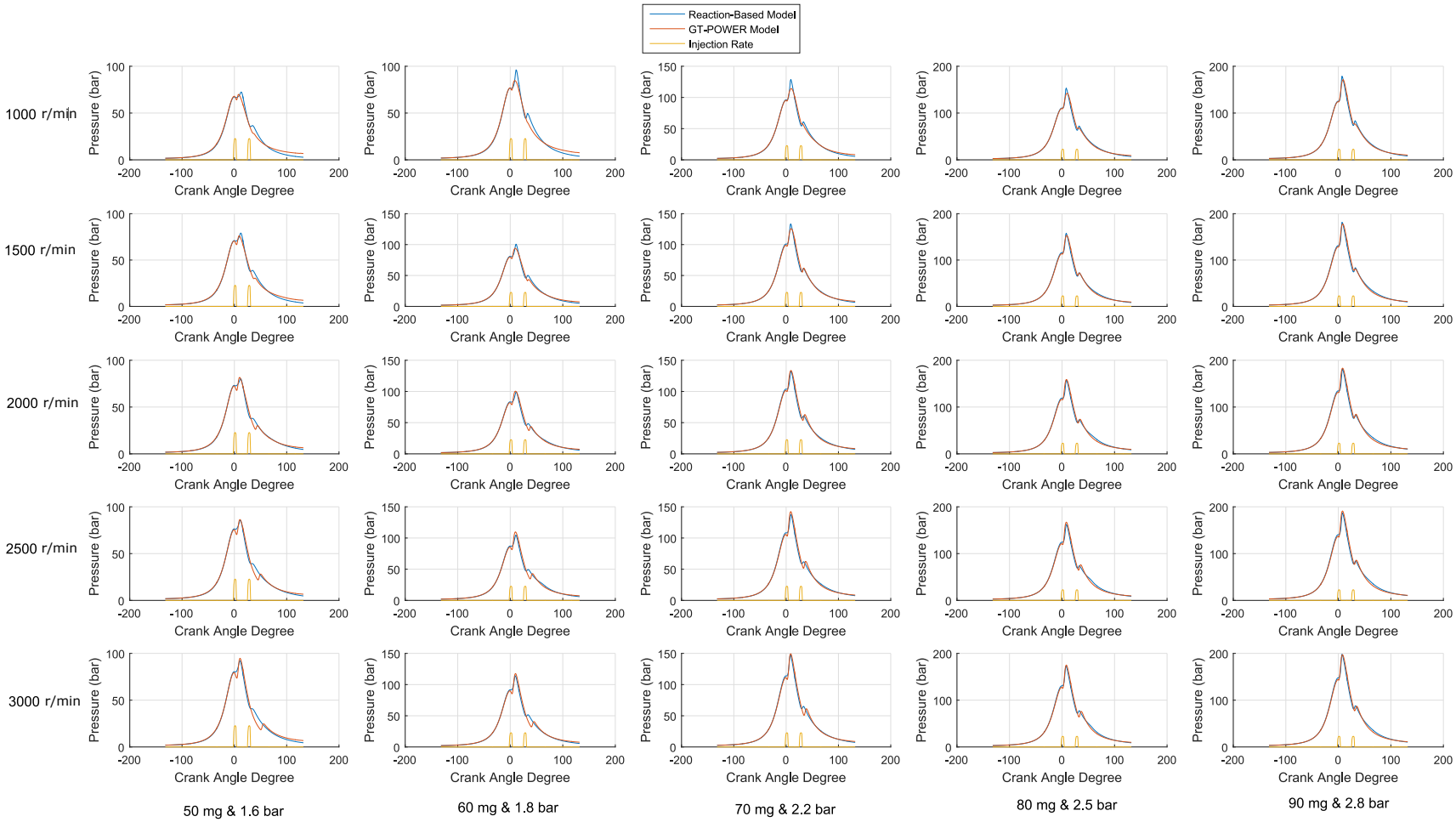

Figure 2.8: In-cylinder pressure for the two-step and GT-POWER models under 5×5 engine operation matrix

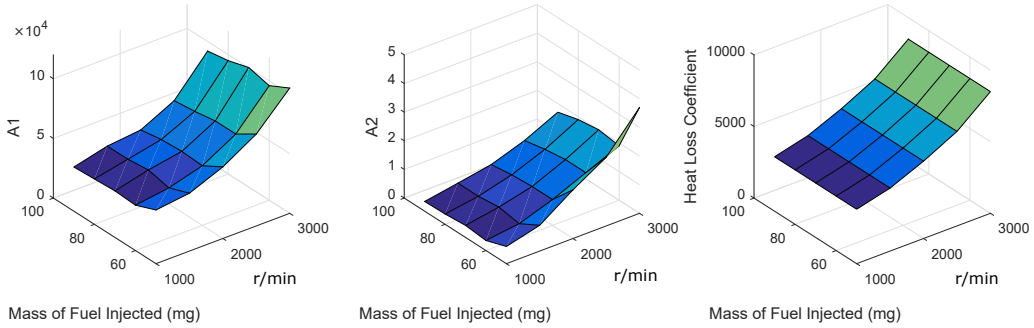

Figure 2.9: Calibration coefficients for the two-step model

From this preliminary study, it is concluded that model parameters A_1 (2.36a) and A_2 (2.36b) need to be calibrated as the functions of engine speed and load.

2.4.5 Variable injection timing, fixed engine speed and load

Figure 2.10 shows the in-cylinder pressure curves from the reaction-based model and GT-POWER model for main injection at 10 CAD BTDC, TDC and 5 CAD ATDC, respectively. The late-injection timing was set to 25 CAD after main injection. The engine was running at 1500 r/min with 50 mg of total injected fuel mass. The results showed that very little re-calibration effort was needed for a fairly good match. The calibrated parameters are A_1 and/or A_2.

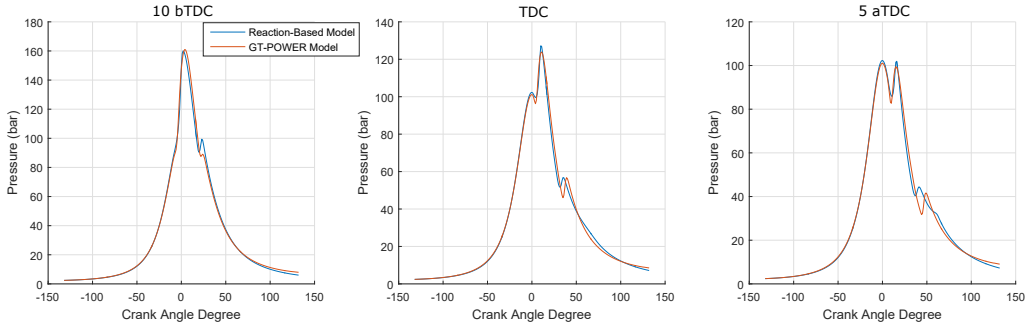

Figure 2.10: In-cylinder temperature and pressure for the two-step and GT-POWER models with different main injection timing

Figure 2.11, 2.12, 2.13, 2.14, 2.15 and 2.16 are the in-cylinder temperature and pressure

plots from the two-step model with different injection profiles, compared with that from GT-POWER model at engine speed of 1500 r/min. There are two injections in this combustion event: one main injection at 355 CAD and one late injection with various timings. For each injection, the injected mass of fuel is 40 mg/hub.

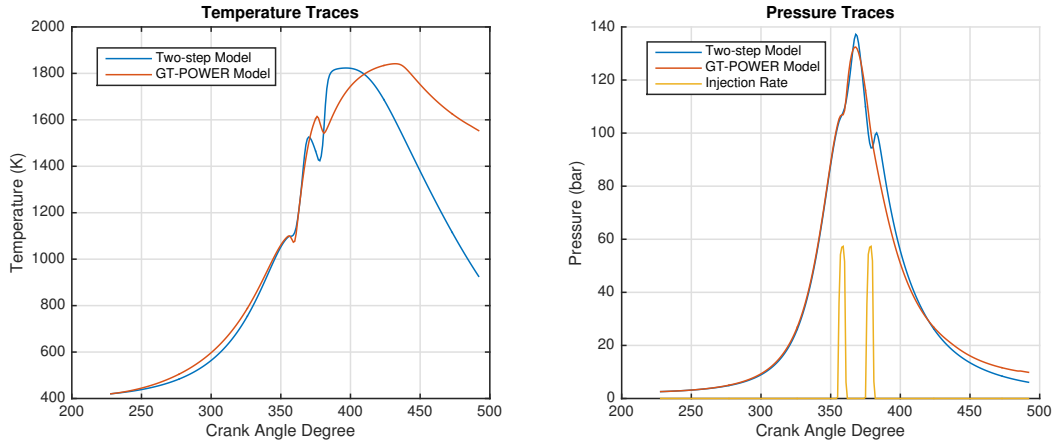

Figure 2.11: In-cylinder temperature and pressure for the two-step and GT-POWER models with late injection at 15 CAD ATDC

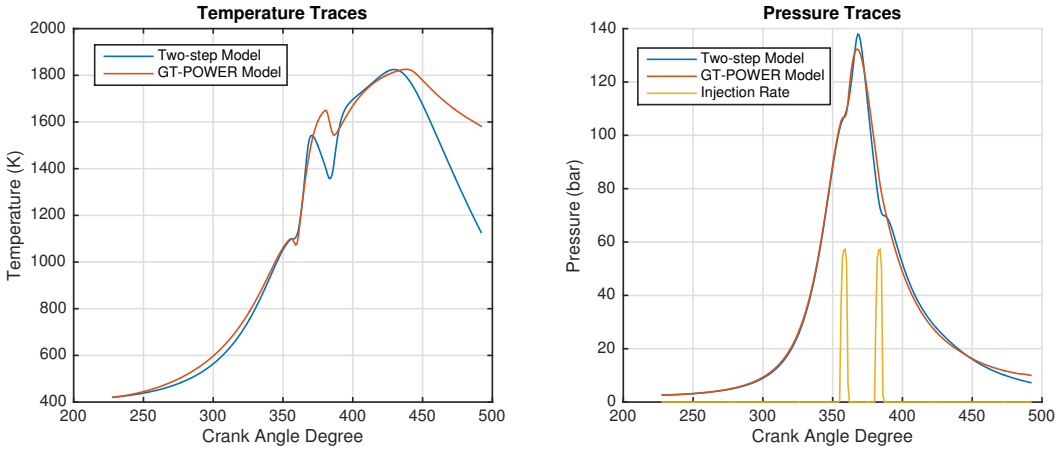

Figure 2.12: In-cylinder temperature and pressure for the two-step and GT-POWER models with late injection at 20 CAD ATDC

The overall shape of the pressure curve from the two-step model matches well with GT-Power simulation results. The effect of late injection to in-cylinder pressure is well predicted. However, the over-predicted peak pressure indicates that there are still corrections to be

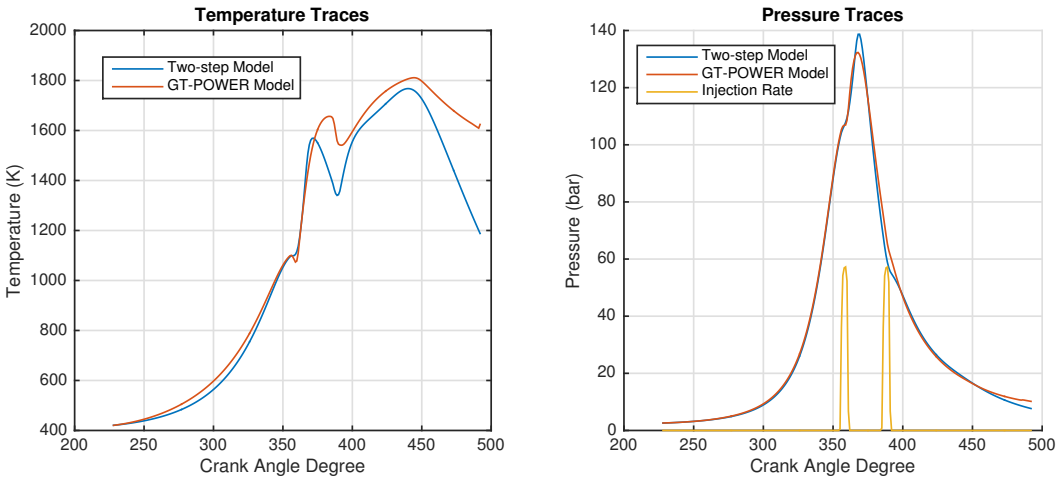

Figure 2.13: In-cylinder temperature and pressure for the two-step and GT-POWER models with late injection at 25 CAD ATDC

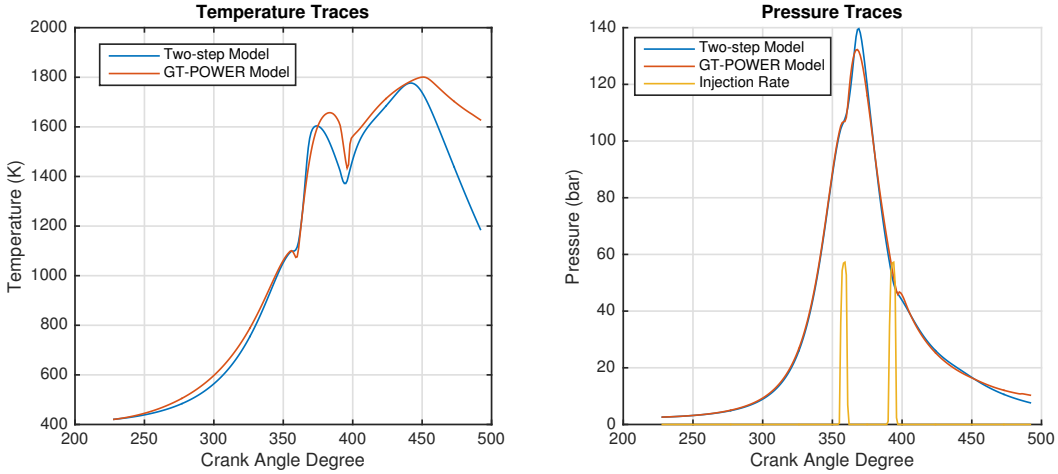

Figure 2.14: In-cylinder temperature and pressure for the two-step and GT-POWER models with late injection at 30 CAD ATDC

made. Note that the temperature after the second injection does not match well between the reaction-based and GT-POWER models, especially when the second injection time is heavily retarded. This could be due to the inaccuracy of GT-POWER DIPulse model. One observation is that the ignition delay is extremely large for the GT-POWER simulations; see Figure 2.15. The calculated indicated mean effective pressure (IMEP) and its error are shown in Table 2.7. Note that we only need to correlate A_2 with the injection timing to get

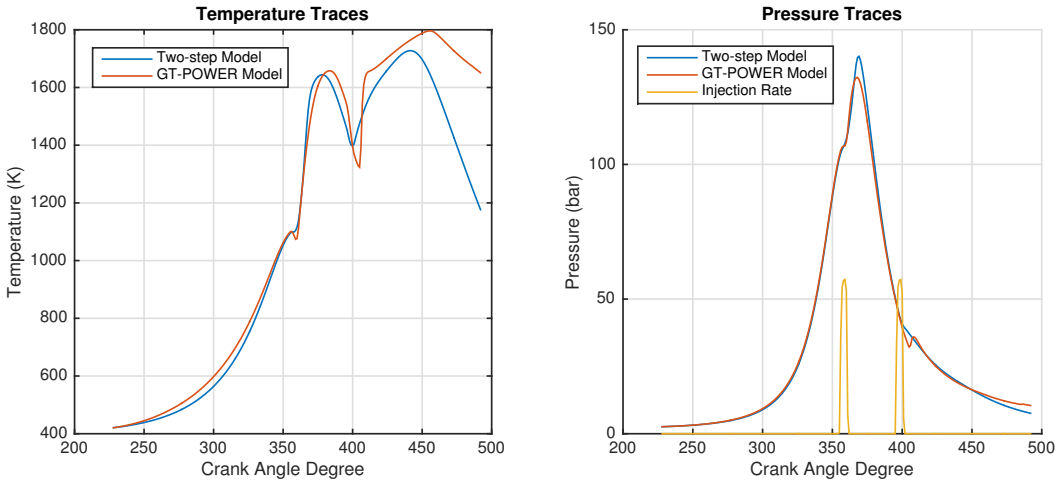

Figure 2.15: In-cylinder temperature and pressure for the two-step and GT-POWER models with late injection at 35 CAD ATDC

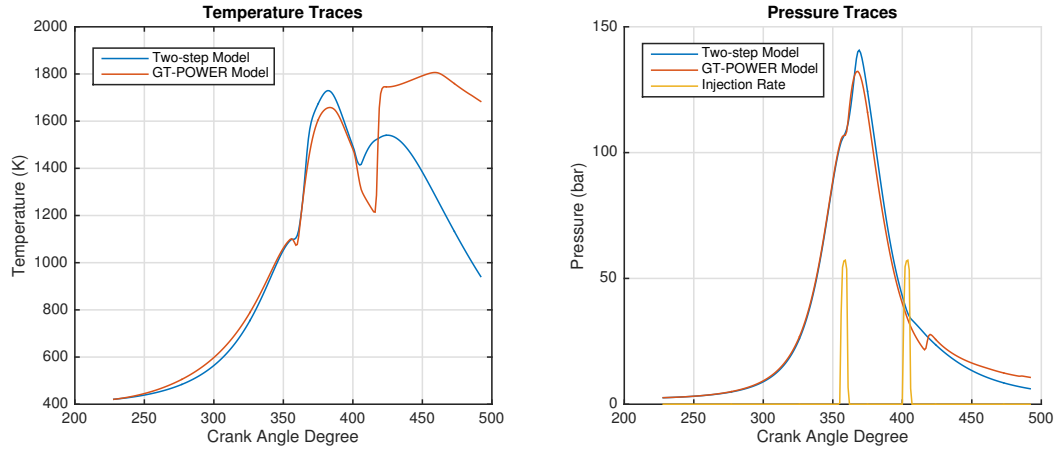

Figure 2.16: In-cylinder temperature and pressure for the two-step and GT-POWER models with late injection at 40 CAD ATDC

a good match.

2.4.6 EGR sweep

Figure 2.17 shows the in-cylinder pressure under different EGR ratios. The selected operating points of EGR ratio are 15%, 20%, 25% and 30%.

Table 2.7: IMEP (bar) from -132 CAD to 132 CAD

Injection Timing	IMEP_{RB}	IMEP_{GT}	Relative Error	A_2
15° ATDC	16.2477	16.2712	0.14%	1.06
20° ATDC	16.0589	15.8008	1.63%	1.79
25° ATDC	15.1928	15.3863	1.26%	2.68
30° ATDC	15.0783	15.0184	0.40%	3.30
35° ATDC	15.0079	14.6032	2.77%	3.60
40° ATDC	13.9484	13.9833	0.25%	3.80

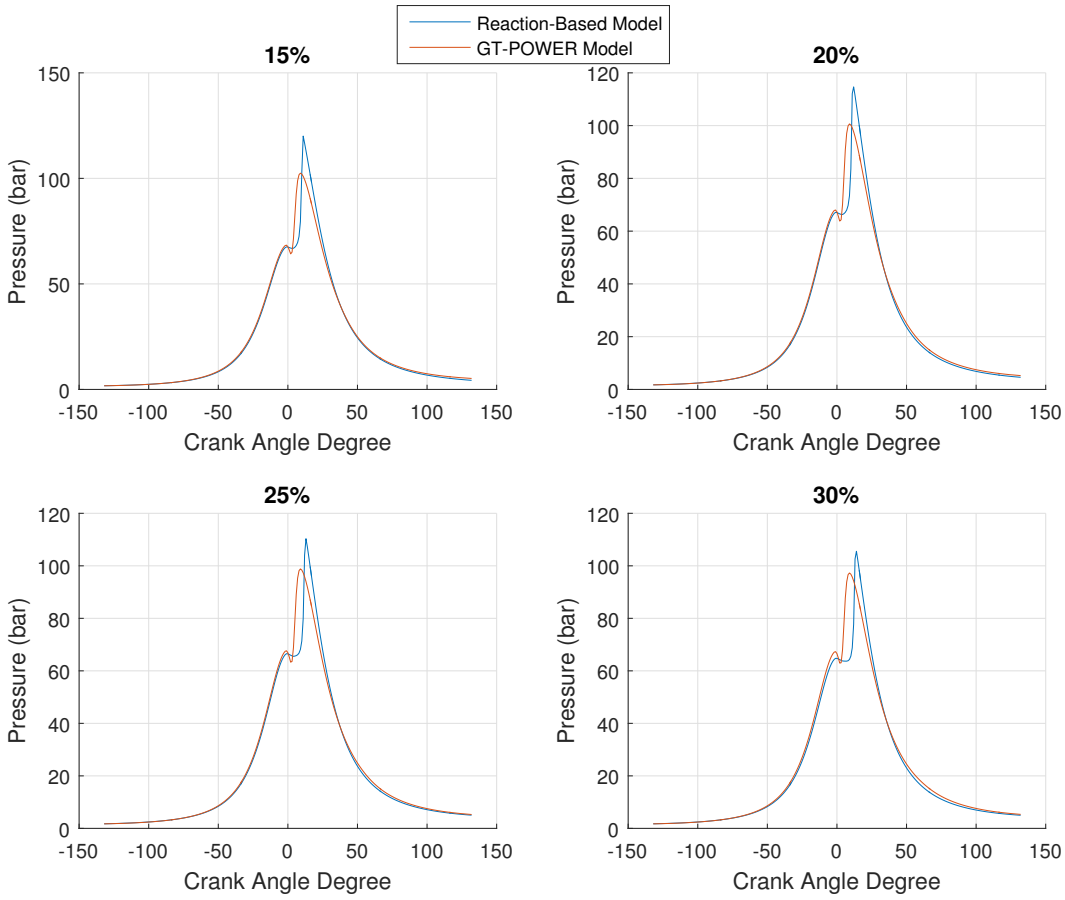

Figure 2.17: In-cylinder temperature and pressure for the two-step and GT-POWER models with different EGR ratio

2.4.7 Air-Fuel ratio sweep

The last validation step is to compare the model behavior under different air-fuel ratio (AFR) conditions. The three cases are based on different boost pressure: 1.4 bar, 1.6 bar and 1.8

bar. The engine was running at 1500 r/min. There were two injections: one main injection at -2 CAD and one late-injection at 25 CAD. The total mass of fuel injected was 50 mg/hub.

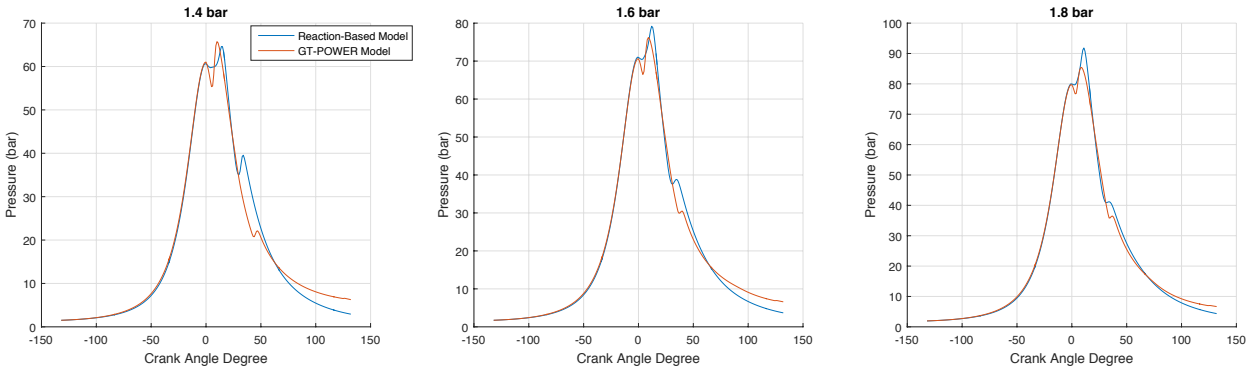

Figure 2.18: In-cylinder temperature and pressure for the two-step and GT-POWER models with different air-fuel ratio

There was not much recalibration effort necessary to obtain the matched pressure curve to achieve less than 3% relative error in IMEP. The calibrated parameters are A_1 and/or A_2.

2.4.8 Notes

From the results of preliminary calibration of the reaction-based model, some general ideas and insights of comprehensive calibrations are obtained:

1) For the fixed point calibration (that is, the model is set at fixed speed, load, injection mass, injection timing and EGR rate) the model parameters can be calibrated to estimate the combustion metrics.

2) To have a model that covers a wide range of engine operating conditions, some of the parameters need to be function of engine control inputs.

3) The engine speed, load, main injection timing and EGR rate are the most effective factors that force the parameters to change, while multiple injections and air-fuel ratio do not affect the parameters so much.

4) It is therefore necessary to first study the sensitivity of the model to all the parameters. By eliminating the least sensitive parameters, the overall calibration effort can be significantly reduced.

5) These parameters to be calibrated need to be formulated as functions of engine speed, load, main injection timing, and EGR rate, either as lookup table or polynomials.

6) The fully calibrated model should be able to accurately predict engine output torque (or IMEP) with any given engine control input.

2.5 Model calibration

The reaction-based model has been developed in MATLAB/Simulink and compared with a GT-POWER model. The next step is to evaluate and further enhance the developed reaction-based combustion model using engine test data set provided by GM. The evaluation process is divided into two steps: initial reduced data set evaluation and final full data evaluation. The reduced data set evaluation results are used to guide the further model enhancement and the enhanced model is used for final model evaluation.

The workflow of the model calibration is summarized as follows:

1) The model sensitivity with respect to each parameter is studied. The most sensitive parameters are selected as candidates for calibration, while the rest are kept constant.

2) An automated optimization algorithm is implemented. The algorithm is able to handle multiple parameters and objects. The cost function is defined and weightings are properly selected.

3) The data set is used for fixed point calibration, and lookup tables are generated. The smoothness of the calibration surface is also studied.

4) A calibration structure is developed.

5) For parameters with a smooth calibration surface, polynomial functions are generated to match the calibration data. Multi-case algorithm is used to optimize the polynomial coefficients.

6) The model is finalized by combining all the lookup tables and polynomial functions.

7) A final model evaluation is processed on the finalized model and conclusions are drawn from the results.

2.5.1 Sensitivity analysis

The calibration process is essentially parameter estimation. Parameters that exert the most influence on model responses are identified through a "sensitivity analysis" [19]. By calculating and comparing the sensitivity coefficients of all the parameters, a list, called "sensitivity ranking", can be obtained. For the same model, different sensitivity analysis methods will result in different sensitivity rankings. However, the actual ranking is not as important as these parameters consistently appear near the top of the list. Disagreement among rankings by the various methods for variables of lesser importance is not of practical concern since these variables have little or no influence on model outputs.

For the developed reaction-based model, the one-at-a-time method is used. Conceptually, this method is to repeatedly vary one parameter at a time while holding the others fixed. A sensitivity ranking can be obtained quickly by increasing each parameter by a given percentage while leaving all others constant, and quantifying the change in model output.

To be more specific, suppose there are n parameters, the sensitivity coefficient of system

response η_i to parameter β_j can be approximated as

$$\begin{aligned} s_{i,j} &= \beta_j \frac{\partial \eta_i}{\partial \beta_j} \\ &\approx \beta_j \frac{\eta_i\left(\beta_1, ..., (1+\delta)\,\beta_j, ..., \beta_n\right) - \eta_i\left(\beta_1, ..., \beta_j, ..., \beta_n\right)}{(1+\delta)\,\beta_j - \beta_j} \\ &= \frac{\eta_i\left((1+\delta)\,\beta_j\right) - \eta_i\left(\beta_j\right)}{\delta} \end{aligned} \tag{2.47}$$

where δ is the relative perturbation and in this study $\delta = 0.001$.

The sensitivity coefficients of all the parameters are calculated for a variety of engine operating conditions. It turns out that the most significant (sensitive) parameters remain the same for all the tested points. As an example, the results of 680 r/min, 1 bar are shown in Table 2.8. The system response chosen in this study is the cylinder pressure because it is directly measured in test data. However, other system variables can also be studied. The sensitivity in the table is the mean value over the entire tested cycle. The percentage of the sensitivity coefficients with respect to the mean value of nominal cylinder pressure, which is not perturbed, is calculated to evaluate the relative significance of each parameter. The results show that $E_{A,1}$, $E_{A,2}$ and n_1 are the parameters with percentage sensitivity greater than 5%. Figure 2.19 shows the plots of crank-based sensitivity coefficients of $E_{A,1}$, $E_{A,2}$ and n_1. The shape of $E_{A,1}$ and n_1 are very similar, which indicates that only one of the two parameters needs to be calibrated. As a result, the parameters to be fully calibrated are $E_{A,1}$ and $E_{A,2}$.

Table 2.8: Sensitivity coefficients of parameters

Parameters	A_1	A_2	A_3	$E_{A,1}$	$E_{A,2}$	m_1	n_1	m_2	n_2	k_1	k_2
Sensitivity	0.18	0.11	0.00	3.60	2.15	0.13	0.83	0.53	0.08	0.18	0.01
Percentage (%)	1.63	0.95	0.01	32.25	19.34	1.18	7.43	4.75	0.68	1.58	0.05

2.5.2 Overview of experimental data

The experimental data to be used for calibration is from a GM 6.6 L, 8 cylinder, Duramax engine. The specifications of the engine is summarized in Table 2.9. The engine was

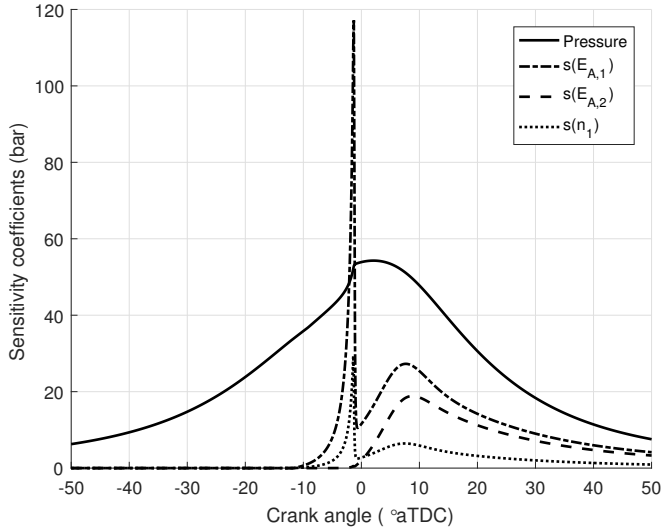

Figure 2.19: Sensitivity coefficients of most significant parameters

tested at steady-state under various speed and load conditions. The recorded test data includes in-cylinder pressure traces and other engine control inputs, along with post-processed heat-release traces, air and EGR variables, pressure metrics such as IMEP (indicated mean effective pressure) and NMEP (net mean effective pressure).

Table 2.9: Engine specifications

Parameter	Model value
Bore	103 mm
Stroke	99.05 mm
Connecting rod length	163 mm
Compression ratio	16.4:1
Intake valve duration	148 CAD
Exhaust valve duration	244 CAD

The available test data is summarized in Table 2.10 with three test data sets described as follows.

Test Set #1: Engine map

- 16 operating points (OP) over the speed-load map.

Table 2.10: Summary of the experimental data

Operating point		BMEP kPa	q_{inj} mm^3	SOI_{main} °bTDC	EGR %
Engine map	Max	801.2	48.0	19	71.9
	Min	57.1	8.2	TDC	49.0
680 × 9	Max	101.2	12.0	25	70.9
	Min	98.7	10.1	TDC	70.3
1400 × 9	Max	252.0	23.5	25	65.0
	Min	248.4	19.2	2	61.6
1400 × 10	Max	502.2	38.1	25	53.4
	Min	496.4	33.3	-3	49.7
2000 × 9	Max	709.7	41.6	20	48.6
	Min	690.9	30.7	-3	45.2
1400 × 45	Max	270.3	19.2	12	65.8
	Min	131.8	18.7	-2	4.2

- Engine operated as calibrated at each OP with combustion inputs (fuel injection timings, EGR, air-fuel ratio, etc.) from speed-fuel maps and varied based on OP.
- main injection used for most key points and post injection used at certain high-load OPs.
- An addition data set under the same conditions but with additional pilot injection for comparison purpose.

Test Set #2: SOI sweeps at fixed speed and load

- 4 speed-load pairs: 680 r/min, 1 bar; 1400 r/min, 2.5 bar; 1400 r/min, 5 bar; 2000 r/min, 7 bar.
- Main injection only for 680 r/min and 1400 r/min and additional post injection included at 2000 r/min.
- Fixed EGR level for each speed-load pair.

Test Set #3: SOI sweeps with constant fuel quantity

- Constant mass of fuel injected at 1400 r/min.
- Different EGR levels.

2.5.3 Automated calibration algorithm

The first step is to individually calibrate the whole data set, either manually or automatically, in order to confirm the two selected parameters are sufficient to achieve acceptable model performance. Test Set #1 is first used to manually calibrate the model. As a result, the IMEP error can be made arbitrarily small while pressure and temperature traces are kept close enough to those in test data. An automated optimization algorithm is developed to reduce the manual effort for individual calibration. The developed code is further implemented for multi-case calibration, where the optimized parameters work for multiple operating conditions. The algorithm is based on *lsqnonlin*, a MATLAB nonlinear optimization function [20]. The function solves nonlinear Least-Squares curve fitting problems of the form

$$\min ||f(x)||_2^2 = \min \left[f_1(x)^2 + f_2(x)^2 + \ldots + f_n(x)^2 \right] \tag{2.48}$$

where the cost function $f(x)$ is in the following form

$$f(x) = \begin{bmatrix} f_1(x) \\ f_2(x) \\ \vdots \\ f_n(x) \end{bmatrix} = \begin{bmatrix} W_P^{0.5} \left(\frac{P - P_{exp}}{P_0} \right) \\ W_T^{0.5} \left(\frac{T - T_{exp}}{T_0} \right) \\ W_{IMEP}^{0.5} \left(\frac{IMEP - IMEP_{exp}}{IMEP_0} \right) \\ W_{MFB}^{0.5} \left(MFB - MFB_{exp} \right) \end{bmatrix} \tag{2.49}$$

where P_{exp}, T_{exp}, $IMEP_{exp}$ and MFB_{exp} are crank-based time series in column vector from experimental data. P_0, T_0 and $IMEP_0$ are normalizing factors. W_P, W_T, W_{IMEP} and W_{MFB} are weighting factors.

For the individual calibration, x is the vector containing the parameters, i.e.

$$x = \begin{bmatrix} E_{A,1} \\ E_{A,2} \end{bmatrix} \tag{2.50}$$

As an example, Figure 2.20a shows the predicted in-cylinder pressure compared to experimental data at 1400 r/min, 2.5 bar. The model successfully predicts the combustion phasing, pressure rise, peak pressure and pressure drop. However, there is a difference in pressure near the onset of combustion. Since the two-step mechanism does not account for the dissociation of large hydrocarbon molecules into small hydrocarbon molecules, the heat absorption due to the dissociation was not modeled, resulting in higher pressure rise around the start of combustion. The corresponding temperature (Figure 2.20b), mass-fraction-burned (Figure 2.21a) and heat release rate (Figure 2.21b) are shown in the following. The overall shape of the predicted temperature is in good agreement with experimental data, although there is a discrepancy in the compression stroke near top dead center, peak temperature and exhaust gas temperature. The large temperature drop at the end of combustion is due to the over-estimated heat release rate as shown in Figure 2.21a and Figure 2.21b.

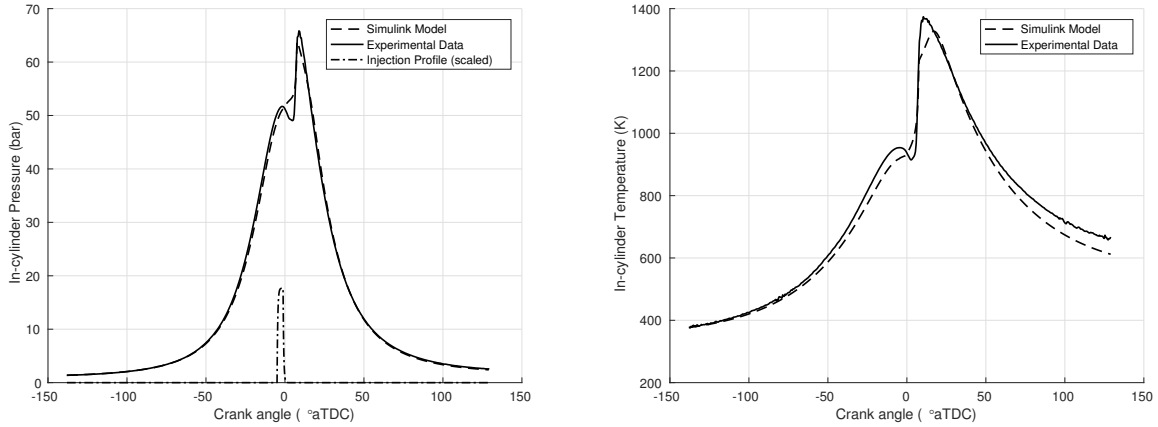

(a) In-cylinder pressure

(b) In-cylinder temperature

Figure 2.20: Pressure and temperature predictions at 1400 r/min, 2.5 bar

The first peak in the heat release rate refers to the first step of the chemical reaction. The model predicted an earlier start of heat release but a delayed and steep rising. After a short duration, the first step terminated and the second step initiated. The heat release rate of the second step was also over-predicted since there is a peak in the predicted curve while the experimental data shows a dip. In the mass-fraction-burned plot, it is worth noting that

the model accurately predicted the combustion incompleteness, where the MFB does not reach 1 at the end of combustion. Note that a Wiebe-based combustion model is not able to predict this phenomenon. It also shows an earlier completion of combustion compared to the experimental data.

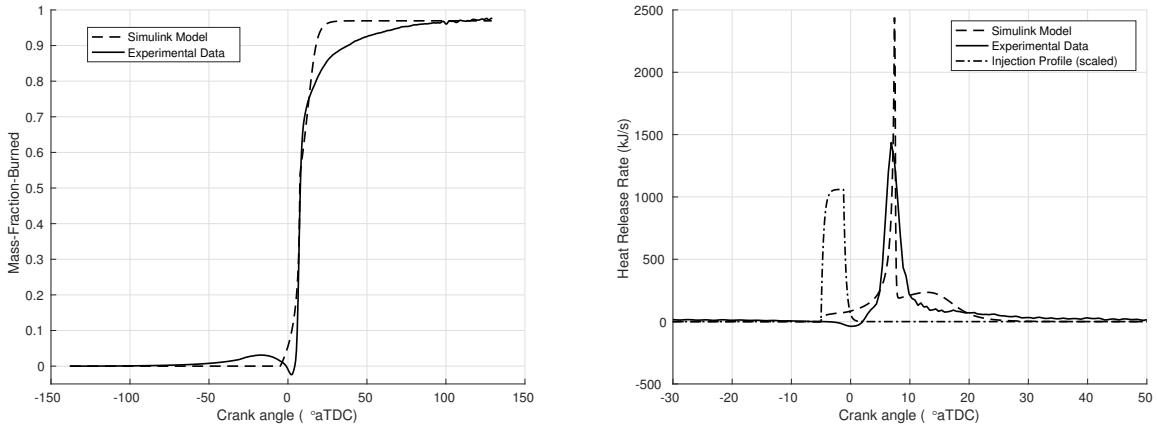

(a) Mass fraction burned (b) Heat release rate

Figure 2.21: MFB and HRR predictions at 1400 r/min, 2.5 bar

The IMEP error was kept within 5% throughout the calibration process. It can be confirmed that a two-step model is capable of capturing the main combustion features but is simple enough for real-time model-based control.

2.5.4 Individual calibration

The results of individual calibration is shown in Figure 2.22 over the engine map, Figure 2.23 for SOI sweep at 4 operational conditions, and Figure 2.24 for SOI sweep at 1400 r/min with constant fuel. All the test points are within 5% error bound. In fact, the relative IMEP error for each test point is kept within 1%.

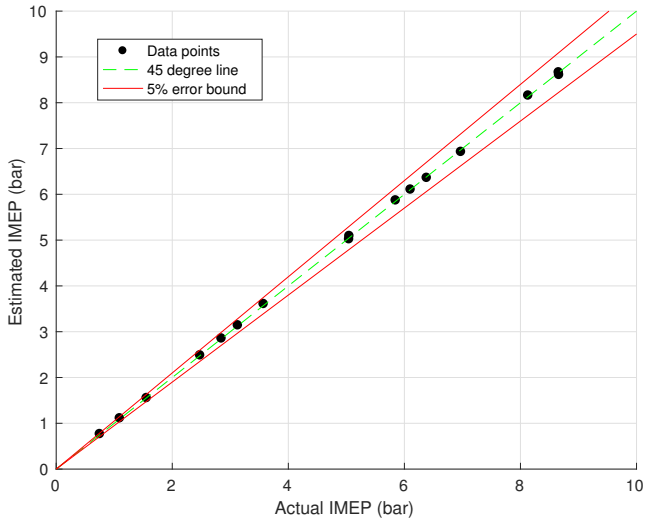

Figure 2.22: Estimated vs. actual IMEP over the engine map

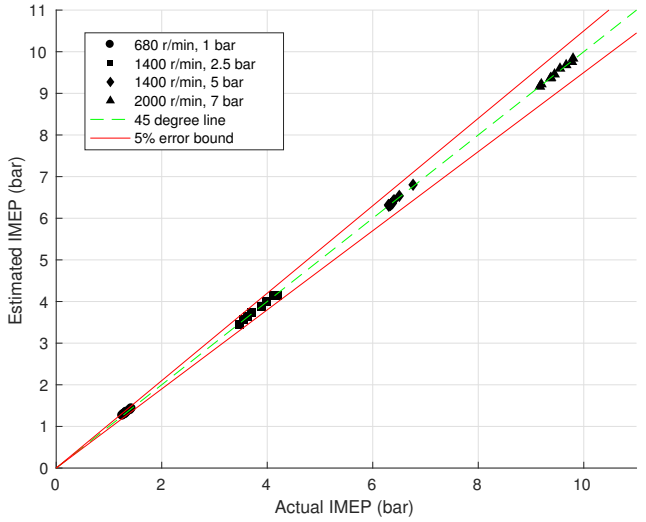

Figure 2.23: Estimated vs. actual IMEP for SOI sweep at 4 operating conditions

2.5.5 Parameter correlations

Cases of fixed speed-load pairs were studied by calibrating the same set of coefficients. In spite of several outliers, the coefficients are shown to be correlated to SOI and engine operating conditions.

As shown in Fig. 2.25, $E_{A,1}$ is small for very advanced injection and rises as the injection

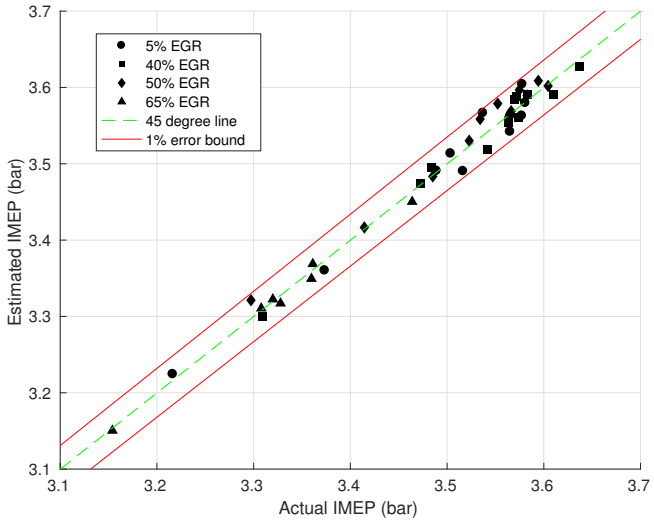

Figure 2.24: Estimated vs. actual IMEP for SOI sweep at 1400 r/min with constant fuel

timing gets more retarded. For injections at 5 to 10 degree before TDC, $E_{A,1}$ reaches its peak. As the injection is further retarded, $E_{A,1}$ decreases. Although the correlation between $E_{A,1}$ and SOI is not close to linear, a clear trend of $E_{A,1}$ increasing as load getting higher is shown. The maximum relative variation of $E_{A,1}$ is 14.7%.

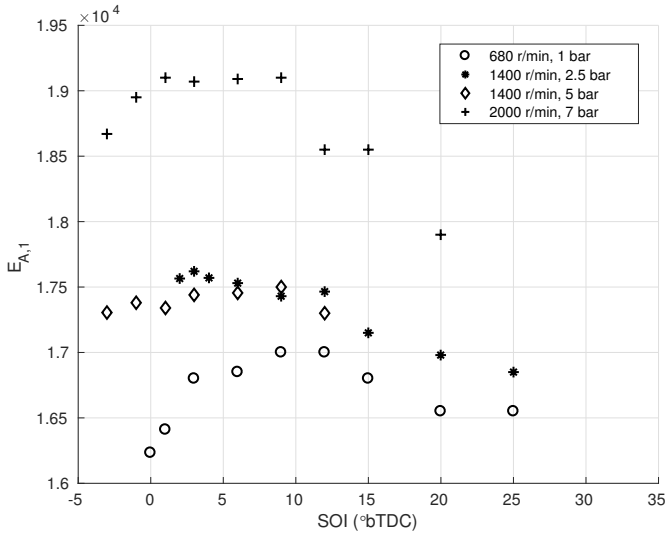

Figure 2.25: Calibrated $E_{A,1}$ vs. SOI for different speed-load pairs

Fig. 2.26 shows the variation of $E_{A,2}$ with respect to SOI. A close-to-linear correlation is

observed. However, at 1400 r/min with 5 bar load, $E_{A,2}$ is lower than expected in general, especially when the injection is extremely advanced.

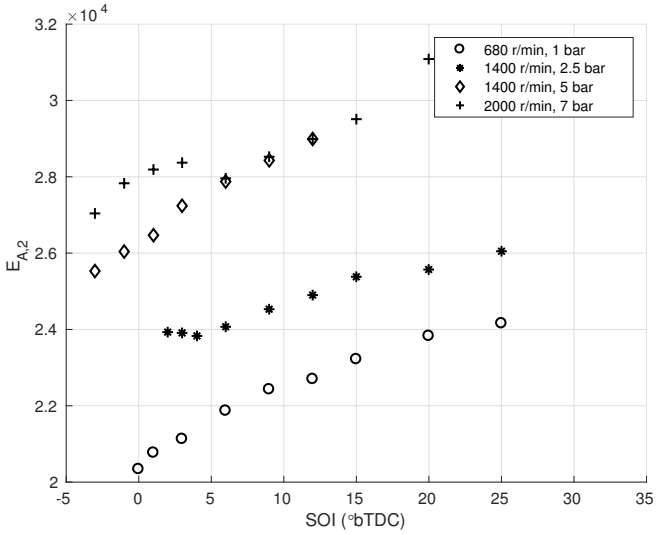

Figure 2.26: Calibrated $E_{A,2}$ vs. SOI for different speed-load pairs

The coefficients were also calibrated at the 1400 r/min with constant quantity of fuel injection. In this case, there were 4 EGR levels: 5%, 40%, 50% and 65%. Only main injection was considered. The results are shown in Figure 2.27 and 2.28.

For $E_{A,1}$, the 5% EGR level is away from its counterparts, where the data is fluctuating around 1.69×10^4. However, the maximum variation is only 5%. For higher EGR levels the trend is much more linear and no large variations are observed for different EGR levels.

For $E_{A,2}$, an even better trend is observed. The coefficient is almost linearly correlated to SOI for each EGR level. Although the trend with respect to EGR level is not clear because of the lower values for 65% EGR case, The scattered points are generally close. The maximum variation is 6%.

2.5.6 Calibration structure

The results of individual calibration indicate that the calibration parameters are strong functions of engine speed, load and start of injection. Thus, lookup tables or functions are

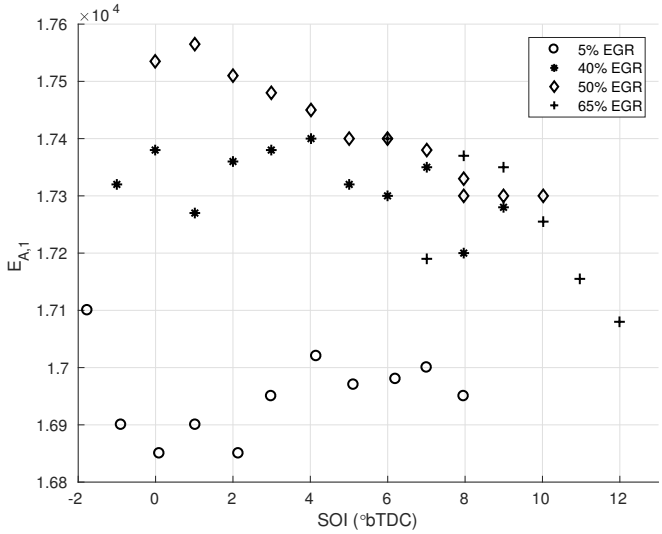

Figure 2.27: $E_{A,1}$ vs. SOI for different EGR levels at 1400 r/min with constant fuel

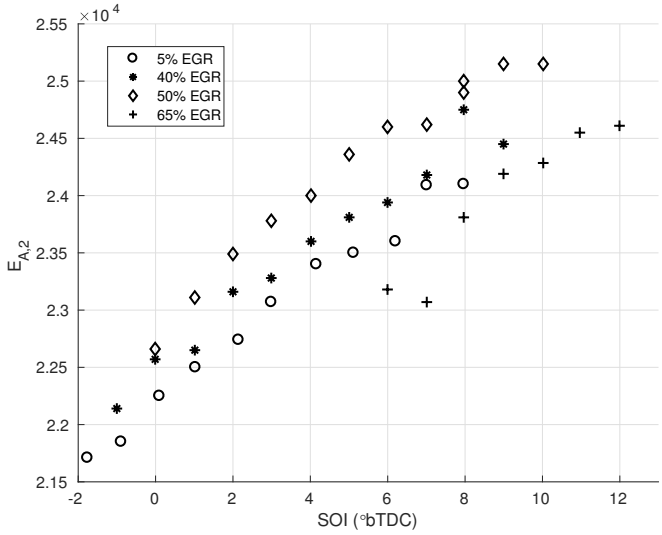

Figure 2.28: $E_{A,2}$ vs. SOI for different EGR levels at 1400 r/min with constant fuel

needed for a universal set of parameters covering the entire engine test data set. Figure 2.29 shows the calibration structure of the parameters as lookup tables or functions of engine control inputs.

The calibration structure is illustrated as follows:

- Individual calibration of the 16 key points over the engine operating map is performed,

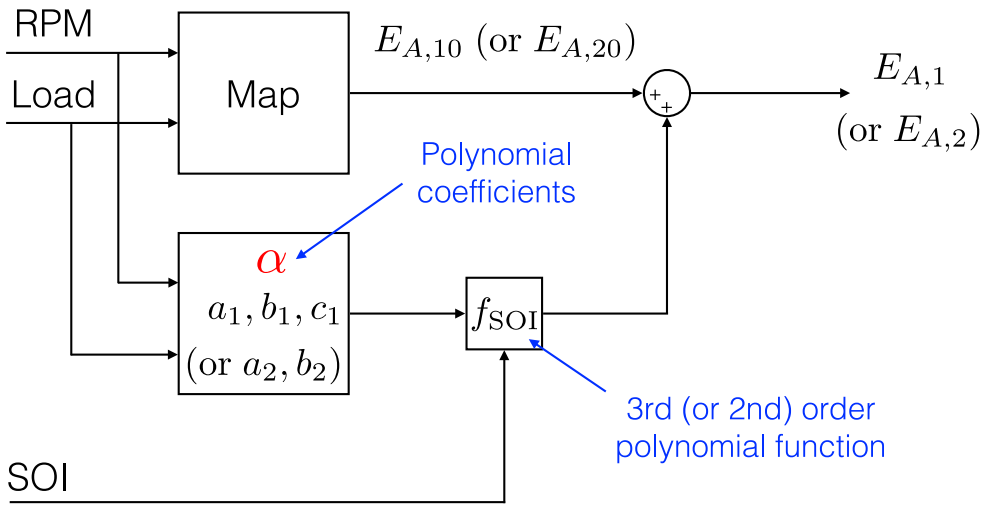

Figure 2.29: Calibration structure

which has been completed in the previous subsection.

- Lookup tables are generated from the calibration results, which are denoted as $E_{A,10}$ and $E_{A,20}$.
- The automated calibration algorithm is implemented for multi-case calibration to optimize the coefficients of the second order polynomial for SOI sweep.

The second order polynomial fit structure expressed mathematically is in the form

$$E_{A,1} = a_1 \cdot (SOI - SOI_0)^2 + b_1 \cdot (SOI - SOI_0) + E_{A,10} \tag{2.51}$$

and

$$E_{A,2} = a_2 \cdot (SOI - SOI_0)^2 + b_2 \cdot (SOI - SOI_0) + E_{A,20} \tag{2.52}$$

where SOI_0 is the injection timing of points on the engine map. a_1, b_1, a_2 and b_2 are initially lookup tables, but can be reduced to numbers if error is not significantly increased.

The third order polynomial fit structure expressed mathematically is in the form

$$E_{A,1} = a_1 \cdot (SOI - SOI_0)^3 + b_1 \cdot (SOI - SOI_0)^2 + c_1 \cdot (SOI - SOI_0) + E_{A,10} \tag{2.53}$$

and

$$E_{A,2} = a_2 \cdot (SOI - SOI_0)^3 + b_2 \cdot (SOI - SOI_0)^2 + c_2 \cdot (SOI - SOI_0) + E_{A,20} \quad (2.54)$$

where SOI_0 is the injection timing of points on the engine map. a_1, b_1, c_1, a_2, b_2, c_2 are lookup tables of engine speed and load.

2.5.7 Calibration: engine map

The engine map calibration is used to obtain $E_{A,10}$ and $E_{A,20}$. The calibration surface is generated by interpolation and extrapolation. A factor called "smoothness" can be tuned with losing accuracy as shown in Figure 2.30. For the best accuracy, the smoothness is set as 1. The calibration surface is shown in Figure 2.31.

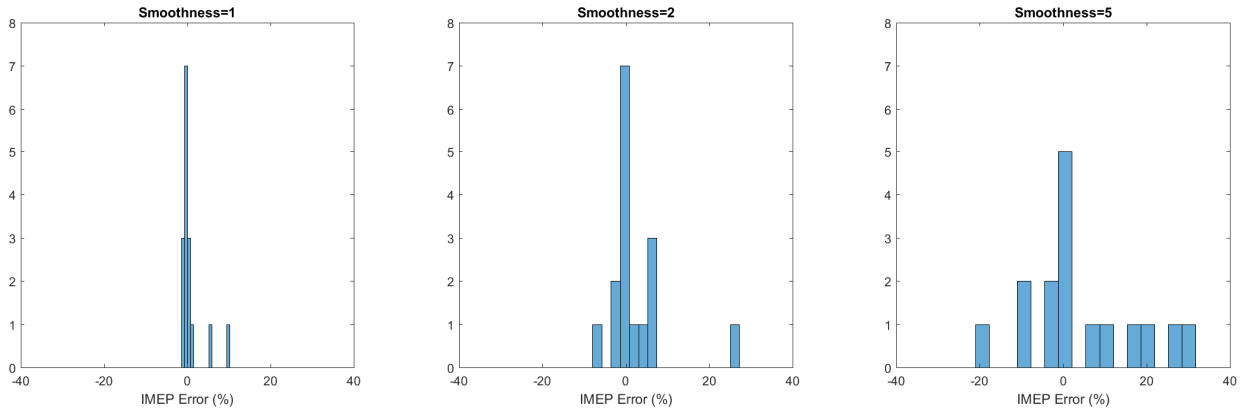

Figure 2.30: Distribution of IMEP error with various smoothness

2.5.8 Calibration: SOI sweep at constant speed and load

The estimated IMEP is compared to actual one for different calibration strategies. The smoothed lookup tables are first used and showed good agreement with test data in Figure 2.32. When the calibration structure is implemented, modeling errors are increased. A third order polynomial fit is shown to achieve fairly good match, compared to test data as shown in Figure 2.33. The error distribution is uniform. There are 8 outliers out of 37

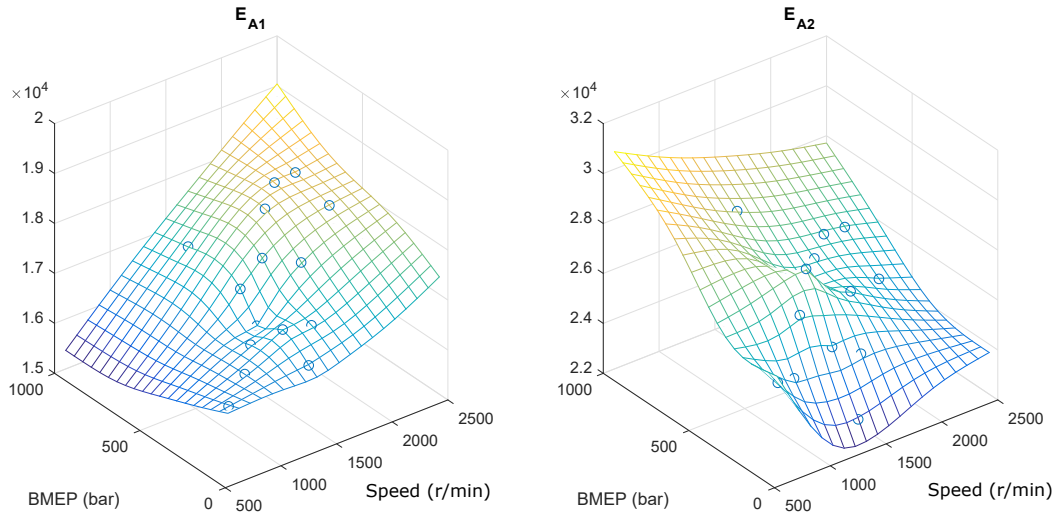

Figure 2.31: Calibration surfaces for $E_{A,1}$ and $E_{A,2}$

points in this study, which means 78% of the points are within 5% error bound. A second order polynomial structure simplified the expression of the parameters but also introduced more error as shown in Figure 2.34. The error distribution for the two structures is shown in Figure 2.35a and Figure 2.35b. The advantage in accuracy of 3rd order polynomial fit is obvious. Alternatively, a mixed order polynomial fitting has been applied, where $E_{A,1}$ is fit with a third order polynomial and $E_{A,2}$ is fit with a second order polynomial. The results, as shown in Figure 2.36, showed slightly reduced accuracy but also less computational effort.

2.5.9 Calibration: SOI sweep at constant speed and fuel injection

Figure 2.37 and Figure 2.38 show the results for SOI sweep at constant speed and fuel for smoothed lookup table with second order polynomial fit, respectively. It is shown that the fitting is less accurate compared to cases with the constant speed and load. However, the fitting captures most of the data points.

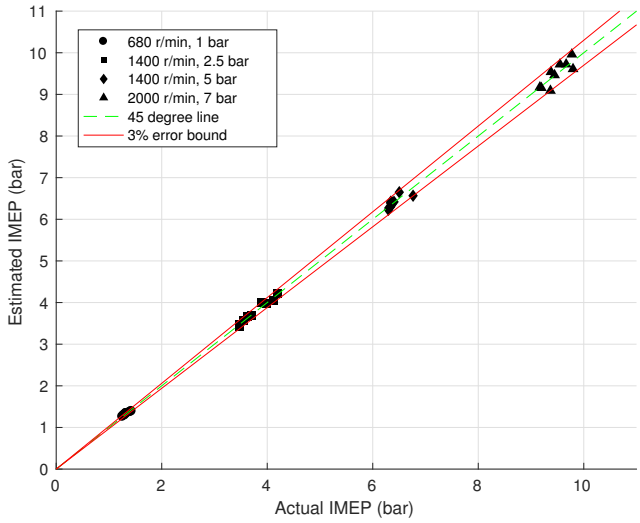

Figure 2.32: Predicted IMEP vs. actual IMEP for smoothed lookup table

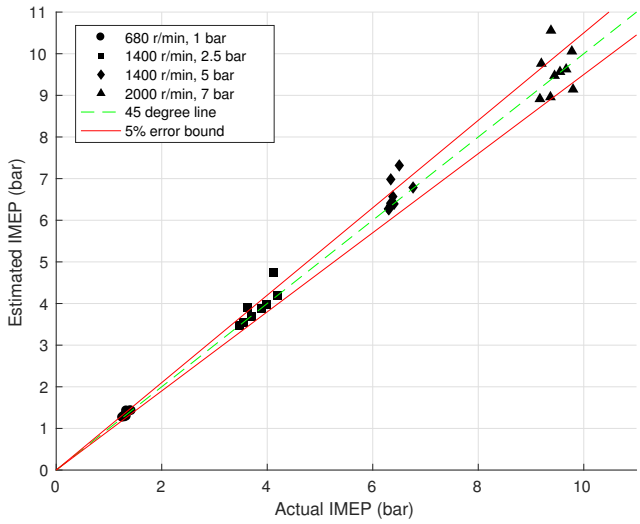

Figure 2.33: Predicted IMEP vs. actual IMEP for third order polynomial fit

2.5.10 Model validation

To validate the calibrated model, a reduced data set is used. The data are arbitrarily selected from the full set. Half of the points are used to calibrate the model and the other half are used to test the model's performance. Figure 2.39 shows the predicted IMEPs vs. actual ones for SOI sweep data. Most of the points are with the 10% bound although there are a

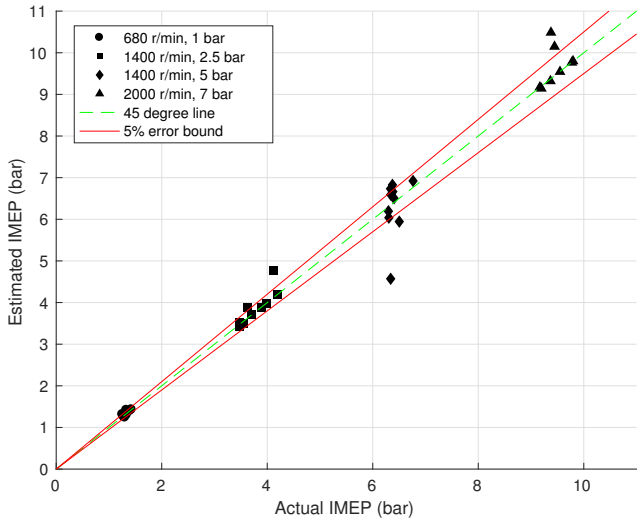

Figure 2.34: Predicted IMEP vs. actual IMEP for second order polynomial fit

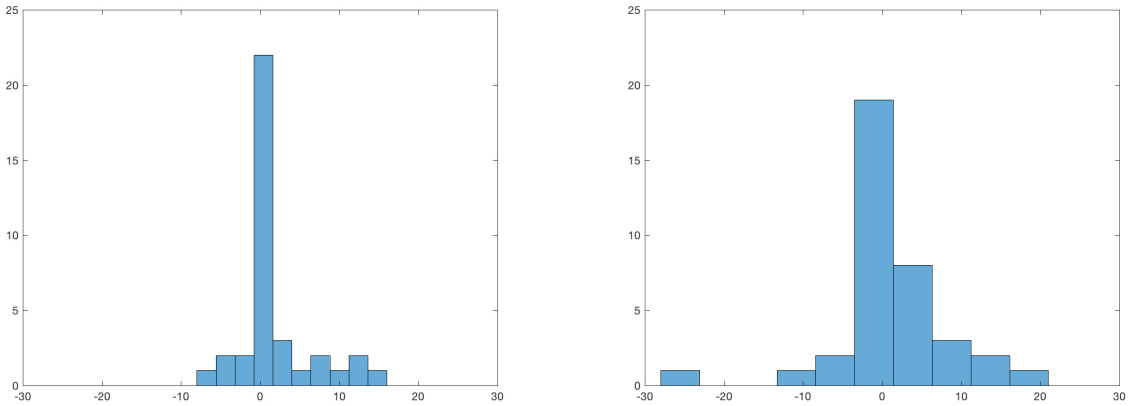

(a) Third order polynomial fit

(b) Second order polynomial fit

Figure 2.35: Error distribution

few outliers.

2.6 Conclusions

Traditional Wiebe based combustion model needs to be pre-calibrated to simulate flame propagation process and is not capable of predicting autoignition and heat release in diesel combustion when combustion parameters change. Combustion model is required to predict

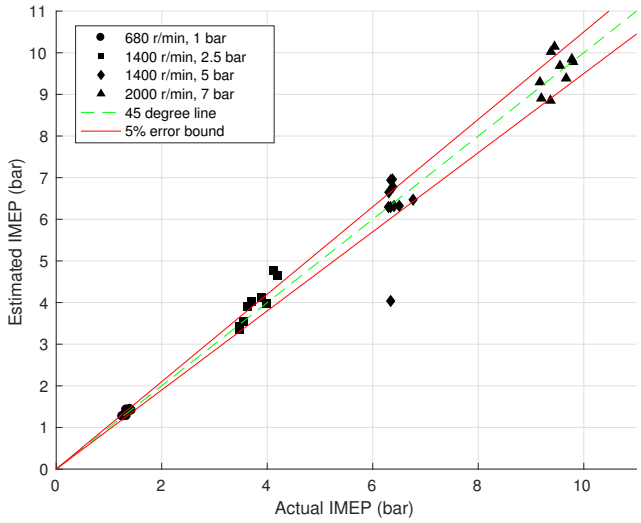

Figure 2.36: Predicted IMEP vs. actual IMEP for third order polynomial fit for $E_{A,1}$ and second order polynomial fit for $E_{A,2}$

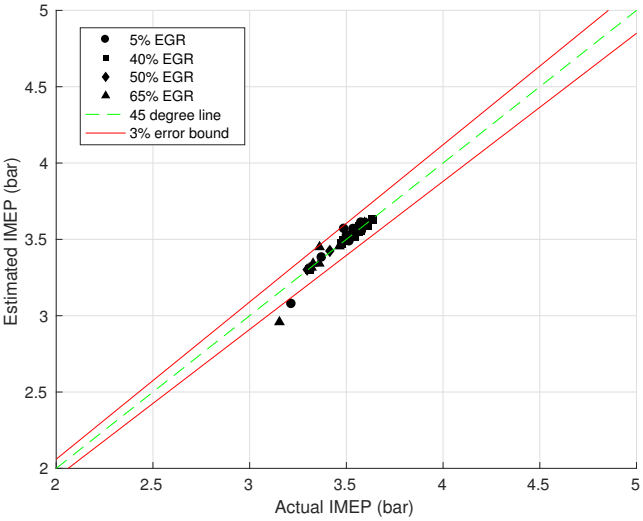

Figure 2.37: Predicted IMEP vs. actual IMEP for smoothed lookup table

the torque for diesel engines under different operating conditions, including multiple pulse fuel injections, large range of AFR, EGR variations, etc. The key in-cylinder dynamics, such as charge mixing, chemical reactions and heat transfer, need to be accounted for and to do this a detailed crank-resolved model has been selected. The reaction-based modeling

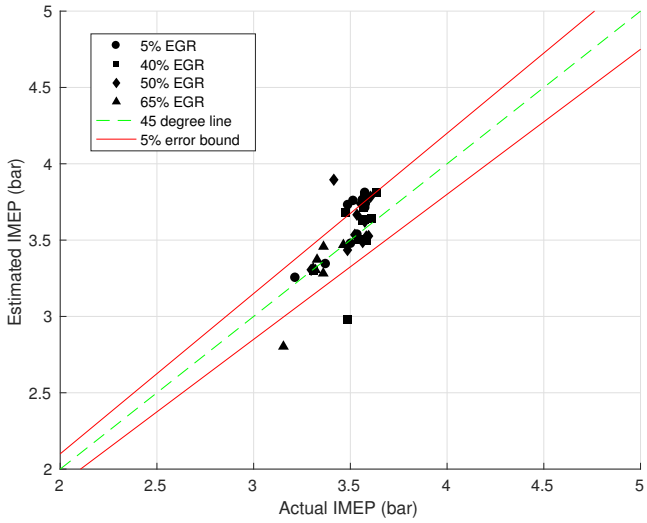

Figure 2.38: Predicted IMEP vs. actual IMEP for second order polynomial fit

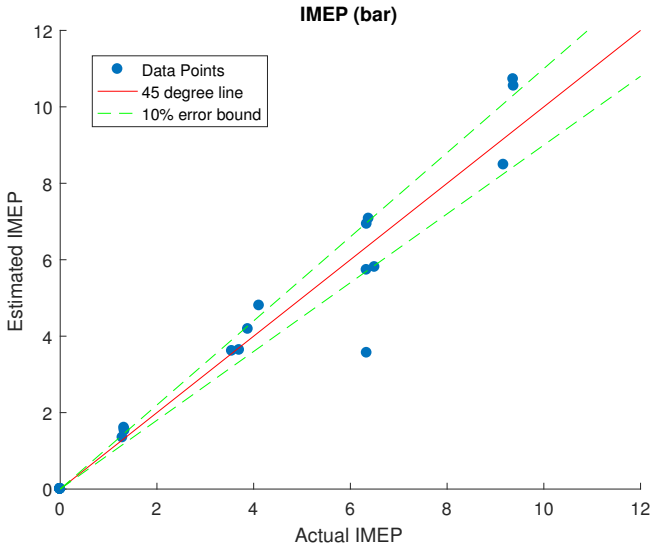

Figure 2.39: Predicted IMEP vs. actual IMEP

approach is therefore chosen because autoignition and heat release rate are predicted based on instant mixture composition and in-cylinder temperature and pressure.

In this chapter, a two-step reaction-based combustion model has been developed along with the torque model. The model is based on first law of thermodynamics expressed in species concentrations. The model has 9 state variables: $[C_{10.8}H_{18.7}]$, $[O_2]$, $[CO]$, $[CO_2]$,

[H_2O], [N_2], V, T. The initial concentrations are calculated based on mass of fuel injected, AFR, residual mass and EGR rate at IVC Each concentration is integrated independently and temperature rate is calculated based on the effect of all the concentrations. The rate of change of concentration is mainly controlled by a two-step chemical reaction, where the rate is described by the Arrhenius function. The model has been developed and simulated in MATLAB Simulink. The key findings are summarized as follows:

1. The model divides the combustion process into two stages: ignition, and first stage of energy release and second stage of energy release.

2. At stage 1, the model predicts the autoignition accurately, followed by a fast heat release process, producing major amount of CO, which is mostly accomplished by the first chemical reaction step. This process coincides with the experimental observations.

3. At stage 2, [CO] reaches the limit that triggers the second stage chemical reaction. Heat release rate is significantly lower than that in the first stage, however, it is still based on the assumption of homogeneous combustion. The rate of rising is higher and drops earlier compared to actual stratified combustion test results.

4. Unlike Wiebe-based model, for multi-injection conditions, the model is able to adapt to any injection profile automatically.

5. The mathematical nature of Arrhenius function introduces a positive feedback of temperature variation, i.e., once the reaction is initiated, temperature will grow faster and faster. The only termination is when the fuel is almost completely consumed. This characteristics allows the model to predict the ignition and early stage of combustion accurately. But it also could over predict the heat release rate in middle and late combustion stages. This could be also due to the homogeneous combustion assumption.

6. The model is able to predict incomplete combustion by calculating the species concentration at the end of combustion. The residual [$C_{10.8}H_{18.7}$] and [CO] account for the

unburned mixture. This is important for very later injection case during regeneration operation.

The model was calibrated in a comprehensive style. By sensitivity analysis, it is found that the most sensitive parameters are activation energies in both steps: $E_{A,1}$ and $E_{A,2}$. Since the two steps are independent in heat release, it is feasible to control the two stages separately by changing $E_{A,1}$ and $E_{A,2}$. Individual calibration for single point gives precise IMEP and good crank-based response. The parameters correlated well with SOI in linear or second order polynomial sense at fixed speed and load condition. The polynomial fitting is accurate for normal operating conditions but less accurate for very low and high load conditions.

CHAPTER 3

A THREE-ZONE COMBUSTION MODEL FOR DIESEL ENGINES

3.1 Introduction

To meet the demands for performance (torque and fuel economy) and to satisfy the government regulations for emissions and safety, modern diesel engines, typically operated under lean air-fuel ratio (AFR), utilize control strategies such as multiple fuel injections and exhaust gas recirculation (EGR). At low speed, a pilot injection is usually made 5 to 7 crank angle degrees before the main injection to increase the cylinder temperature so that when the main injection occurs the fuel in the environment is at a higher temperature than its autoignition point, uniform combustion. It is shown that pilot injection also helps to reduce combustion noise [21]. Under the regenerative operations of engine aftertreatment subsystems (e.g., diesel particular filter and lean NOx trap), a post injection is often used to maintain the engine exhaust AFR close to stoichiometry, and the injection timing is usually significantly retarded. These strategies make control of diesel engine systems more difficult than ever. To enable model-based control, physics-based models were developed to simulate the engine behavior in real-time. Therefore, it is required that a control-oriented engine combustion model gives accurate predictions while keeping itself computationally efficient.

Features of a combustion model include predicting burn rate, in-cylinder temperature and pressure closely related to engine performance (e.g., torque and efficiency), which makes it one of the most critical sub-models of an engine system model. Various types of combustion models have been developed that can be categorized into four groups based on their complexity: 1) zero-dimensional models; 2) quasi-dimensional models; 3) one-dimensional models; 4) three-dimensional models.

Zero-dimensional models are also referred to as single-zone models due to the assumption that the entire engine cylinder is a uniform thermodynamic control volume, which under-

goes energy and/or mass exchange with the surroundings and energy released during the combustion process is governed by first law of thermodynamics. In most single-zone models [22] and some multi-zone models [23, 24], the well-known Wiebe function [7] is used to model the fuel burn rate. The Wiebe function has advantages of low computational load and easy implementation. However, when the control variables are out of the modeled operational range, for instance, when multiple injection strategy changes, Wiebe-based combustion models are neither able to provide accurate predictions nor easy to calibrate. Moreover, a separate ignition delay model [25] is needed to predict the start of combustion, which in most cases is accomplished by the Arrhenius integral [26]. Empirical burn rate model [27] is used alternatively by including cylinder state such as temperature, pressure, fuel and oxygen concentrations, etc. The model predicts heat release rate, peak pressure and IMEP fairly well for multiple injections while keeping computational load low. However, complementary models such as fuel evaporation model, mixing model, and ignition delay model, crucial to predicting combustion timing and limiting the burn rate, are required for such type of models.

Reaction-based modeling approach [28] has been proposed and used for diesel combustion. These models utilize thermochemistry and chemical kinetics [13] to describe the interactive dynamics among in-cylinder species, which is quite different from the traditional macroscopic thermodynamics-based models. The properties of the whole cylinder gas is assumed to be the weighted sum of all the species properties, although temperature is uniform over the entire control volume. The burn rate is calculated based on the species concentrations and temperature, depending on which chemical kinetic mechanism is assumed. Ideally, the reaction-based models are able to adapt to any injection profile due to the consistent formulation of the model structure. Moreover, because concentrations and temperature are fed back to the burn rate calculation, the model has the potential to predict heat release rate under various operating conditions such as multiple injections. The model in literature [28] was tested to predict the in-cylinder pressure reasonably accurately under a wide range

of operating conditions, where it turned out that two combustion coefficients are functions of engine speed and load, even injection timing. The functions can be modeled as second order polynomials. The model is still under single-zone assumption without evaporation and mixing mechanism leading to early start of combustion, over-predicted burn rate and peak pressure, and fast burning during mixing-controlled combustion stage.

To compensate for the shortcomings of single-zone models, quasi-dimensional models (or multi-zone models) are developed mainly to model the inhomogeneity of mixture in a diesel engine cylinder. The models remain zero-dimensional but introduce interactions between different zones. There are two types of quasi-dimensional diesel combustion models depending on the formulation. Phenomenological combustion models [29, 30, 31] are extension of single-zone empirical models by expanding the fuel evaporation model into a spray model, where a number of zones with different composition and temperature but the same pressure are used and an air zone is used to account for air entrainment, leading to accurate predictions of heat release rate, pressure, and NO emissions. However, the burn rate is still calculated empirically; thus ignition delay models are required for these models. The other type of models uses chemical kinetics to calculate combustion rate, in addition to using detailed spray model [32, 33]. In these models, the inhomogeneity of composition and temperature are accounted for by formulating a number of spray parcels that interact with each other and with the surrounding air zone. There is no need for ignition delay model in this case because the chemical kinetic mechanism predicts the start of combustion automatically. Fewer calibration parameters are required for such models due to the absence of empirical functions. The model is able to predict combustion metrics such as heat release rate and in-cylinder pressure accurately over a wide range of engine operational map. However, the computational load is significantly increased. Multi-zone modeling approaches have been widely used for different combustion systems, such as HCCI [34, 35, 36] and PCCI [37] combustion, and these models have been validated with rapid compression machine tests [38, 39]. For diesel combustion, the multi-zone approach used for handling fuel evaporation (spray

models [40, 41]) and mixing-controlled combustion [42]. More related work can be found in [43] and [44].

In this chapter, a three-zone reaction-based model is developed with formulations [45] significantly different from the models discussed above. The physical delay is accounted for using fuel evaporation model, the chemical delay by a simplified chemical kinetic mechanism, and air entrainment by Fick's law of diffusion. The purpose of this work is to significantly reduce the number of zones in the multi-zone model to decrease the computational load while maintaining the critical physical significance and keeping the model prediction accurate with minimal calibration parameters. The model's capability of combustion metrics prediction has been demonstrated. The model has been calibrated with test data from a GM 6.6 L diesel engine. The improvement in both accuracy and parameter invariability compared to the single-zone reaction-based model has been shown.

3.2 Model description

This section describes the main architecture of the proposed three-zone combustion model. The structure of the model will be explained schematically, followed by mathematical derivations of the dynamics in each zone.

3.2.1 Model structure

The structure of the three-zone model is shown in Figure 3.1a. The model is divided into three zones: a fuel zone surrounded by a reaction zone that interacts with the unmixed zone. It is assumed that fuel zone only contains diesel fuel molecules, while the unmixed zone consists of fresh air and residual gas. During the simulation, liquid fuel is first injected into the cylinder to form the fuel zone. Due to the lower temperature of the injected fuel than gases in the reaction zone, the fuel is first heated as a whole until it reaches boiling point. The fraction of fuel which is at boiling point begins to vaporize and mix with the surrounding reaction zone gas. The vaporization process leads to two effects: transfer of fuel

molecules from the fuel zone to the reaction zone and heat absorption due to phase change. On the other hand, the air and residual gas in the unmixed zone flow into the reaction zone, driven by two types of forces: diffusion governed by Fick's law and bulk mass transfer as a result of the temperature difference between the two zones. The cross-sectional view of modeled cylinder physics is shown in Figure 3.1b.

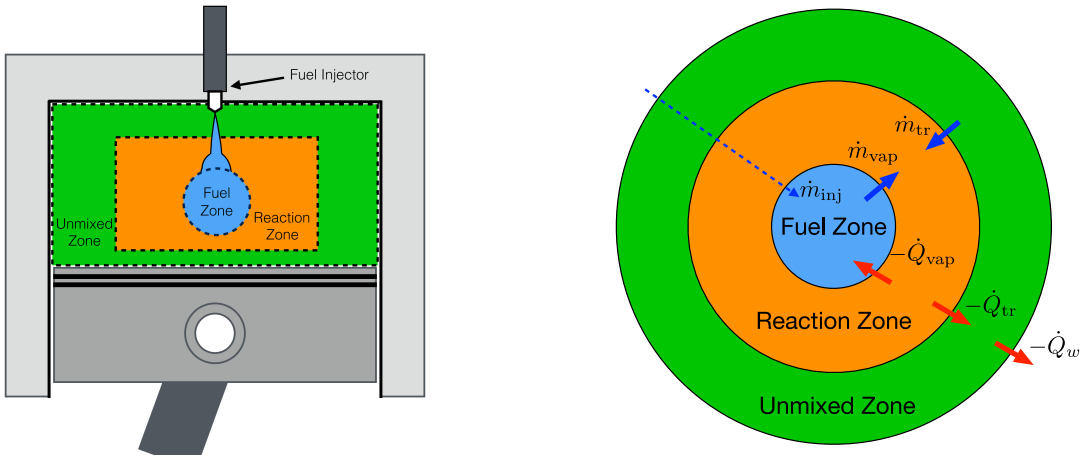

(a) Longitudinal view (b) Cross-sectional view

Figure 3.1: Three-zone model schematic

3.2.2 Volume and volume rate equations

The zero-dimensional reaction-based modeling approach is based on the assumption that the volume, where reactions take place, is predefined. Therefore, it is important to calculate the volume and volume rate for each zone before calculating mass and thermal quantities.

The instant cylinder volume V and volume rate of change $\dot{V}$ are dependent on current crank angle and the cylinder geometry. Equation 2.18 and 2.19 demonstrate the calculation of these two variables

For the fuel zone, the fuel is in liquid state, leading to the assumption that the density of fuel is constant. Therefore, the volume rate can be calculated as

$$V_f = \frac{m_f}{\rho_{\text{fuel}}} \tag{3.1}$$

where m_f is the mass in fuel zone and ρ_{fuel} is fuel density. In fact, the volume of fuel zone is only 0.01% of cylinder volume, which makes it negligible in this study.

For unmixed zone, the volume V_u is calculated by ideal gas law:

$$V_u = \frac{m_u R_u T_u}{pMW_u} \tag{3.2}$$

where m_u is the total mass of unmixed zone; R_u is the universal gas constant; T_u is unmixed zone temperature; p is the in-cylinder pressure; MW_u is the mixture molecular weight in the unmixed zone. The rate of volume change of unmixed zone $\dot{V}_u$ is calculated by taking numerical derivative of V_u with respect to time.

The volume and its rate of change in the reaction zone can be calculated based on volumes of cylinder and reaction zone:

$$V_r = V - V_u \tag{3.3}$$

and

$$\dot{V}_r = \dot{V} - \dot{V}_u \tag{3.4}$$

3.2.3 Fuel zone

The objective of formulating fuel zone is to describe the physics of fuel evaporation during and after injection events using a simplified droplet evaporation model [13], as shown in Figure 3.2. Certain assumptions are made so that the model is computationally efficient while still agrees reasonably well with experimental results:

1. The fuel is a single-component liquid.

2. Temperature is uniform and constant over the entire zone at any instant in time, and it is assumed to be equal to the temperature when the fuel is initially injected. As the fuel zone is heated by the reaction zone, the temperature will increase until it reaches the boiling point of the fuel, T_{boil}. Only when the boiling point is reached does the fuel begin to vaporize. The time duration between the start of injection and start of fuel evaporation is defined as the physical delay of ignition.

3. The heat transfer between fuel zone and reaction zone begins as soon as fuel is injected and ends when boiling point is reached.

4. The thermal-physical properties, such as thermal conductivity, density, and specific heat, are assumed to be constant for solving the equations.

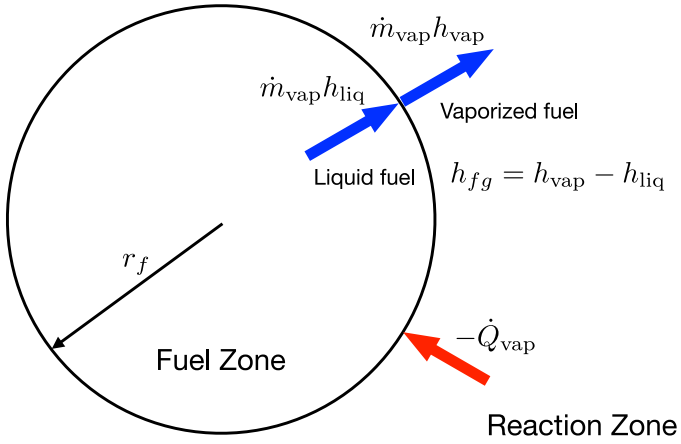

Figure 3.2: Fuel evaporation model

There are two states, the mass of fuel, m_f, and temperature, T_f, in the fuel zone:

$$\dot{m}_f = \frac{dm_f}{dt} = \dot{m}_{\text{inj}} - \dot{m}_{\text{vap}} \tag{3.5}$$

$$\dot{T}_f = \frac{-\dot{Q}_{\text{vap}} + \dot{m}_{\text{inj}}(h_{\text{inj}} - h_f) - \dot{m}_{\text{vap}} h_{fg}}{m_f c_{v,\text{fuel}}} \tag{3.6}$$

where $\dot{m}_{\text{inj}}$ is available through fuel injection profile or parameters; h_{inj} is the specific enthalpy of fuel at injection temperature; h_f is the specific enthalpy of the mass in fuel zone; h_{fg} is the specific heat for evaporation; $c_{v,\text{fuel}}$ is the constant-volume specific heat capacity of fuel; and $\dot{m}_{\text{vap}}$ is the evaporation rate of fuel that can be derived by solving the energy equation on the droplet surface:

$$\dot{Q}_{\text{vap}} = -\dot{m}_{\text{vap}} h_{fg} \tag{3.7}$$

Substituting Fourier's law for $\dot{Q}_{\text{vap}}$, the equation becomes

$$4\pi k_g r_f^2 \frac{dT}{dr} = \dot{m}_{\text{vap}} h_{fg} \tag{3.8}$$

where k_g is the conductivity and r_f is the radius of the fuel zone. It is assumed that at any time, the temperature in the reaction zone has a constant distribution gradient; thus, the gradient term can be rewritten as $2(T_r - T_f)/l_r$, where T_r is the reaction zone temperature and l_r is the thickness of the reaction zone.

The evaporation rate and heat transfer can be calculated as follows

$$\dot{m}_{\text{vap}} = \begin{cases} \frac{8\pi k_g r_f^2 (T_r - T_f)}{l_r h_{fg}} & \text{if } T_f = T_{\text{boil}} \\ 0 & \text{if } T_f < T_{\text{boil}} \end{cases} \tag{3.9}$$

$$\dot{Q}_{\text{vap}} = -\frac{8\pi k_g r_f^2 (T_r - T_f)}{l_r} \tag{3.10}$$

3.2.4 Unmixed zone

The unmixed zone contains fresh air and residual gas as a fraction of the whole cylinder gas. It is assumed that the unmixed zone is a hollow cylinder with the reaction zone inside of it. The mass transfer consists of bulk mass flow caused by temperature gradient and diffusion caused by concentration gradient:

$$\dot{m}_{\text{tr}} = \dot{m}_{\text{bulk}} + \dot{m}_{\text{diff}} \tag{3.11}$$

To physically account for bulk mass flow, a virtual interface zone (M) is assumed, as shown in Figure 3.3. The mass of Zone M is assumed to be nonzero only within each step. Temperature T_m is equal to the weighted averaged temperature of the reaction zone and unmixed zone:

$$T_m = \frac{m_r T_r + m_u T_u}{m_r + m_u} \tag{3.12}$$

where m_r and T_r are mass and temperature of reaction zone, respectively.

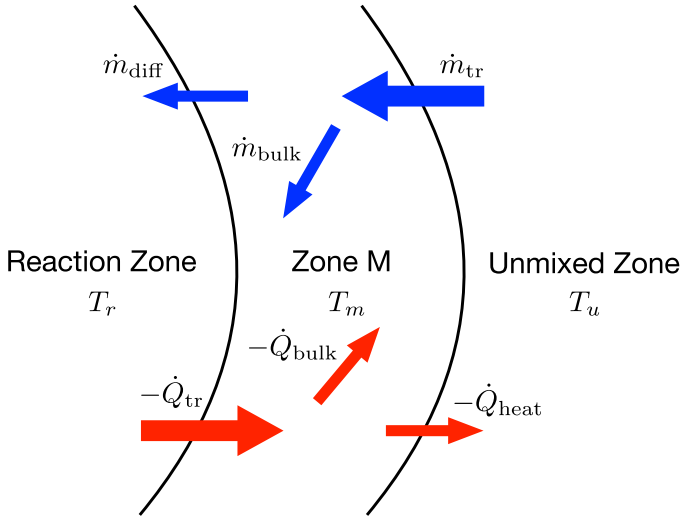

Figure 3.3: Air entrainment model

The total conductive heat transfer into reaction zone is calculated as

$$\dot{Q}_{\text{tr}} = -\frac{2k_c A_r (T_r - T_u)}{l_r} \tag{3.13}$$

where k_c is the conductivity of current interface. This heat transfer has two effects: moving the mass from unmixed zone to reaction zone and heating up the rest of unmixed zone. It can be expressed as

$$\dot{Q}_{\text{tr}} = \dot{Q}_{\text{bulk}} + \dot{Q}_{\text{heat}} \tag{3.14}$$

where

$$\dot{Q}_{\text{bulk}} = -\frac{2k_c A_r (T_r - T_m)}{l_r} \tag{3.15}$$

Since the conductive heat transfer used to drive the bulk flow is from reaction zone and only Zone M is contacted with reaction zone, the temperature difference in the calculation should be $T_r - T_m$. As a result, the heat transfer for heating the unmixed zone is resulted:

$$\dot{Q}_{\text{heat}} = \dot{Q}_{\text{tr}} - \dot{Q}_{\text{bulk}} = -\frac{2k_c A_r (T_m - T_u)}{l_r} \tag{3.16}$$

At this point, the bulk mass flow can be derived from $\dot{Q}_{\text{bulk}}$:

$$\dot{m}_{\text{bulk}} = -\frac{\dot{Q}_{\text{bulk}}}{c_m (T_r - T_u)} = \frac{2k_c A_r (T_r - T_m)}{l_r c_m (T_r - T_u)} \tag{3.17}$$

where c_m is specific heat capacity. It is apparent that when T_m approaches T_u, $\dot{m}_{\text{bulk}}$ approaches $\frac{2k_C A_r}{l_r c_m}$. And when T_m approaches T_r, $\dot{m}_{\text{bulk}}$ approaches 0, which indicates $\dot{m}_{\text{bulk}} \in \left[0, \frac{2k_C A_r}{l_r c_m}\right]$.

A simplified charge mixing model [24] is modified in this chapter to formulate the diffusive mass flow rate of unburned gas from unmixed zone to reaction one, which is dominated by turbulent diffusion. Under this assumption, Fick's law is applied:

$$\dot{m}''_{\text{diff}} = -\rho_u \mathcal{D}_t \frac{dY}{dr} \tag{3.18}$$

where $\dot{m}''_{\text{diff}}$ is the turbulent mass flux of the unmixed gas; ρ_u is the density of the unburned gas; $\mathcal{D}_t$ is the turbulent diffusivity; and $\frac{dY}{dr}$ is the mass fraction distribution in the reaction zone in the direction of interest. In this case, it is calculated as the mass fraction difference between reaction zone and unmixed zone:

$$\frac{dY}{dr} \approx \frac{2(Y_r - Y_u)}{l_r} \tag{3.19}$$

where Y_r and Y_u are the mass fraction in reaction zone and unmixed zone, respectively. The relationship between turbulent diffusivity and turbulent viscosity gives the following equation that can be used to calculate $\mathcal{D}_t$:

$$Sc_t = \frac{\nu_t}{\mathcal{D}_t} \tag{3.20}$$

where Sc_t is the turbulent Schmidt number. Note that ν_t is the turbulent viscosity that can be calculated by

$$\nu_t = k_d \bar{v} l_r \tag{3.21}$$

where $\bar{v}$ is the averaged velocity of the gas flow in the reaction zone that can be approximated by the mean piston speed; l_r is the thickness of the reaction zone (the same as in the previous calculation); and k_d is the calibration parameter. The mass transfer rate from unmixed zone to reaction zone can be expressed as

$$\dot{m}_{\text{diff}} = \frac{2k_d \rho_u \bar{v} A_r (Y_u - Y_r)}{Sc_t} \tag{3.22}$$

where A_r is the contact area of the surface between unmixed zone and reaction zone, which is equal to the surface area of the reaction zone.

The reaction-based model of unmixed zone is based upon the first law thermodynamic analysis of an open system. Six states are included in this zone and they are unmixed zone volume (V_u), unmixed zone temperature (T_u), the concentrations of oxygen ($[O_2]$), carbon dioxide ($[CO_2]$), water ($[H_2O]$), and nitrogen ($[N_2]$). In a chemical kinetic system, the molecular concentration of species i is defined as

$$[X_{u,i}] = \frac{N_{u,i}}{V_u} \tag{3.23}$$

where $N_{u,i} = \frac{m_{u,i}}{MW_{u,i}}$ is the number of moles of species i; $m_{u,i}$ is the mass; and $MW_{u,i}$ is the molecular weight.

The rate of change of molar concentration of species i is defined as

$$[\dot{X}_{u,i}] = \frac{\dot{N}_{u,i}}{V_u} - \frac{\dot{V}_u N_{u,i}}{V_u^2} = w_{\mathrm{tr},i} - \frac{\dot{V}_u}{V_u}[X_{u,i}] \tag{3.24}$$

where $w_{\mathrm{tr},i}$ is the gas mixing rate, which can be calculated as

$$w_{\mathrm{tr},i} = -\frac{\dot{m}_{\mathrm{tr}}}{V_u MW_u} \tag{3.25}$$

From the first law of thermodynamics, we have

$$\frac{dU_u}{dt} = \dot{Q}_u - \dot{W}_u - \dot{m}_{\mathrm{tr}} h_u \tag{3.26}$$

where U_u is the internal energy of unmixed zone; $\dot{Q}_u$ is the net heat transfer rate into the system; $\dot{W}_u$ is the net rate of work done by the system; $\dot{m}_{\mathrm{tr}} h_u$ is the energy change due to mass flow; and h_u is the specific enthalpy of unmixed gases.

The rate of work done is defined as

$$\dot{W}_u = p\dot{V}_u \tag{3.27}$$

The relation between internal energy U_u and enthalpy H is

$$H_u = U_u + pV_u \tag{3.28}$$

Then by re-arranging and differentiating with respect to time the left hand side of (3.26) becomes

$$\frac{dU_u}{dt} = \frac{d(H_u - pV_u)}{dt} = \frac{dH_u}{dt} - \dot{p}V_u - p\dot{V}_u \tag{3.29}$$

By substitution, (3.26) can be re-arranged as

$$\frac{dH_u}{dt} = \dot{Q}_u + \dot{p}V_u - \dot{m}_{\mathrm{tr}}h_u \tag{3.30}$$

The extensive property H_u can be expressed as a sum of weighted molar enthalpies of all species

$$H_u = \sum N_i\bar{h}_i = V_u \sum [X_i]\bar{h}_i \tag{3.31}$$

Thus, LHS of (3.30) becomes

$$\mathrm{LHS} = \dot{V}_u \sum [X_i]\bar{h}_i + V_u \sum [\dot{X}_i]\bar{h}_i + V_u \sum [X_i]\dot{\bar{h}}_i \tag{3.32}$$

where $\dot{\bar{h}}_i = \bar{c}_{p,i}\dot{T}_u$. Note that $\bar{c}_{p,i}$ is the constant-pressure molar heat of species i. The state equations of ideal gas in terms of concentrations are given as

$$p = \sum [X_i]R_uT_u \tag{3.33}$$

and

$$\dot{p} = R_uT_u \sum [\dot{X}_i] + R_u\dot{T}_u \sum [X_i] \tag{3.34}$$

By substitution, the right hand side (RHS) of (3.30) becomes (3.35).

$$\mathrm{RHS} = \dot{Q}_u + R_uT_uV_u \sum [\dot{X}_i] + R_u\dot{T}_uV_u \sum [X_i] + \dot{m}_{\mathrm{tr}}h_u \tag{3.35}$$

Equating (3.32) and (3.35) and re-arranging the equation give the formula for the temperature rate in (3.36).

$$\dot{T}_u = \frac{\dot{Q}_w - \dot{Q}_{\mathrm{heat}} + R_uT_uV_u \sum [\dot{X}_{u,i}] - V_u \sum [\dot{X}_{u,i}]\bar{h}_i - \dot{V}_u \sum [X_{u,i}]\bar{h}_i - \dot{m}_{\mathrm{tr}}h_u}{V_u \sum [X_{u,i}]\left(\bar{c}_{p,i} - R_u\right)} \tag{3.36}$$

Heat transfer term $\dot{Q}_u$ consists of heat transfer from reaction zone and heat loss to cylinder wall:

$$\dot{Q}_u = \dot{Q}_w - \dot{Q}_{\mathrm{heat}} \tag{3.37}$$

The heat loss rate to cylinder wall $\dot{Q}_w$ can be expressed as

$$\dot{Q}_w = -A_c h_c (T_u - T_w) \tag{3.38}$$

where A_c is the effective contact area between gas and cylinder wall; h_c is the heat transfer coefficient; and T_w is the cylinder wall temperature. The heat transfer coefficient is calculated by Woschni's correlation [46]

$$h_c = \alpha B^{-0.2} p^{0.8} T_u^{-0.55} (2.28 S_p)^{0.8} \tag{3.39}$$

where S_p is the mean piston speed and α is constant.

3.2.5 Reaction zone

The formulation of reaction zone is similar to that of unmixed zone, with gas-phase fuel and mixed gas flowing into the reaction zone and chemical reaction mechanism integrated. There are eight states included in this zone and they are reaction zone volume (V_r), reaction zone temperature (T_r), concentrations of diesel fuel ($[C_{10.8}H_{18.7}]$), oxygen ($[O_2]$), carbon dioxide ($[CO_2]$), water ($[H_2O]$), nitrogen ($[N_2]$), and carbon monoxide ($[CO]$).

The rate of change of molar concentration of species i can be calculated as

$$[\dot{X}_{r,i}] = w_i - \frac{\dot{V}_r}{V_r}[X_{r,i}] \tag{3.40}$$

where w_i is the concentration production that can be further separated into two parts:

$$w_i = w_{\text{rxn},i} + w_{\text{flow},i} \tag{3.41}$$

where $w_{\text{rxn},i}$ is the concentration production due to chemical reactions and it is calculated by the chemical kinetic mechanism, and $w_{\text{flow},i}$ is the concentration change due to mass flow into and out of the control volume. In the reaction zone, $w_{\text{flow},i}$ consists of fuel evaporation rate and gas mixing rate, i.e.

$$w_{\text{flow},i} = w_{\text{vap},i} + w_{\text{tr},i} = \frac{1}{V_r}\left(\frac{\dot{m}_{\text{vap},i}}{MW_{f,i}} + \frac{\dot{m}_{\text{tr},i}}{MW_{u,i}}\right) \tag{3.42}$$

where $MW_{f,i}$ and $MW_{u,i}$ are molecular weights of each species in fuel zone and unmixed zone, respectively.

The formula for temperature rate is shown in (3.43).

$$\begin{aligned}\dot{T}_r =& \frac{\dot{Q}_{\text{vap}} + \dot{Q}_{\text{tr}} + R_u T_r V_r \sum [\dot{X}_{r,i}] - V_r \sum [\dot{X}_{r,i}] \bar{h}_i - \dot{V}_r \sum [X_{r,i}] \bar{h}_i}{V_r \sum [X_{r,i}] \left(\bar{c}_{p,i} - R_u\right)} \\ &+ \frac{\dot{m}_{\text{vap}} h_f + \dot{m}_{\text{bulk}} h_r + \dot{m}_{\text{diff}} h_u}{V_r \sum [X_{r,i}] \left(\bar{c}_{p,i} - R_u\right)}\end{aligned} \tag{3.43}$$

where h_r is the specific enthalpy of the mass in reaction zone.

The two-step chemical reaction [13] of $C_{10.8}H_{18.7}$ oxidation can be expressed as

$$C_{10.8}H_{18.7} + 10.075\, O_2 \longrightarrow 10.8\, CO + 9.35\, H_2O \tag{3.44a}$$

$$CO + 0.5\, O_2 \longleftrightarrow CO_2 \tag{3.44b}$$

The reaction rates for $C_{10.8}H_{18.7}$ and CO oxidation are given by Arrhenius functions

$$w_1 = - A_1 \exp\left(-\frac{E_{A,1}}{R_u T}\right) [C_{10.8}H_{18.7}]^{m_1} [O_2]^{n1} \tag{3.45a}$$

$$\begin{aligned}w_2 =& - A_2 \exp\left(-\frac{E_{A,2}}{R_u T}\right) [CO]^{m_2} [O_2]^{n_2} [H_2O]^{k1} \\ &+ A_3 \exp\left(-\frac{E_{A,3}}{R_u T}\right) [CO_2]^{k2}\end{aligned} \tag{3.45b}$$

where A_1, A_2, A_3, $E_{A,1}$, $E_{A,2}$, $E_{A,3}$, m_1, m_2, n_1, n_2, k_1 and k_2 are constants.

By inspecting (3.44a) and (3.44b), the rest of the reaction rates are as follows

$$w_{O_2} = 10.075 w_1 + 0.5 w_2 \tag{3.46a}$$

$$w_{CO_2} = -w_2 \tag{3.46b}$$

$$w_{H_2O} = -9.35 w_1 \tag{3.46c}$$

$$w_{CO} = -10.8 w_1 + w_2 \tag{3.46d}$$

Note that the second step is a reversible reaction, where the reverse reaction decomposes CO_2 molecules into CO and O_2.

3.2.6 Cylinder properties

With the calculation of mixture properties of each zone, the averaged properties over the entire cylinder can be obtained. In-cylinder temperature is defined as the mass-based averaged temperature for all three zones:

$$T = \frac{m_f T_f + m_r T_r + m_u T_u}{m_f + m_r + m_u} \tag{3.47}$$

and in-cylinder pressure is calculated by ideal gas law:

$$p = \frac{(m_f + m_r + m_u) R_u T}{V M W_{\text{mix}}} \tag{3.48}$$

where MW_{mix} is the molecular weight of the mixture over the whole cylinder.

3.3 Model Validation

3.3.1 Test data

The test data used for model validation are from the same GM 6.6 L, 8 cylinder Duramax engine. The specifications of the engine are already summarized and can be found in Table 2.9. The engine was tested at steady-state under various speed and load conditions. At each operating condition, different start of injection (SOI) timings and EGR rates are used. Brake mean effective pressure (BMEP) in bar is the measure of load. The recorded test data include in-cylinder pressure traces and engine control inputs, along with post-processed heat release rate traces, air and EGR variables, pressure metrics such as IMEP and net mean effective pressure (NMEP) variables. The available test data are summarized in Table 3.1 as follows.

SOI of main injection sweeps at fixed speed and load conditions with pilot injection:

1) Four speed-load pairs: 680 r/min, 1 bar; 1400 r/min, 2.5 bar; 1400 r/min, 5 bar; and 2000 r/min, 7 bar.

2) An extra post injection at 2000 r/min.

Table 3.1: Summary of test data

Operating points		BMEP bar	q_{inj} mm^3	SOI_{main} °bTDC	EGR %
680 r/min × 12	Max	1.01	10.6	25	61.9
	Min	0.99	8.9	-10	60.8
1400 r/min × 11	Max	2.52	18.3	25	55.5
	Min	2.49	16.4	-5	53.7
1400 r/min × 11	Max	5.02	31.3	25	51.4
	Min	4.98	27.6	-5	48.0
2000 r/min × 10	Max	7.09	56.2	20	40.3
	Min	6.90	45.8	-7	38.5

3) Fixed EGR rate for each speed-load pair.

In each of the four groups, half of the data points are randomly selected for model calibration. The other half are used for model validation. To be more specific, 6 points from 680 r/min, 10 points from 1400 r/min and 5 points from 2000 r/min have been randomly selected for calibration; and the remaining 23 data points are used to test the model performance.

3.3.2 Combustion characteristics

The accuracy of pressure prediction is of highest priority. Thus, a MATLAB function based on nonlinear Least-Squares algorithm [20] is used to minimize the resulting pressure error. The function solves nonlinear least-squares curve fitting problems of the form

$$\min_{\boldsymbol{x}} ||\boldsymbol{f}(\boldsymbol{x})||_2^2 = \min_{\boldsymbol{x}} \left[f_1(\boldsymbol{x})^2 + \ldots + f_n(\boldsymbol{x})^2 \right] \tag{3.49}$$

where the cost function $\boldsymbol{f}(\boldsymbol{x})$ in this study is in the following form

$$\boldsymbol{f}(\boldsymbol{x}) = \boldsymbol{p} - \boldsymbol{p}_{\text{exp}} \tag{3.50}$$

Note that $\boldsymbol{p}_{\text{exp}}$ is a crank-based vector from experimental data and $\boldsymbol{x}$ is a vector containing the calibration parameters:

$$\boldsymbol{x} = \begin{bmatrix} k_g & k_c & k_d \end{bmatrix}^T \tag{3.51}$$

Table 3.2: Optimized model parameters

k_g	k_c	k_d
8.3×10^3	1.1×10^4	0.12

The parameter values for optimal performance are shown in Table 3.2.

The modeled pressure traces are first compared with test data for different speed and load conditions under the same main injection timing; see Figure 3.4. Three operating conditions are investigated: 680 r/min, 1 bar; 1400 r/min, 5 bar; 2000 r/min, 7 bar. The main injection timing is fixed at 20° before top dead center (TDC). Under this advanced injection timing condition, the model predictions are in good agreement with the measured values. The start of combustion has been accurately predicted due to the fuel evaporation model. The peak pressure prediction is fairly good, except for a slight mismatch with 2% relative error. This error, which is a result of the premixed combustion stage, could be attributed to the assumption of the two-step mechanism, which is an over-simplified model of the combustion chemistry. The model predicts in-cylinder pressure accurately under different operating conditions without re-calibrating model parameters. This demonstrates the advantages of the physics-based model compared to calibration-based models.

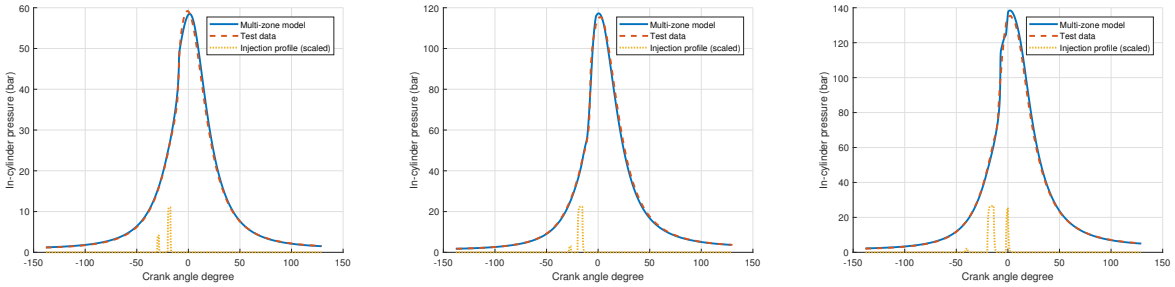

(a) 680 r/min, BMEP=1 bar (b) 1400 r/min, BMEP=5 bar (c) 2000 r/min, BMEP=7 bar

Figure 3.4: Pressure traces at different speed-load conditions with the same main injection timing at 20° bTDC

The second comparison is made under the same operational conditions except for changing the main injection timing being to 6° before TDC; see Figure 3.5. The overall pressure

prediction is still accurate, although error increases near the peak pressure location at 2000 r/min. As discussed above, the two-step assumption results in modeling error during the premixed combustion stage and in this case it is near TDC. On the other hand, the error in fuel injection rate also increases the deviation during pressure rise.

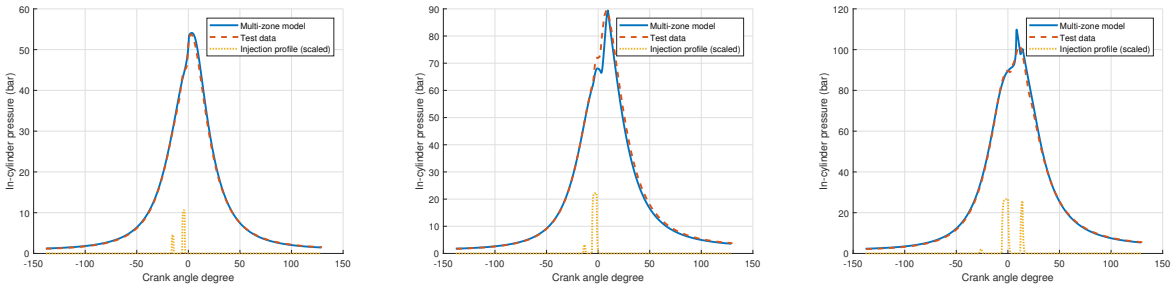

(a) 680 r/min, BMEP=1 bar (b) 1400 r/min, BMEP=5 bar (c) 2000 r/min, BMEP=7 bar

Figure 3.5: Pressure traces under different speed and load conditions with the same main injection timing at 6° bTDC

Another comparison is performed for the same operating conditions but with a retarded injection timing at 5° after TDC; see Figure 3.6. While maintaining the calibration parameters unchanged, the model predictions are still within the acceptable range. At 680 r/min, there is a larger error at the first peak, which could be due to the simplification of the fuel evaporation model. Since the fuel zone is assumed to be one spherical volume, the contact area is calculated based on the sphere radius, which could be different than the actual contact area for heat transfer. Thus, temperature estimation of the fuel zone might not be perfect, which would lead to inaccurate ignition delay for some extreme cases. At 1400 r/min and 2000 r/min, the error remains but becomes smaller and the model captures the trends fairly well. Note that for different operational conditions, the EGR rate is different, which is not explicitly included in the model. This factor could also account for the mismatch. With the results shown in the above figures, it can be concluded that the model is capable of predicting in-cylinder pressure under different speed, load, and injection timing.

The last comparison is mainly between the three-zone and single-zone models. The operating conditions are restricted to 1400 r/min and 2.5 bar with retarded injection timings.

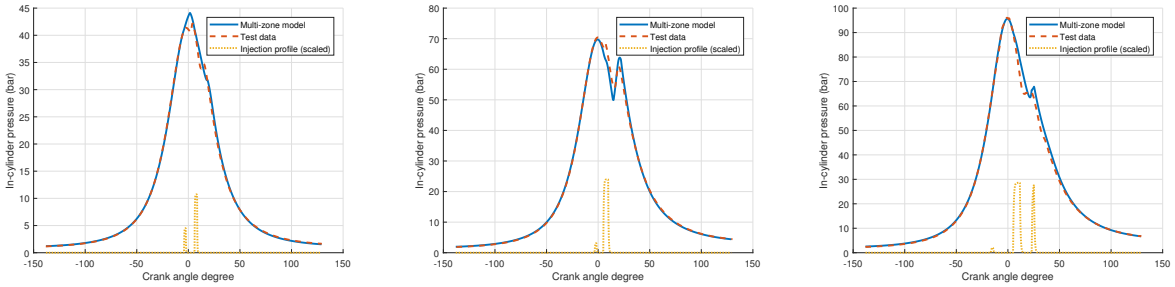

(a) 680 r/min, BMEP=1 bar (b) 1400 r/min, BMEP=5 bar (c) 2000 r/min, BMEP=7 bar

Figure 3.6: Pressure traces at different speed-load conditions with the same main injection timing at 5° aTDC

However, similar results are obtained under other conditions. As shown in Figure 3.7, while the three-zone model predicts the pressure traces with acceptable error, single-zone model predicts a much earlier start of combustion, which leads to an over-predicted peak pressure. This is due to the lack of physical delay in the single-zone model. The fuel is assumed to be ready for combustion as soon as it enters the cylinder. However, in reality, it takes time for the fuel to be prepared for combustion, which is well explained in the three-zone model.

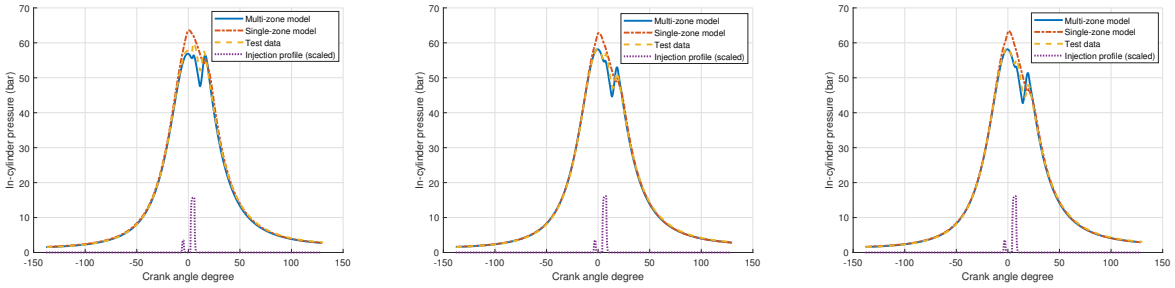

(a) SOI_{main}=2° aTDC (b) SOI_{main}=4° aTDC (c) SOI_{main}=5° aTDC

Figure 3.7: Pressure traces at 1400 r/min, BMEP=2.5 bar, with different main injection timings

The under-estimated physical delay can be further observed in heat release rate traces in Figure 3.8. The single-zone model predicts the start of combustion near the start of injection, while the actual start of combustion is around 5 degrees after injection. The three-zone model successfully matches the test results.

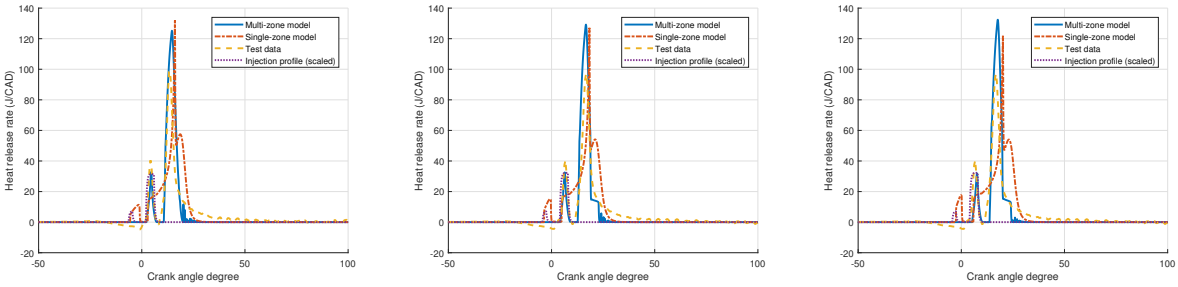

(a) SOI_{main}=2° aTDC (b) SOI_{main}=4° aTDC (c) SOI_{main}=5° aTDC

Figure 3.8: Heat release rate traces at 1400 r/min, BMEP=2.5 bar, with different main injection timings

The corresponding numerical evaluation of the modeling error of both single-zone and three-zone model is shown in Table 3.3. The modeling error in pressure is calculated as the scaled root mean square of relative pressure error from intake valve closing (IVC) at 138° bTDC to exhaust valve opening (EVO) at 129° aTDC:

$$\text{error} = \sqrt{\frac{1}{N}\sum_{i=1}^{N}\left(\frac{p(i)_{\text{model}} - p(i)_{\text{exp}}}{p(i)_{\text{exp}}}\right)^2} \times 100 \tag{3.52}$$

where $p(i)_{\text{model}}$ is the model predicted pressure; $p(i)_{\text{exp}}$ is the measured pressure; i is the index of the sampling points within the investigated range of crank angle degrees; N is the total number of sampling points.

Table 3.3: Modeling error in in-cylinder pressure (%)

SOI	Single-zone model	Three-zone model
2° aTDC	6.3860	3.8778
4° aTDC	5.9162	3.1189
5° aTDC	5.8746	3.0215

3.3.3 Parameter variability

As the three-zone model outperforms the single-zone model in predicting the combustion characteristics, it is worth noting that the three-zone model is also preferred when the models

are to be calibrated. To obtain the previous results, the single-zone model was calibrated case-by-case [47], which indicates that the model is essentially a calibration-based model with several lookup tables. Although polynomial fitting approach was applied to eliminate part of the required calibration effort, the single-zone model still needs 5-6 parameters to be calibrated with comprehensive test data.

On the other hand, the three-zone model is demonstrated to be table-free with a fixed calibration. The resulting IMEP is shown in Figure 3.9. All the data points are within the 10% error bound, and this is the results with fixed model calibration parameters. Comparing to single-zone model, which needs to change the parameters whenever the operating condition changes, the three-zone model, once calibrated, is sufficient to keep all parameters constant.

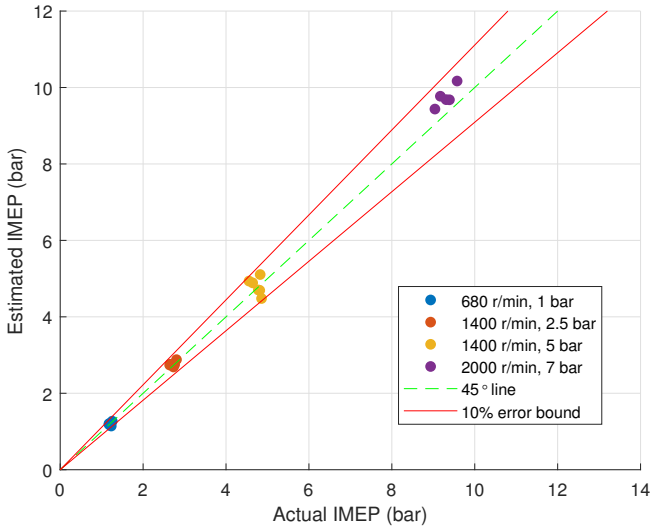

Figure 3.9: Predicted IMEP vs actual IMEP for different operating conditions

3.4 Conclusions

The three-zone reaction-based modeling approach for diesel combustion is shown in this chapter. The developed model is based on the single-zone reaction-based model, with addition of fuel evaporation model and air entrainment model. The model parameters are

calibrated using part of the test data from a GM 8-cylinder, turbocharged diesel engine. The other part of the test data over a wide range of operating conditions are then used for model validation. Comparisons between model predictions and measured data show good agreement under different speed, load and injection timing. The model successfully predicts in-cylinder pressure, heat release rate and IMEP without re-calibrating model parameters. The three-zone model outperforms single-zone one for both accuracy and parameter invariability. The current model can be used as a foundation to generate simplified control-oriented linear models or nonlinear models for model-based control design.

CHAPTER 4

MODELING AND CONTROL OF AN EBOOST SYSTEM

4.1 Introduction

With increasingly stringent regulations on engine emissions and consumer requirements for performance, modern turbocharged diesel engines are normally equipped with devices such as variable geometry turbocharger (VGT) [48, 49] and exhaust gas recirculation (EGR) [50]. Diesel engines with VGT and EGR not only gain additional power from the increased injected mass of fuel due to boosted intake air mass but also reduce NOx and soot emissions due to EGR [51]. The CO_2 emission reduction can be achieved in terms of engine down-sizing. Turbocharged engines have advantages compared to supercharged engines in boost control, altitude performance, durability, packaging and noise [52]. However, the well-known "turbo lag" is the most significant disadvantage of turbochargers (TC). Since the turbo lag is usually perceptible as slow torque response during transient operations, it directly impacts the drivability and limits engine transient performance. Coordinated VGT-EGR control is able to mitigate the turbo-lag issue [53, 54, 55, 56], but the benefit (improved performance) and cost (increased complexity) are significantly dependent on the control strategy.

Among all the techniques to eliminate turbo lag, such as transmission down-shifting, EGR reduction, smoke limit relaxing, etc., one of the most promising approaches is to add additional energy (so-called "assist energy") to the air charge system. Depending on the type of assist energy applied, there are hydraulically assisted and electrically assisted systems that have been widely studied to improve the turbocharger performance. A conventional hydraulically assisted system [57, 58] consists of a high-pressure oil pump driven from the engine crankshaft and a hydraulic turbine which is driven by the high-velocity oil jet from a simple nozzle. The more recently developed system, so-called "regenerative hydraulically assisted turbocharger (RHAT)", includes a hydraulic pump into the original system, which

has introduced additional freedom of control and the recovery ability that further improves the performance and efficiency. The related studies can be found in [59, 60, 61, 62]. Electrically assisted systems, on the other hand, comprise an electric motor that directly drives the turbocharger shaft (electrically assisted turbocharger or eTurbo) or a separate compressor (electrically assisted boosting system or eBoost). The main advantage of the hydraulically assisted turbocharger, compared to the electrical turbocharger, is its higher power density. Currently, most of the electrically assisted driving motors have the power output in the range of 1.5 - 10 kilowatts. The desired power to assisted the acceleration of large turbochargers could be over 10 kilowatts, although applications of 48 volts electric motors on assisted boosting has been validated, which could eliminate this shortcoming. The RHAT system also works better for energy recovery. When the excessive exhaust energy is available to be harvested, it is usually within the range of 15 - 40 kilowatts, where the turbocharger is operating at high speed with high kinetic energy. The current production electric motor does not provide energy recovery capability without a significant increase in inertia and mechanical stress when operating at high speed. Although RHAT out-performs eTurbo due to lower inertia, less cost, smaller packaging space and potentially better durability, it has certain challenges such as improving its low efficiency, designing fast-response hydraulic control valves and actuation systems with high-flow capacity with low losses, reducing parasitic and windage losses, managing energy storage in a hydraulic tank, and optimizing hydraulic turbine and turbo-pump that is able to deliver high efficiency over a wide operational range [61]. The studies on eTurbo and the corresponding controls can be found in [63, 64, 65, 66, 67, 68, 69].

There have been extensive numerical studies on performance of eTurbo [68, 70] and eBoost [71, 72]. In [73] a physics-based engine and vehicle model, consisting of a crank-angle-resolved cylinder model and a mean-value (0-D) air path model, has been used to study the improvement in engine performance with different assisted turbocharging topologies. Cases studied include steady-state and tip-in operations and different driving cycles. It is shown in the simulation results that both eTurbo and eBoost are able to improve steady-state and

transient engine performance. In addition, eBoost has provided higher low-speed torque output and faster transient response for transient operations starting at low engine speed, since the boost pressure build-up is not limited by the surge line, while eTurbo possesses the potential to increase high-speed torque output for a limited period of time. The improvement in performance by different boost-assist options, such as pre-compressor assistance, intake assistance, and exhaust assistance, have been investigated with 1-D simulations [74]. It is concluded that the pre-compressor option gives the best performance by a considerable margin as it avoids the compressor surge limit. A component-based model has been developed to simulate engine air path dynamics in 0-D with the flexibility to implement different assisting configurations and controls [75]. A 1-D simulation study of eTurbo and eBoost on a gasoline engine and a diesel engine has shown that downstream configuration of eBoost can significantly improve system efficiency at steady-state, compared to the upstream eBoost configuration, due to the surge limit of main compressor [76]. It is also concluded that eTurbo is not as ideal as eBoost because of the surge limit. An overview of the electrically assisted devices can be found in [77]. An integrated framework on testing and control of the eTurbo system has been developed in [78].

There is little existing literature in the area of the modeling and control of eBoost on diesel engines in detail. The physics-based air-path model developed in [75] provides the framework for a more comprehensive study of the control problems for eBoost systems. It is pointed out in [79] that by increasing the system voltage from 12 to 48 volts, engine steady-state fuel economy and transient response can be further improved. A dynamic pressure ratio allocation method is used to separate the control reference to each actuator, considering the relatively slow dynamics of turbocharger and fast response of eBoost [80]. The control design was validated in a test vehicle equipped with a downsized turbocharged spark-ignition engine. A distributed model predictive controller has been designed for an electrically boosted diesel engine air charge system [81]. The developed controller coordinates the eBoost, VGT, and EGR actuators to regulate the intake manifold pressure, exhaust manifold pressure, and

EGR rate to required set points.

In this chapter, the performance improvement is first studied through a GT-SUITE model with added eBoost. Both steady-state and transient performance is shown to be improved by properly controlling the eBoost speed. A control-oriented engine air-path model has been developed for model-based eBoost control. The model is validated on a component base with steady-state engine test data. Because the available data do not include the eBoost, the eBoost compressor and motor model are not validated explicitly. The model has been linearized about engine steady-state operating points and the linear quadratic controller has been designed to regulate boost pressure and EGR rate to the desired levels. Engine tests have been performed to validate the simulation results. According to steady-state experimental data, the eBoost is able to improve the overall BSFC with the optimized speed command value and the actual BSFC benefit is close to simulation results. It is also found that the standard bypass valve is not suitable due to the leakage at closing position, which significantly reduces the eBoost efficiency. Transient test results validated that the eBoost is able to reduce the boost tracking response time.

4.2 Engine air charge system model

The air charge system layout is shown in Figure 4.1, where three parts are included in this model: engine, turbocharger and eBoost.

In order to implement eBoost model to engine air charge system, a simplified three-state engine air charge model is adopted first. The dynamic states of the model are intake manifold pressure (p_2), exhaust manifold pressure (p_3) and turbocharger speed (ω_{tc}). The state equations can be found in (4.1).

$$\dot{p}_2 = \frac{RT_2}{V_2}\left(\dot{m}_c + \dot{m}_{\text{egr}} - \dot{m}_{\text{in}}\right) \tag{4.1a}$$

$$\dot{p}_3 = \frac{RT_3}{V_3}\left(-\dot{m}_t - \dot{m}_{\text{egr}} + \dot{m}_{\text{exh}}\right) \tag{4.1b}$$

$$\dot{\omega}_{tc} = \frac{1}{J_c\omega_{tc}}\left(\dot{W}_t - \dot{W}_c - \dot{W}_l\right) \tag{4.1c}$$

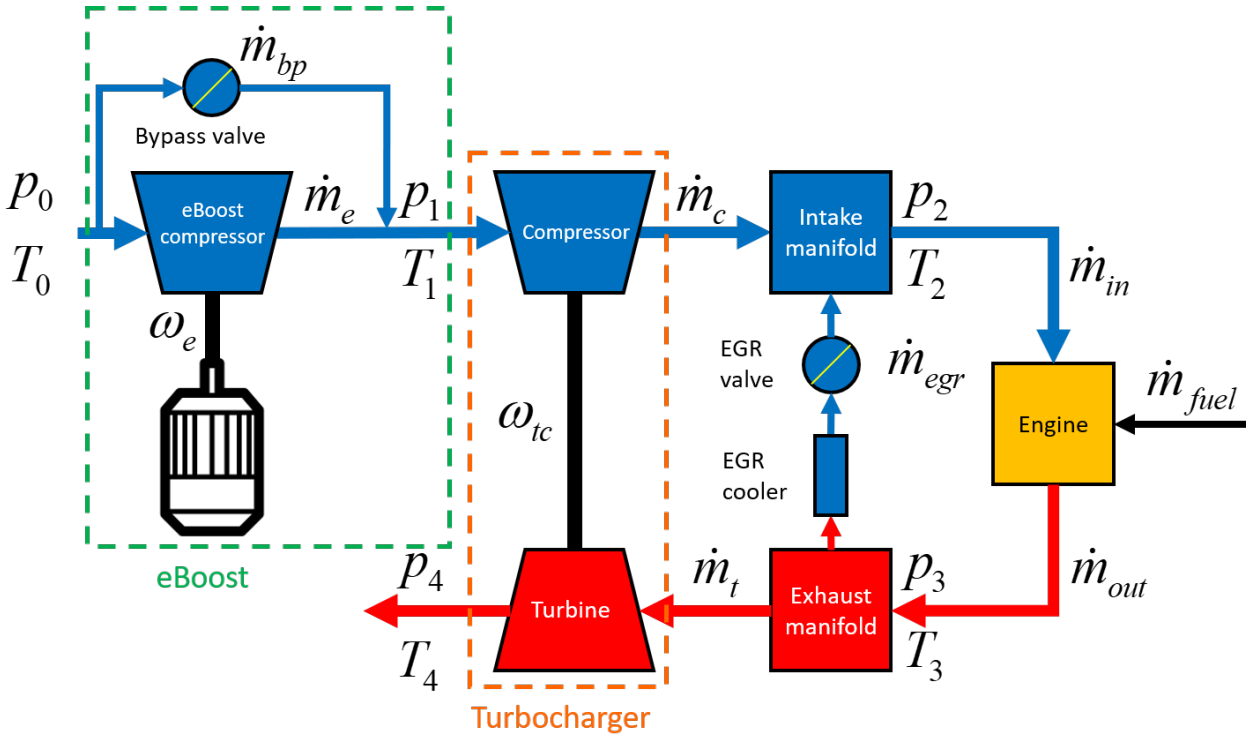

Figure 4.1: System layout for engine air path with eBoost

Each of the physical quantities in the equations is investigated and validated in the following sections. The model for each component is identified using the steady-state engine test data. There are totally 224 data points used for this model calibration. After the model is validated component-by-component, it is further validated using transient engine test data.

4.2.1 Engine intake and exhaust mass flow rate

It is common to model the engine breathing process of four-stroke engines using the speed density equation. The rate of mass flow from intake manifold to engine cylinder $\dot{m}_{\text{in}}$ can be modeled as:

$$\dot{m}_{\text{in}} = \frac{\eta_{\text{vol}} p_2 N_e V_d}{120 R T_2} \tag{4.2}$$

where η_{vol} is the volumetric efficiency of the engine; N_e is the engine speed in r/min; and V_d is the displacement volume.

The volumetric efficiency is a function of engine speed and boost pressure, and can be modeled as:

$$\eta_{\text{vol}} = k_{ve,1}\sqrt{p_2} + k_{ve,2}\sqrt{N_e} + k_{ve,3} \tag{4.3}$$

where $k_{ve,1}$, $k_{ve,2}$ and $k_{ve,3}$ are parameters to be identified. With test data of engine intake mass flow rate, intake manifold pressure and temperature, the volumetric efficiency can be easily identified, leading to calibrated engine intake mass flow rate shown in Figure 4.2. The calibrated values are listed in Table 4.1.

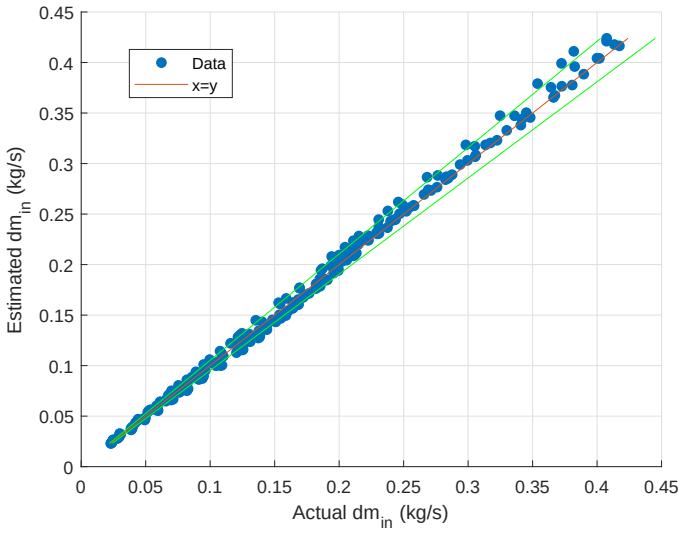

Figure 4.2: Model identification results for engine intake mass flow rate

Table 4.1: Model calibration - engine intake mass flow rate

Parameter	Model value
$k_{ve,1}$	1.09×10^{-5}
$k_{ve,2}$	0.0018
$k_{ve,3}$	0.7703

Engine exhaust mass flow rate can be modeled as the sum of engine intake mass flow rate and fuel injection mass flow rate. This is based on the assumption that in-cylinder residual gas fraction is negligible. Therefore:

$$\dot{m}_{\text{exh}} = \dot{m}_{\text{in}} + \dot{m}_{\text{fuel}} \tag{4.4}$$

where fuel injection mass flow rate is calculated based on the commanded fueling rate in each cylinder per cycle. For the target engine, which has eight cylinders, the fuel injection mass flow rate can be expresses as in (4.5). The unit for fuel command u_{fuel} is mg/stroke.

$$\dot{m}_{\text{fuel}} = \frac{8 \times 10^{-6}}{120} u_{\text{fuel}} N_e \tag{4.5}$$

4.2.2 EGR mass flow rate

EGR mass flow rate can be modeled using the standard throttle flow equation, which has two inputs: effective area (A_{eff}) as a function of throttle position, and pressure ratio $\left(\frac{p_{ds}}{p_{us}}\right)$. Depending on the magnitude of pressure ratio, the calculation may be different. The standard form of throttle flow is shown below.

$$\dot{m}_{th} = A_{\text{eff}} \frac{p_{us}}{\sqrt{RT_{us}}} \psi\left(\frac{p_{ds}}{p_{us}}\right) \tag{4.6}$$

For unchoked flow, meaning

$$\frac{p_{ds}}{p_{us}} > \left(\frac{2}{\gamma+1}\right)^{\frac{\gamma}{\gamma-1}}$$

$$\psi\left(\frac{p_{ds}}{p_{us}}\right) = \sqrt{\frac{2\gamma}{\gamma-1}\left[\left(\frac{p_{ds}}{p_{us}}\right)^{\frac{2}{\gamma}} - \left(\frac{p_{ds}}{p_{us}}\right)^{\frac{\gamma+1}{\gamma}}\right]} \tag{4.7}$$

For choked flow, meaning

$$\frac{p_{ds}}{p_{us}} \leq \left(\frac{2}{\gamma+1}\right)^{\frac{\gamma}{\gamma-1}}$$

$$\psi\left(\frac{p_{ds}}{p_{us}}\right) = \sqrt{\gamma\left(\frac{2}{\gamma+1}\right)^{\frac{\gamma+1}{\gamma-1}}} \tag{4.8}$$

For EGR mass flow rate, effective area is a function of EGR valve opening $\left(u_{\text{egr}}\right)$, and pressure ratio is the ratio of exhaust manifold pressure to intake manifold pressure. Thus,

$$\dot{m}_{\text{egr}} = A_{\text{egr}} \frac{p_3}{\sqrt{RT_3}} \psi\left(\frac{p_2}{p_3}\right) \tag{4.9}$$

where A_{egr} can be modeled as a second order polynomial of u_{egr}, as indicated by Figure 4.3.

$$A_{\text{egr}} = k_{ea,1} u_{\text{egr}}^2 + k_{ea,2} u_{\text{egr}} + k_{ea,3} \tag{4.10}$$

where the parameter values are given in Table 4.2. The identification results are shown in Figure 4.4.

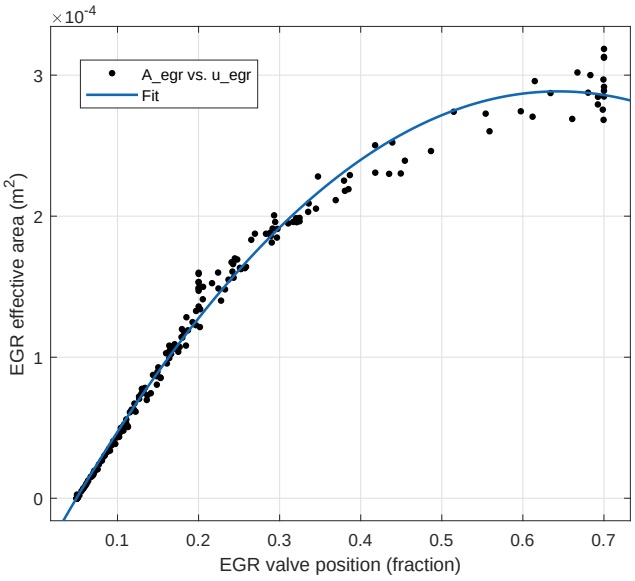

Figure 4.3: EGR effective area vs. EGR valve position

Table 4.2: Model calibration - EGR mass flow rate

Parameter	Model value
$k_{ea,1}$	-8.15×10^{-4}
$k_{ea,2}$	0.0011
$k_{ea,3}$	-4.98×10^{-5}

4.2.3 Intake manifold temperature

Considering the charge air cooler (CAC) after the compressor and EGR cooler after EGR valve, the temperature in the intake manifold is the mixed temperature from both intake charge air cooler and EGR cooler. These components can be treated as standard heat exchangers whose effectiveness is used to model the heat the heat transfer through the coolers. The outlet temperature of the coolers can be written as:

$$T_{\text{cac}} = T_c(1 - \varepsilon_{\text{cac}}) + T_{\text{cool,cac}}\varepsilon_{\text{cac}} \tag{4.11}$$

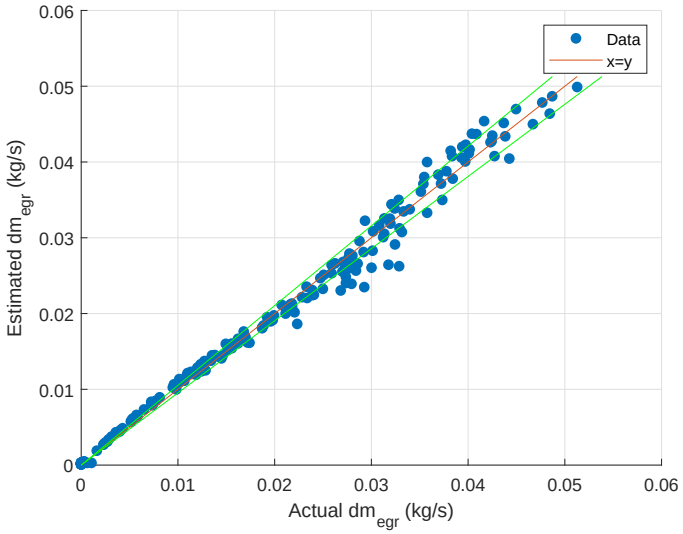

Figure 4.4: Model identification results for EGR mass flow rate

for CAC, and

$$T_{\text{egr}} = T_3(1 - \varepsilon_{\text{egr}}) + T_{\text{cool,egr}}\varepsilon_{\text{egr}} \tag{4.12}$$

for EGR cooler. $T_{\text{cool,cac}}$ is the coolant temperature at CAC and $T_{\text{cool,egr}}$ is the coolant temperature at EGR cooler. The heat transfer efficiency coefficients ε_{cac} and ε_{egr} are assumed to be constant, and their values are shown in Table 4.3.

Table 4.3: Model calibration - coolant temperature

Parameter	Model value
ε_{cac}	0.98
ε_{egr}	0.97

T_c is the main compressor outlet temperature, which is estimated by a third order polynomial equation with compressor mass flow rate and TC shaft speed as input:

$$\begin{aligned} T_c = \quad & k_{ct,1} + k_{ct,2}\dot{m}_c + k_{ct,3}N_{tc} + k_{ct,4}\dot{m}_c^2 + k_{ct,5}\dot{m}_c N_{tc} + k_{ct,6}N_{tc}^2 + k_{ct,7}\dot{m}_c^3 \\ & + k_{ct,8}\dot{m}_c^2 N_{tc} + k_{ct,9}\dot{m}_c N_{tc}^2 + k_{ct,10}N_{tc}^3 \end{aligned} \tag{4.13}$$

The model values for the parameters are given in Table 4.4. Model fitting results are given in Figure 4.5.

Table 4.4: Model calibration - compressor outlet temperature

Parameter	Model value
$k_{ct,1}$	356.81
$k_{ct,2}$	235.79
$k_{ct,3}$	4.38×10^{-4}
$k_{ct,4}$	3.53×10^{3}
$k_{ct,5}$	-0.0254
$k_{ct,6}$	1.82×10^{-9}
$k_{ct,7}$	1.55×10^{4}
$k_{ct,8}$	-0.1837
$k_{ct,9}$	6.76×10^{-7}
$k_{ct,10}$	-3.71×10^{-13}

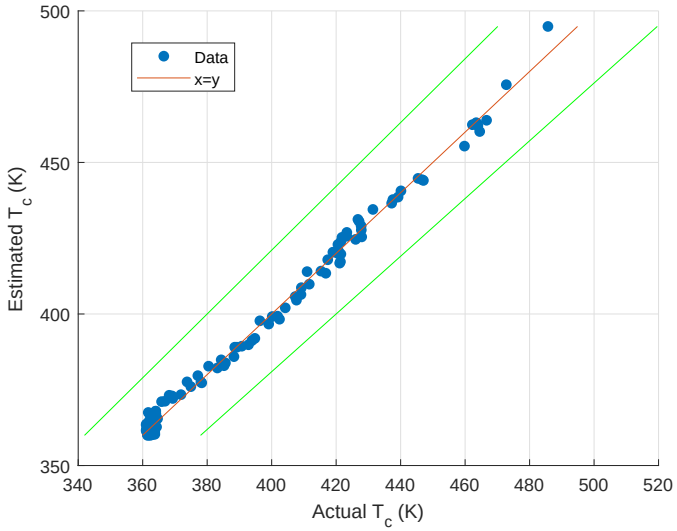

Figure 4.5: Model identification results for compressor outlet temperature

Assuming that the mixture temperature in the intake manifold is based on each mass flow rate, thus

$$T_2 = \frac{\dot{m}_c T_{\text{cac}} + \dot{m}_{\text{egr}} T_{\text{egr}}}{\dot{m}_c + \dot{m}_{\text{egr}}} \tag{4.14}$$

The identification results are shown in Figure 4.6.

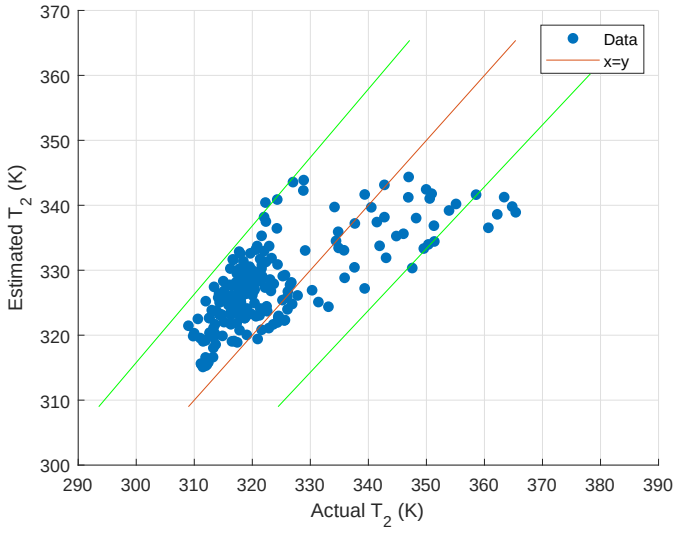

Figure 4.6: Model identification results for intake manifold temperature

4.2.4 Exhaust manifold temperature

The calculation of exhaust manifold temperature is based on engine exhaust temperature and heat exchange between the engine exhaust flow and exhaust pipe. The exhaust manifold temperature is modeled as a result of heat exchange process:

$$T_3 = T_0 + (T_{\text{exh}} - T_0) \exp\left(-\frac{k_{et,1}}{\dot{m}_{\text{exh}} c_p}\right) \tag{4.15}$$

The engine exhaust temperature is modeled based on the Seliger cycle [82].

$$T_{\text{exh}} = k_{et,2} \left(\frac{p_3}{p_2}\right)^{1-\frac{1}{\gamma}} r_c^{1-\gamma} \cdot \left[\frac{\dot{m}_{\text{fuel}} \cdot \text{LHV}}{\dot{m}_{\text{exh}} c_p} (1 - x_r) + T_2 r_c^{\gamma-1}\right] \tag{4.16}$$

where r_c is the engine compression ratio; and x_r is cylinder residual gas fraction. The model parameters are calibrated as shown in Table 4.5 and Figure 4.7

Table 4.5: Model calibration - exhaust manifold temperature

Parameter	Model value
$k_{et,1}$	28.3286
$k_{et,2}$	1.0158

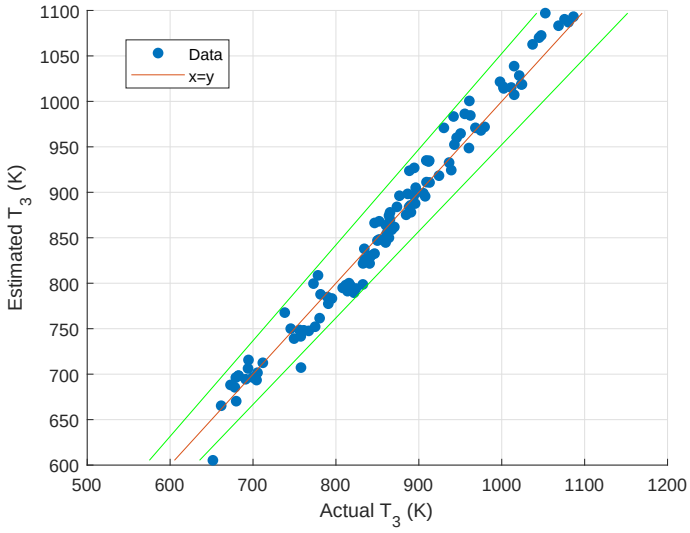

Figure 4.7: Model identification results for exhaust manifold temperature

4.2.5 Turbine power and mass flow rate

The physics-based control-oriented turbine power model can be found in the open literature. The turbine operation depends on turbine inlet condition and TC shaft speed:

$$\dot{W}_t = \frac{1}{60} N_{tc} \dot{m}_t^2 \frac{1}{B} \frac{RT_3}{p_3} \tan \alpha_1 \tag{4.17}$$

where N_{tc} is the TC shaft speed in r/min; $\dot{m}_t$ is the mass flow rate through turbine; B is turbine inlet clearance, which can be a tuning parameter; and α_1 is the gas entry angle to the rotor and is determined by the vane guide blade angular position controlled by VGT position actuator. Their relation can be shown in Figure 4.8. In this study, the vane angle is modeled as a polynomial function of VGT command and TC shaft speed:

$$\begin{aligned} \alpha_1 = \quad & k_{\alpha,1} + k_{\alpha,2} u_{\text{vgt}} + k_{\alpha,3} N_{tc} + k_{\alpha,4} u_{\text{vgt}}^2 + k_{\alpha,5} u_{\text{vgt}} N_{tc} + k_{\alpha,6} N_{tc}^2 + k_{\alpha,7} u_{\text{vgt}}^3 \\ & + k_{\alpha,8} u_{\text{vgt}}^2 N_{tc} + k_{\alpha,9} u_{\text{vgt}} N_{tc}^2 + k_{\alpha,10} N_{tc}^3 \end{aligned} \tag{4.18}$$

where u_{vgt} is the VGT control input. The identified parameters are shown in Table 4.6. Model calibration results are shown in Figure 4.9.

The mass flow rate through a turbine can be modeled as a similar function to throttle

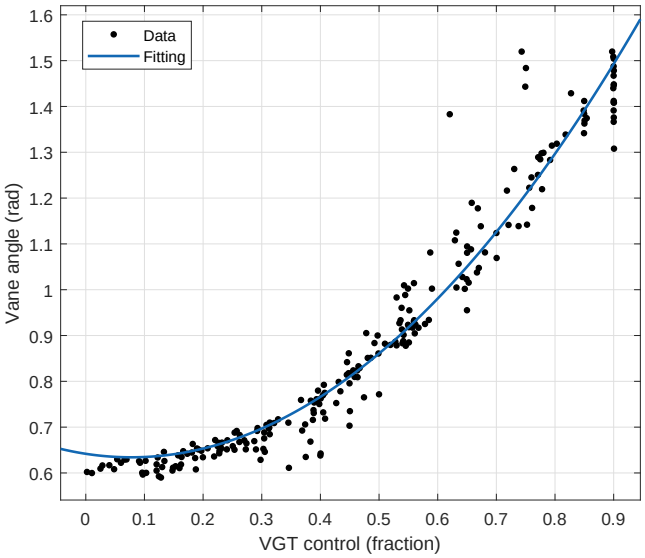

Figure 4.8: VGT control input vs. vane angle

Table 4.6: Model calibration - turbine power

Parameter	Model value
$k_{\alpha,1}$	1.6517
$k_{\alpha,2}$	-2.6254
$k_{\alpha,3}$	-3.60×10^{-5}
$k_{\alpha,4}$	5.4184
$k_{\alpha,5}$	2.54×10^{-5}
$k_{\alpha,6}$	4.20×10^{-10}
$k_{\alpha,7}$	-2.7310
$k_{\alpha,8}$	-1.46×10^{-5}
$k_{\alpha,9}$	-7.56×10^{-10}
$k_{\alpha,10}$	-1.68×10^{-15}

flow:

$$\dot{m}_{\text{vgt}} = A_{\text{vgt}} \frac{p_3}{\sqrt{RT_3}} \psi \left(\frac{p_4}{p_3} \right) \tag{4.19}$$

where the coefficients are calibrated as shown in Table 4.6 and the model fit results are shown in Figure 4.10. Calculation of ψ is defined in equation (4.7) and (4.8).

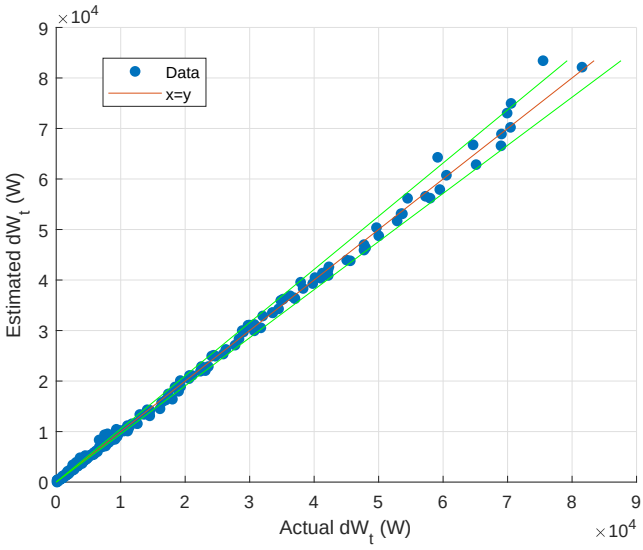

Figure 4.9: Model identification results for turbine power

Table 4.7: Model calibration - turbine mass flow rate

Parameter	Model value
$k_{va,1}$	5.30×10^{-4}
$k_{va,2}$	1.96×10^{-4}
$k_{va,3}$	3.99×10^{-9}
$k_{va,4}$	-7.42×10^{-4}
$k_{va,5}$	-4.57×10^{-9}

4.2.6 Power loss model.

The mechanical loss to the turbocharger shaft is a combination of both heat transfer and friction losses. In this study, only friction loss is considered. According to [83], power loss can be modeled as a polynomial function of rotational speed:

$$\dot{W}_l = k_{pl,1} N_{tc}^2 + k_{pl,2} N_{tc} + k_{pl,3} \tag{4.20}$$

Since there is no direct measurement of power loss, the identification for turbine power and power loss should be carried out together. Table 4.8 gives the values of calibrated parameters.

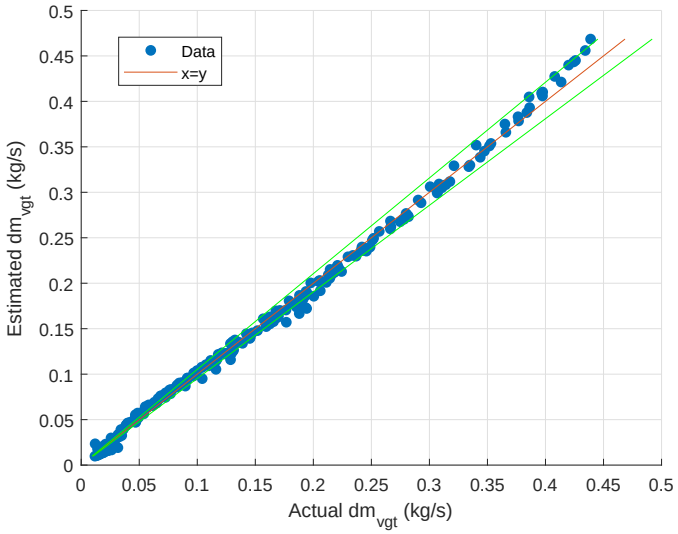

Figure 4.10: Model identification results for turbine mass flow rate

Table 4.8: Model calibration - turbo shaft power loss

Parameter	Model value
$k_{pl,1}$	6.96×10^{-7}
$k_{pl,2}$	2.36×10^{-11}
$k_{pl,3}$	7.50×10^{-9}

4.2.7 Compressor power and mass flow rate.

Although map-based empirical models for a centrifugal compressor have been widely used [84], they have poor extrapolation outside the mapped operating conditions. A physics-based compressor model is able to provide good predictions and relatively low computational cost. A reduced complexity model of compressor power is adopted in this study to efficiently simulate the compressor behavior. The model is generalized such that only two variables are used as inputs: mass flow rate and rotational speed.

$$\dot{W}_c = k_{cp,1}\dot{m}_c N_{tc}^2 + k_{cp,2}\dot{m}_c^2 N_{tc} + k_{cp,3}\dot{m}_c^3 \tag{4.21}$$

where $k_{cp,1}$, $k_{cp,2}$ and $k_{cp,1}$ are parameters to be identified and their values are listed in Table 4.9. The model identification results can be found in Figure 4.11.

Table 4.9: Model calibration - main compressor power

Parameter	Model value
$k_{cp,1}$	2.24×10^{-5}
$k_{cp,2}$	-2.7366
$k_{cp,3}$	1.68×10^{5}

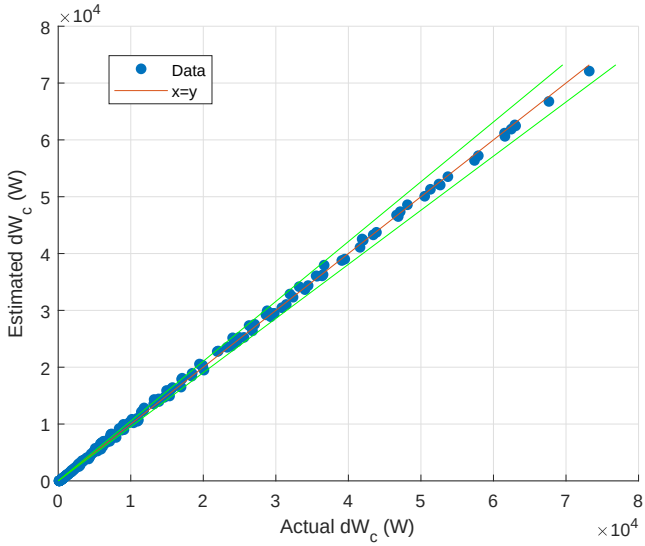

Figure 4.11: Model identification results for main compressor power

Compressor mass flow rate can be modeled as a De Laval nozzle [85] based on the turbocharger geometry with external work input from the compressor wheel:

$$\dot{m}_c = \frac{A_c p_1}{\sqrt{RT_1}} \Phi\left(\frac{p_2}{p_1}, \omega_{tc}\right) \tag{4.22}$$

The critical pressure ratio r_{crit} is defined as

$$r_{\text{crit}} = 1 + \frac{\mu r_{\text{exit}}^2 \omega_{tc}^2}{c_p T_1} \tag{4.23}$$

If

$$\frac{p_2}{p_1} < \left(\frac{2r_{\text{crit}}}{\gamma + 1}\right)^{\frac{\gamma}{\gamma - 1}}$$

Then

$$\Phi\left(\frac{p_2}{p_1}, \omega_{tc}\right) = \sqrt{\gamma \left(\frac{2r_{crit}}{\gamma + 1}\right)^{\frac{\gamma+1}{\gamma-1}}} \tag{4.24}$$

If

$$\frac{p_2}{p_1} \geq \left(\frac{2r_{crit}}{\gamma+1}\right)^{\frac{\gamma}{\gamma-1}}$$

Then

$$\Phi\left(\frac{p_2}{p_1}, \omega_{tc}\right) = \left(\frac{p_2}{p_1}\right)^{\frac{1}{\gamma}} \sqrt{\frac{2\gamma}{\gamma-1}\left[r_{\text{crit}} - \left(\frac{p_2}{p_1}\right)^{\frac{\gamma-1}{\gamma}}\right]} \tag{4.25}$$

where r_{exit} is the radius at the outlet of compressor.

$$\mu = 0.8\left(\sigma_0 + \Delta\sigma_0 + \tan\beta_{2B,0}\frac{C_{r,\text{exit},c}}{U_{\text{exit}}}\right) \tag{4.26}$$

$$\sigma_0 = 1 - \frac{1}{2}\left[1 - \exp\left(-\frac{2\pi}{Z}\cos\beta_{2B,0}\right)\right] \tag{4.27}$$

$$A_c = 2\pi r_{\text{dif}} B_{\text{dif}}\left[C_{d,\max} - C_{d,cor}\left(U_{\text{exit}} - U_{\text{exit,opt}}\right)^2\right] \tag{4.28}$$

The identification results for compressor mass flow rate are shown in Table 4.10 and Figure 4.12.

Table 4.10: Model calibration - compressor mass flow rate

Parameter	Model value
B_{dif}	7.95×10^{-4}
$C_{d,\max}$	1.9673
$C_{d,\text{cor}}$	1.23×10^{-5}
$U_{\text{exit,opt}}$	334.44

4.2.8 Model validation with transient data.

Up to this point, all the components in the VGT-EGR system model, shown in Figure 4.1, have been calibrated using steady-state test data. The third-order nonlinear model of engine air charge system is further validated using the FTP 75 driving cycle data. The results are shown in Figure 4.13.

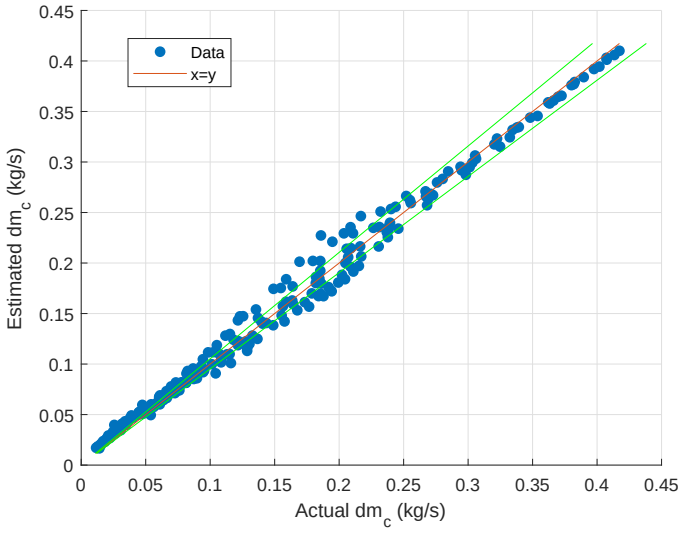

Figure 4.12: Model identification results for main compressor mass flow rate

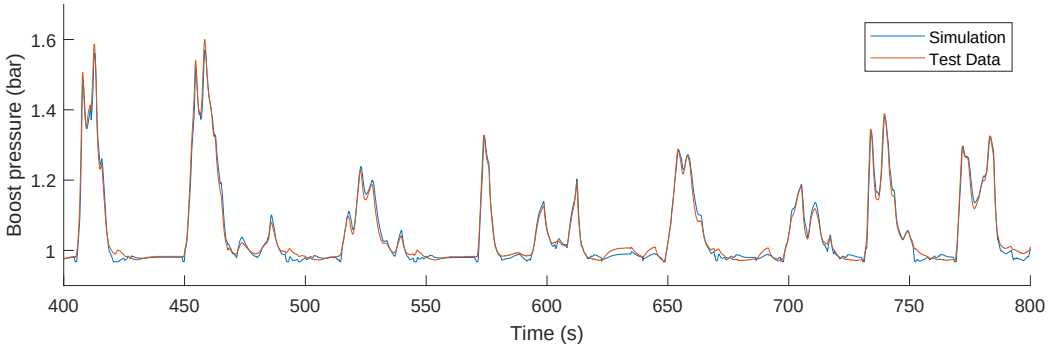

Figure 4.13: Model validation with FTP 75 driving cycle data

4.3 Extended air charge model with eBoost system

By integrating electrically driven compressor (e-compressor) and motor shaft dynamics to the developed 3-state air charge system model, the system becomes a fifth-order nonlinear model. The additional two states are upstream pressure of main compressor (downstream pressure of e-compressor) and electric motor shaft speed, respectively. State equations of the

extended air charge system model are shown below.

$$\dot{p}_1 = \frac{RT_1}{V_1}\left(\dot{m}_e + \dot{m}_{bp} - \dot{m}_c\right) \tag{4.29a}$$

$$\dot{p}_2 = \frac{RT_2}{V_2}\left(\dot{m}_c + \dot{m}_{\text{egr}} - \dot{m}_{\text{in}}\right) \tag{4.29b}$$

$$\dot{p}_3 = \frac{RT_3}{V_3}\left(-\dot{m}_t - \dot{m}_{\text{egr}} + \dot{m}_{\text{exh}}\right) \tag{4.29c}$$

$$\dot{\omega}_{tc} = \frac{1}{J_c\omega_{tc}}\left(\dot{W}_t - \dot{W}_c - \dot{W}_l\right) \tag{4.29d}$$

$$\dot{\omega}_e = \frac{1}{J_e\omega_e}\left(\dot{W}_m - \dot{W}_e - \dot{W}_l\right) \tag{4.29e}$$

4.3.1 The eBoost compressor power and mass flow rate

The model for eBoost compressor power and mass flow rate is adopted from main compressor. Thus,

$$\dot{W}_e = k_{ep,1}\dot{m}_e\omega_e^2 + k_{ep,2}\dot{m}_e^2\omega_e + k_{ep,3}\dot{m}_e^3 \tag{4.30}$$

where $k_{ep,1}$, $k_{ep,2}$ and $k_{ep,1}$ are calibration parameters whose values are shown in Table 4.11.

Table 4.11: Model calibration - eBoost compressor power

Parameter	Model value
$k_{ep,1}$	2.21×10^{-3}
$k_{ep,2}$	-37.25
$k_{ep,3}$	3.47×10^{5}

The eBoost compressor mass flow rate can be modeled similarly:

$$\dot{m}_e = \frac{A_e p_0}{\sqrt{RT_0}}\Phi\left(\frac{p_1}{p_0}, \omega_e\right) \tag{4.31}$$

where Φ is the same function as defined in equation (4.23), (4.24) and (4.25). A_e is calculated in the same way as A_c defined in equation (4.28).

4.3.2 Motor drive power

The motor power output is modeled as a function of motor drive torque and motor speed. Thus,

$$\dot{W}_m = \tau_d \cdot \omega_e \tag{4.32}$$

The characteristics of motor is integrated using the efficiency map provided by the manufacturer.

4.3.3 Bypass mass flow rate

Let $\dot{m}_{bp}$ be the mass flow rate passing through the bypass valve, which can be modeled as the standard throttle flow:

$$\dot{m}_{bp} = A_{bp} \frac{p_0}{\sqrt{RT_0}} \psi \left(\frac{p_1}{p_0} \right) \tag{4.33}$$

where A_{bp} can be simplified as a proportional function of u_{bp},

$$A_{bp} = 6 \times 10^{-4} u_{bp} \tag{4.34}$$

and ψ is calculated based on the standard flow equations as defined in (4.7) and (4.8).

4.4 System analysis of the electrically boosted diesel engine

To perform a preliminary evaluation of benefit of eBoost on engine performance, a comprehensive study, which is carried out in GT-SUITE simulation environment, has been completed through 1-D simulations, using both design of experiment and optimization. The GT-SUITE model is developed based on the existing Ford 6.7 L, 8-cylinder diesel engine model equipped with VGT and EGR. The eBoost compressor and electric motor components are added, and the corresponding manufacturer supplied maps are implemented. The model has been validated with engine test data.

4.4.1 Steady-state performance

First, the baseline lookup tables for VGT rack position, EGR valve position and brake specific fuel consumption (BSFC) have been generated based on manufacturer mapped target boost pressure and EGR rate. These maps are useful to evaluate the effect of eBoost to the system performance. The generated maps are shown in Figure 4.14.

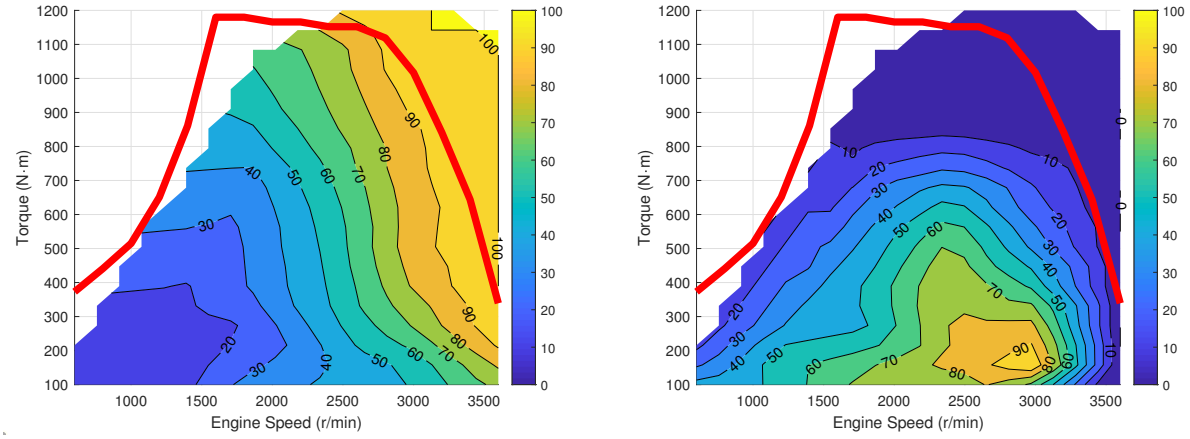

(a) VGT position

(b) EGR position

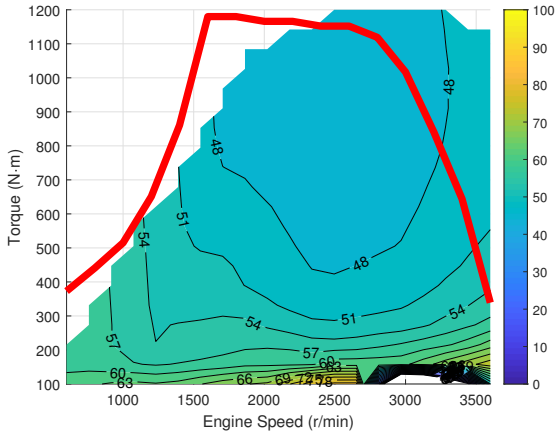

(c) BSFC

Figure 4.14: Baseline engine maps for VGT, EGR, and BSFC (percentage of maximum value)

Next step is to construct a design-of-experiment (DOE) simulation and let the eBoost power sweep within a reasonable range. The designed operating conditions are summarized in Table 4.12.

Table 4.12: GT-SUITE DOE simulation setup

Simulation label		Simulation setup	
Parameter	Minimum	Maximum	# of level
Engine speed (r/min)	600	3600	6
Fuel injection (mg/stroke)	10	120	12
eBoost power (kW)	0	9	10
Bypass valve (degree)	0	90	2

VGT and EGR are controlled in the same way as in the baseline simulation: VGT is controlled to track target boost pressure and EGR is controller to track target EGR rate. eBoost power is maintained constant for each simulation. Bypass valve is on-off controlled so that the bypass valve is wide open when eBoost power is zero and fully closed when eBoost power is not zero.

At each engine speed and load condition, the operating point with the best BSFC has been selected as "optima" operating condition. The optimal points form a new map, leading to the best eBoost power with the lowest BSFC. Note that the BSFC in this case considers the eBoost power used as loss. Thus, the new BSFC, called effective BSFC, is calculated as

$$\mathrm{BSFC}_{\mathrm{eff}} = \frac{\mathrm{BSFC} \cdot \dot{W}_b}{\dot{W}_b - \frac{1}{\eta_e \eta_m} \dot{W}_m} \tag{4.35}$$

where $\mathrm{BSFC}_{\mathrm{eff}}$ is the effective BSFC; $\dot{W}_b$ is brake power; η_e is the battery energy conversion efficiency; and η_m is the motor characteristic efficiency.

The results of DOE simulations are shown in Figure 4.15 and 4.16. The results indicate that under low speed low load condition, eBoost power improves the steady-state fuel economy, leading to increased steady-state output torque for the same BSFC. The corresponding VGT and EGR controls also change. VGT increases its opening when eBoost is engaged because additional power is added to maintain the same boost pressure, leading to reduced required power from turbine. EGR increases its opening in this situation because when turbine power is reduced, exhaust pressure decreases. As a result, to maintain the same EGR rate, EGR valve opening should be increased.

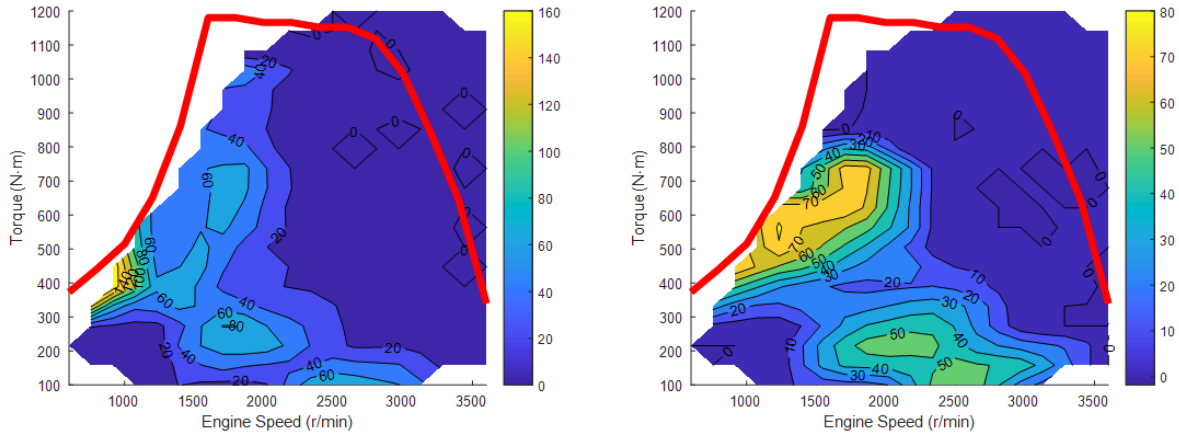

(a) DOE VGT opening increase (%) (b) DOE EGR opening increase (%)

Figure 4.15: DOE results for VGT and EGR

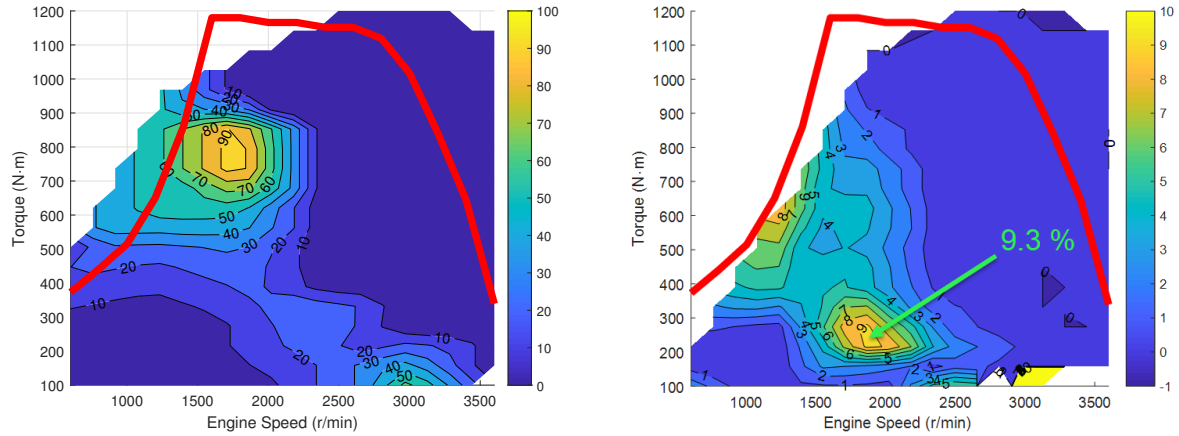

(a) DOE optimal eBoost power (%) (b) DOE BSFC reduction (%)

Figure 4.16: DOE results for eBoost power (normalized percentage) and BSFC

A comparison between the upstream and downstream configuration of eBoost is of great interest. The causality of system input and output is shown in Figure 4.17 and summarized as follows. There are two paths for eBoost to affect BSFC. The first path, which is the direct path, explicitly increases BSFC due to additional power consumption. The second path also called the indirect path, decreases turbine power so that exhaust pressure is lowered, leading to improved combustion efficiency. In this process, turbocharger efficiency (η_{tc}) and eBoost efficiency (η_{eboost}) are competing and this shifts the optimal operational point.

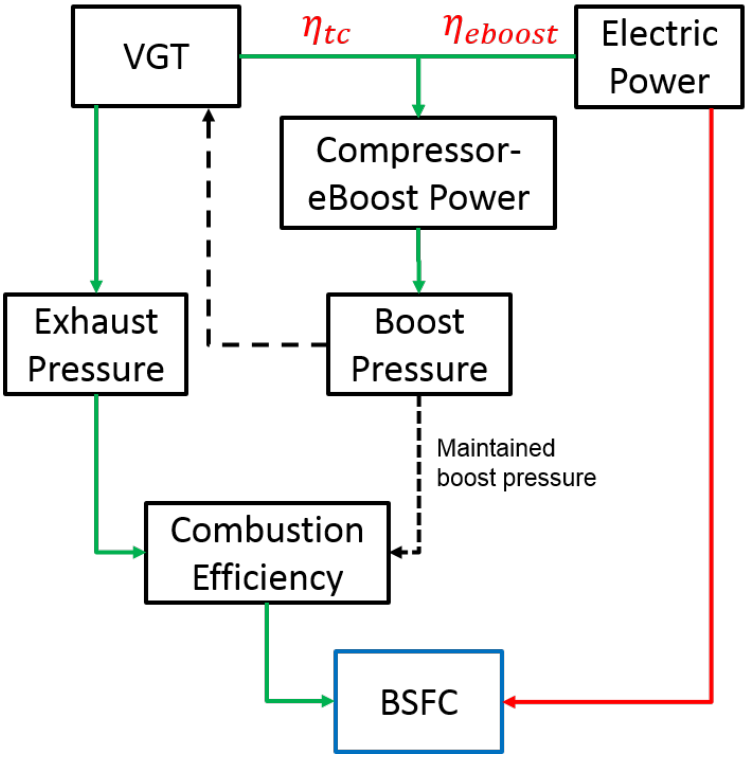

Figure 4.17: System causality

The results of two configurations are shown below.

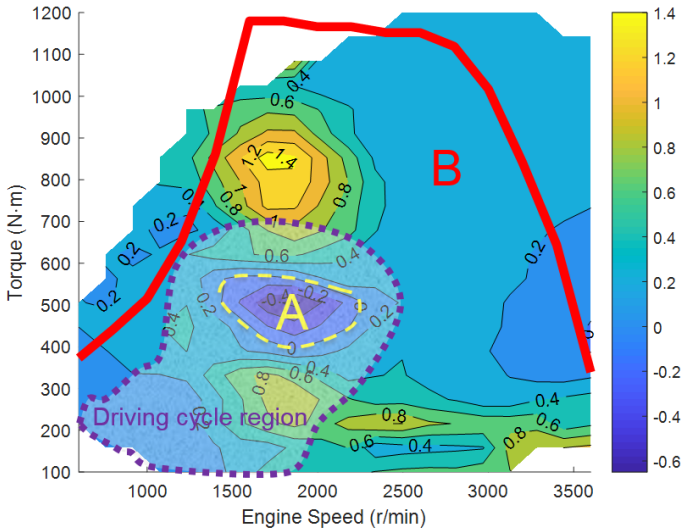

Figure 4.18: Percentage BSFC difference (upstream-downstream)

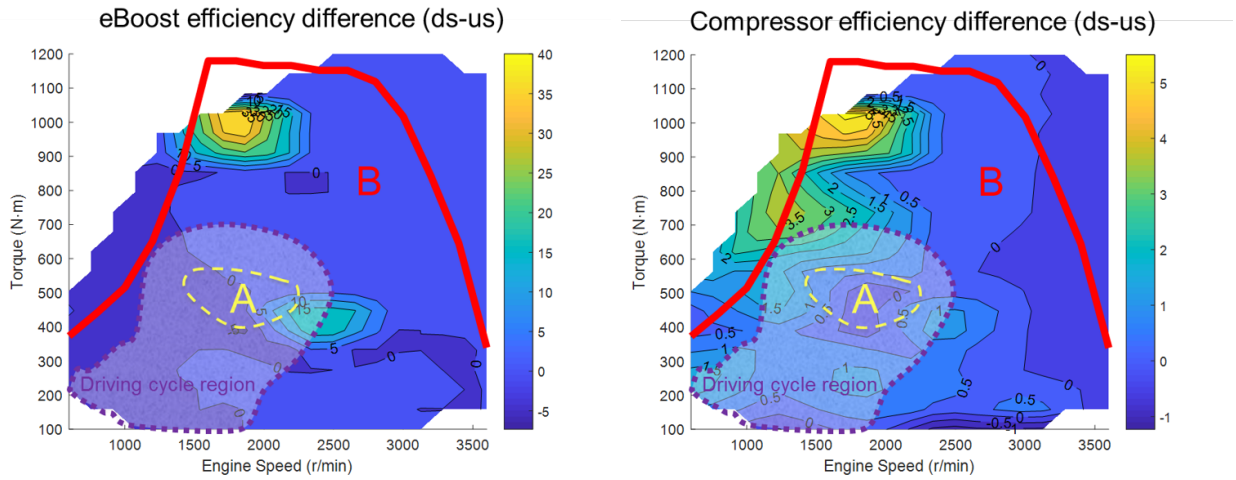

(a) eBoost compressor efficiency difference (%) (b) Main compressor efficiency difference (%)

Figure 4.19: Compressor efficiency difference (downstream-upstream)

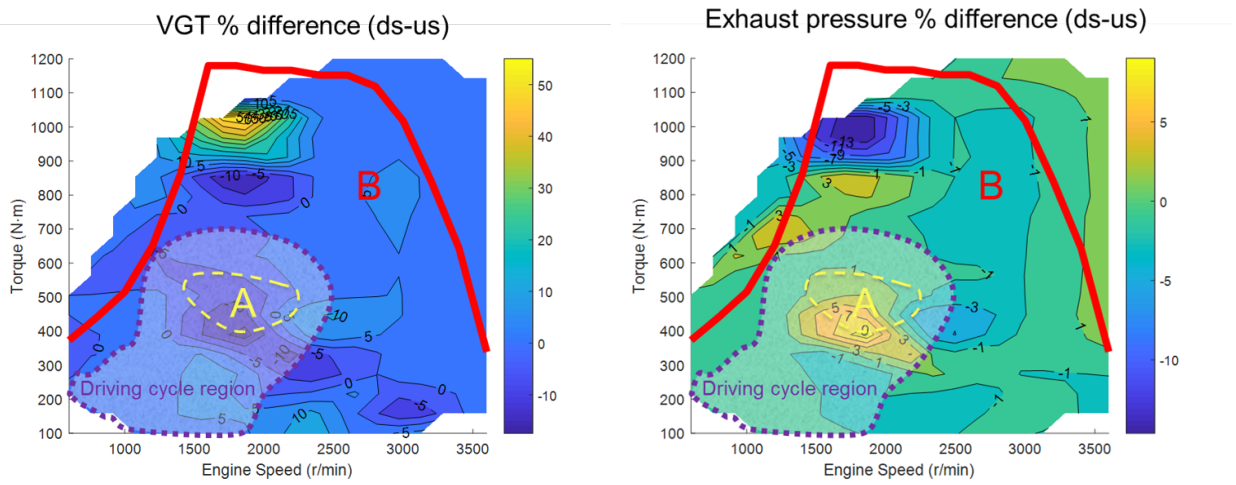

(a) VGT position difference (%) (b) Exhaust manifold pressure difference (%)

Figure 4.20: VGT position and exhaust manifold pressure difference (downstream-upstream)

As shown in Figure 4.18, Region A is where the upstream configuration is preferred and Region B is where downstream is preferred. At 1800 r/min, downstream is preferred in low and high load conditions while upstream is preferred at mid load conditions. As shown in Figure 4.19a, eBoost efficiency is decreased by up to 7% for downstream configuration at mid load. At high load conditions, eBoost efficiency is increased by up to 40%. As shown in Figure 4.19b and Figure 4.20a, Compressor efficiency is decreased by 1%, which is much

less than decrement in eBoost. VGT opening is reduced by 10% at 1800 r/min, mid load. Considering the change in exhaust manifold pressure, as shown in Figure 4.20b, increased exhaust pressure indicates decreased combustion efficiency. This explains the increase in BSFC for the downstream configuration.

In summary, upstream configuration is only preferred when engine is operating at mid speed and load conditions (Region A). To maintain the same boost pressure and minimal BSFC, eBoost and TC are competing based on their operational efficiencies. If eBoost is relatively more efficient than TC, more electric power is applied and VGT opening reduces; and if eBoost is relatively less efficient than TC, less electric power is applied and VGT opening increases. In the two configurations, eBoost is operating at different conditions, such as compressor speed, pressure ratio, temperature, etc. Difference in eBoost and TC efficiencies (thus operations) is the key in the cause of the difference in BSFC. This indicates that there is room for co-optimization of eBoost and TC maps.

4.4.2 Transient performance

To study the transient performance change due to eBoost, various scenarios have been considered, such as open-loop responses to boost pressure step and to engine load step, and closed-loop response to load step.

The open-loop response to boost pressure step reveals the different response time of VGT turbine and eBoost. The simulation has been performed at 1500 r/min, where load torque is assumed to be 250 N-m. As shown in Figure 4.21, to raise the boost pressure to the same level (0.2 bar up from baseline pressure 1.119 bar), the rise time and settling time with eBoost and bypass valve activation are less than these when VGT is activated. This is consistent with the assumption that electrically driven compressor has much faster response than exhaust gas turbine. The control input for VGT and eBoost is a step function.

As the stepped pressure is increased, the difference in response time becomes larger, as shown in Figure 4.22 for 0.4 bar stepped boost and Figure 4.23 for 0.6 bar stepped boost.

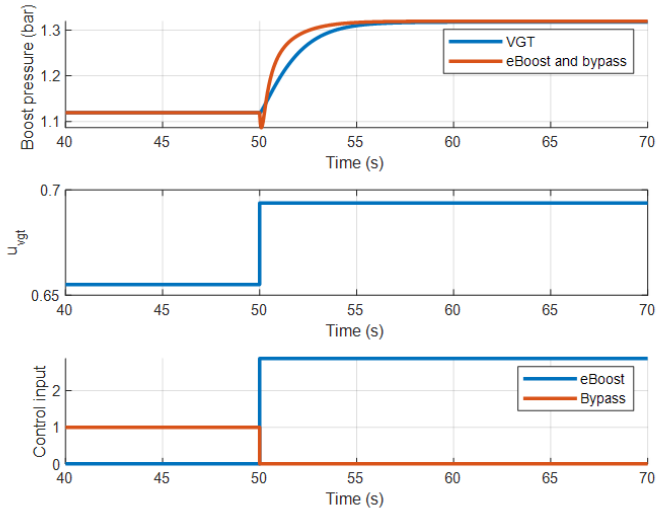

Figure 4.21: Transient response for boost pressure stepped by 0.2 bar

Note that a higher level of eBoost energy required to achieve the higher target boost pressure, is expected.

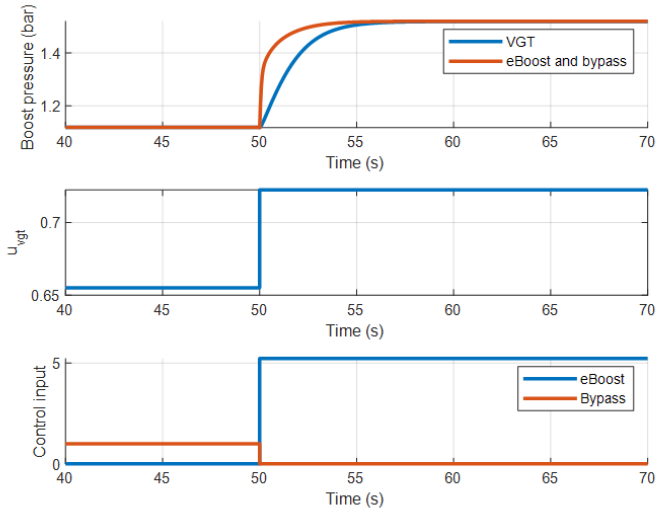

Figure 4.22: Transient response for boost pressure stepped by 0.4 bar

It can be concluded that eBoost has a much faster response than the VGT turbine. To achieve the same boost level, the settling time reduction can be expected to be up to 50% depending on the boost requirement.

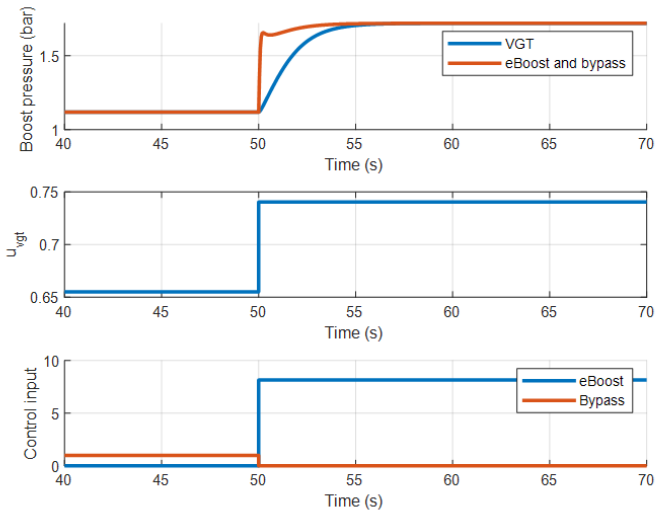

Figure 4.23: Transient response for boost pressure stepped by 0.6 bar

Because the turbo-lag is mainly caused by slow response of available energy at turbine inlet, a more realistic scenario is to include the engine load step by assuming a reasonable dynamics from fuel injection to available energy at exhaust manifold. As shown in Figure 4.24, for a load step from 100 to 500 N-m at 1500 r/min, with a relatively fast response of the exhaust energy, the difference between VGT and eBoost responses are significantly reduced. In this case, the fuel injection is also considered, where the exhaust energy is greatly increased, leading to much larger power to drive the main compressor. A non-minimal phase behavior of eBoost response is also observed in Figure 4.24.

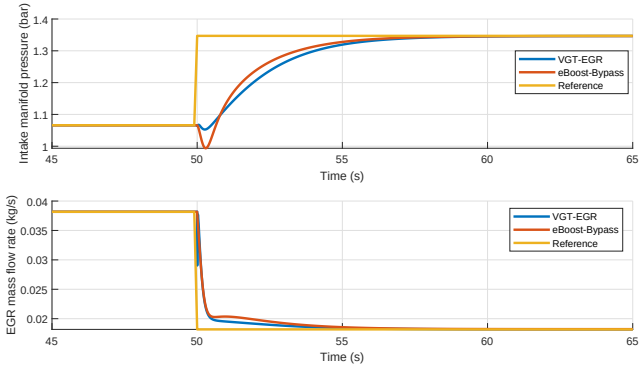

Figure 4.24: Open-loop transient response for load stepped from 100 to 500 N-m

To conclude on the potential of the eBoost system's capability of improving diesel engine torque response, a comparison is made between the case where only VGT is activating to track target boost pressure and the case where both VGT and eBoost are activated. This is accomplished by integrating error-based controllers for VGT, EGR, eBoost and bypass valve in the simulations. VGT is controlled by a PI controller to eliminate both steady-state and transient errors of boost pressure. eBoost and bypass valve are controlled so that they are only active in transient and restore the original state when the error is zero. This ensures that eBoost does not compensate for steady-state boost tracking, which is more realistic for vehicle electric energy management.

In Figure 4.25, where the engine speed is 1500 r/min and load torque is stepped from 100 to 500 N-m, boost pressure and EGR mass flow rate are compared among target level, VGT only, and eBoost assist. The rising time for eBoost assist is significantly reduced. However, due to the drop right after the rise, the overall settling time for both cases are similar. From Figure 4.26, it is clear that spinning of eBoost and closing of bypass valve effectively increase the compressor inlet pressure (p_2) and could lead to fast rising of boost pressure.

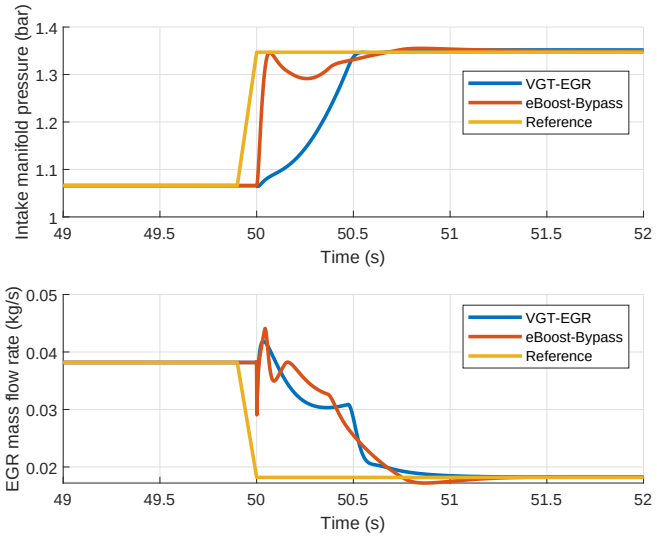

Figure 4.25: Closed-loop transient response for load stepped from 100 to 500 N-m

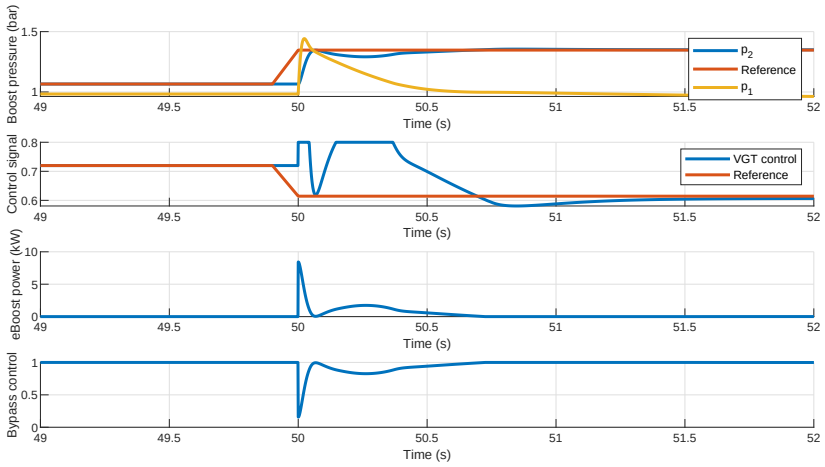

Figure 4.26: Error-based control signals for eBoost assist

4.5 Linear quadratic control of the VGT-EGR-eBoost system

4.5.1 Control objective and problem formulation

The control objective for the diesel engine air charge system is to regulate the amount of fresh air and oxygen concentration in the intake manifold to the desired values provided by the optimized engine calibration process. These calibration maps are generated based on an optimized trade-off between fuel economy and NOx emissions with the constraints on soot formation. The desired fresh air and oxygen concentration can be transferred to target values for air-fuel ratio and EGR fraction. If the fueling rate is known from driver's pedal position, the desired air-fuel ratio and EGR fraction can be converted to set points for boost pressure (p_2) and EGR mass flow rate ($\dot{m}_{\text{egr}}$), as shown in Figure 4.27.

Adding the eBoost and bypass valve to the VGT-EGR system changes the overall system characteristics. If eBoost compressor is running at low speed ($p_1 < p_0$), the flow through bypass valve is in the forward direction (see Figure 4.28a); if eBoost compressor is running at high speed ($p_1 > p_0$), the flow through bypass valve reverses (see Figure 4.28b). The pressure condition at compressor inlet separate the system behavior into two different dynamics. Therefore, it is suggested to design separated controllers for different scenarios (see

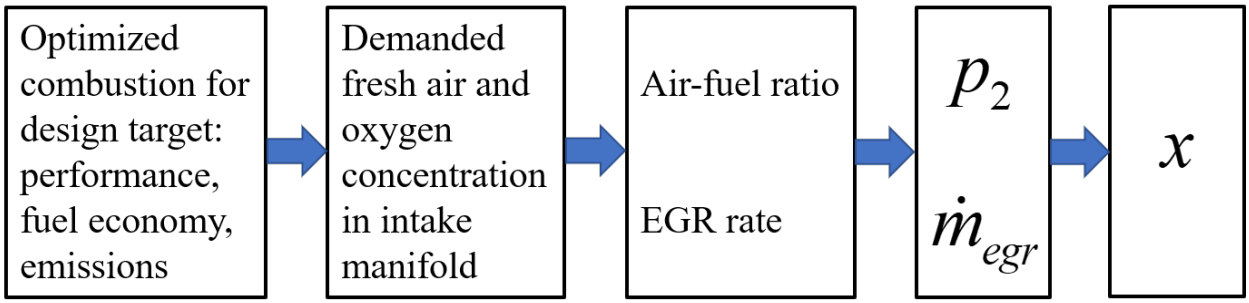

Figure 4.27: Set points for diesel engine air charge system control

Figure 4.29). In this study, only the feedback control for $p_1 > p_0$ is discussed.

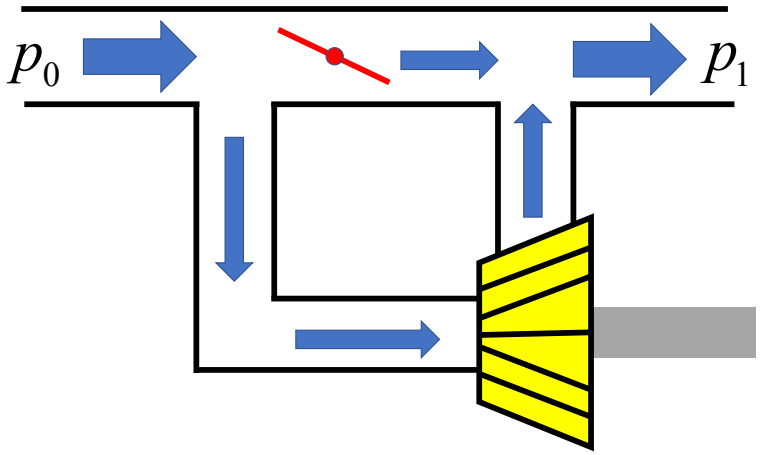

(a) Flow condition with $p_1 < p_0$

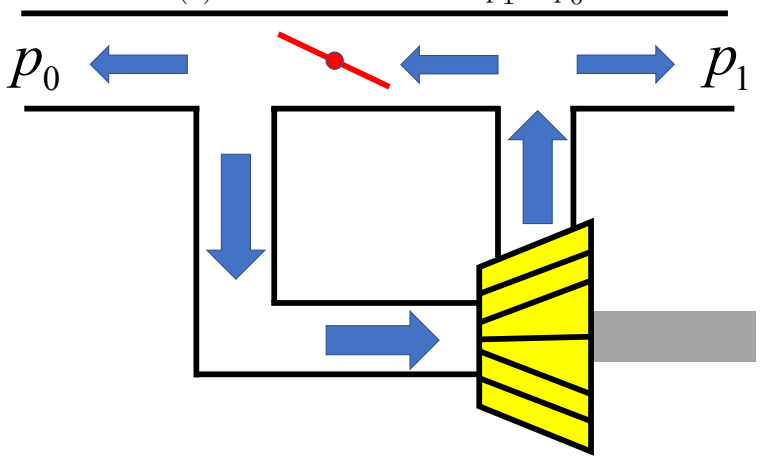

(b) Flow condition with $p_1 > p_0$

Figure 4.28: Flow conditions with different pressure ratio

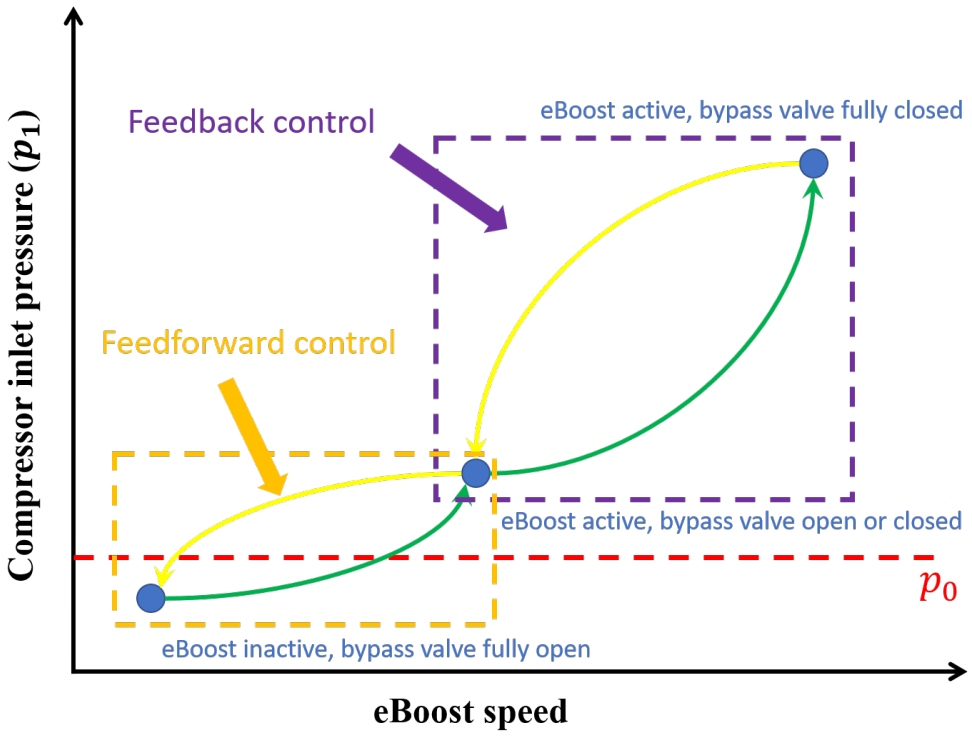

Figure 4.29: Set points for eBoost system

4.5.2 Linearization

Linearization of the full-order nonlinear model follows the standard process [86]. In summary, system states can be expressed as

$$x = [p_3 \quad p_2 \quad \omega_{tc} \quad \omega_e \quad p_1]^T \tag{4.36}$$

and input vector is

$$u = [u_{\text{vgt}} \quad u_{\text{egr}} \quad u_{eb} \quad u_{bp}]^T \tag{4.37}$$

Linearize the model about the equilibrium point x_0 and define the error vectors δx, δu, and δy as:

$$\begin{aligned} \delta x &= x - x_0 \\ \delta u &= u - u_0 \end{aligned} \tag{4.38}$$

Then the linearized state-space model can be written as

$$\delta \dot{x} = A\delta x + B\delta u \tag{4.39}$$

For instance, the linearized system matrices with engine speed of 1500 r/min, brake torque $\tau_e = 500$ N-m, eBoost power $u_{eb} = 2$ kW, and bypass valve opening $u_{bp} = 0.01$ are

$$A = \begin{bmatrix} -45.10 & 22.36 & -161.92 & -3.95 & 7.68 \\ 2.78 & -66.60 & 1099.94 & -42.87 & 83.32 \\ 0.07 & 0.28 & -5.73 & 0.21 & -0.40 \\ 0 & 0 & 0 & -2.97 & 0.04 \\ 0 & 131.73 & -2462.61 & 920.29 & -233.87 \end{bmatrix} \tag{4.40}$$

$$B = \begin{bmatrix} 7571446.13 & -7868122.06 & 0 & -11080.59 \\ 0 & 1719996.04 & 0 & -120213.39 \\ 557.87 & -6.38 \times 10^{-9} & 0 & 577.28 \\ 0 & 0 & 1612.56 & 0 \\ 0 & 0 & 0 & -549703.39 \end{bmatrix} \tag{4.41}$$

4.5.3 Linear quadratic regulator

A linear quadratic regulator (LQR) is designed to regulate the system near the equilibrium point with the cost function below.

$$J = \int_0^\infty \left[x^T(t) Q x(t) + u^T(t) R u(t) \right] dt \tag{4.42}$$

where

$$Q = \begin{bmatrix} 6.5078 & 0 & 0 & 0 & 0 \\ 0 & 5082.4 & 0 & 0 & 0 \\ 0 & 0 & 3457.5 & 0 & 0 \\ 0 & 0 & 0 & 9337.9 & 0 \\ 0 & 0 & 0 & 0 & 95.746 \end{bmatrix} \tag{4.43}$$

$$R = \begin{bmatrix} 5 & 0 & 0 & 0 \\ 0 & 10 & 0 & 0 \\ 0 & 0 & 0.01 & 0 \\ 0 & 0 & 0 & 10 \end{bmatrix} \tag{4.44}$$

The control gain K is calculated by solving algebraic Riccati equation

$$0 = PA + A^T P + Q - PBR^{-1}B^T P \tag{4.45}$$

A state feedback controller is considered in this case

$$u(t) = Kx(t) = -R^{-1}B^T Px(t) \tag{4.46}$$

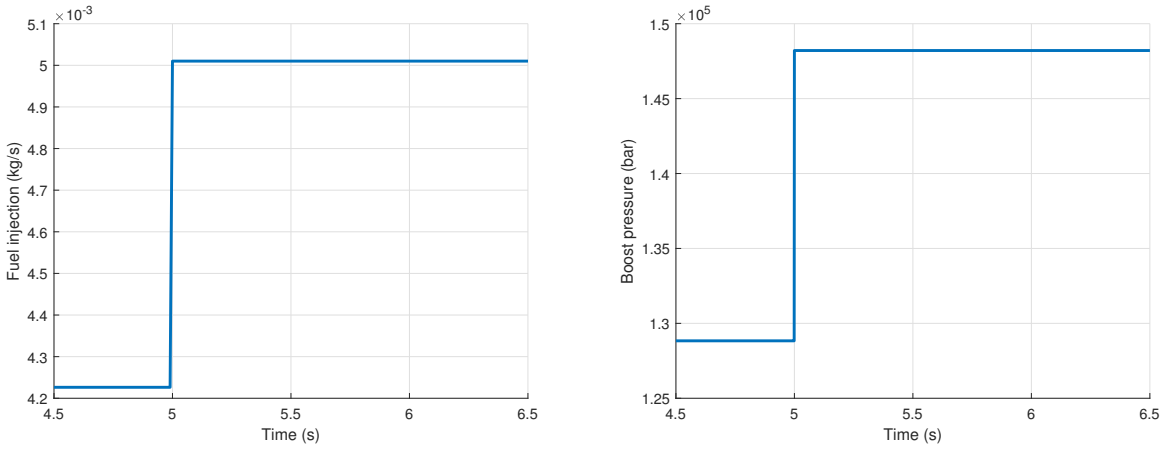

(a) Engine fuel injection (b) Target boost pressure

Figure 4.30: Step load test profile for engine operated at 1500 r/min

The designed LQR control has been implemented to the nonlinear model to study its performance. The set point is initially at 1500 r/min with 450 N-m. After 5 seconds, a load step with a new target torque of 550 N-m is applied (see Figure 4.30). The tracking results are shown in Figure 4.31. A separate PID control system (including 4 PID controller for all the actuators) has been developed for comparison. The objective is to demonstrate the capability of eBoost to improve transient boost tracking. With LQR controller, the VGT

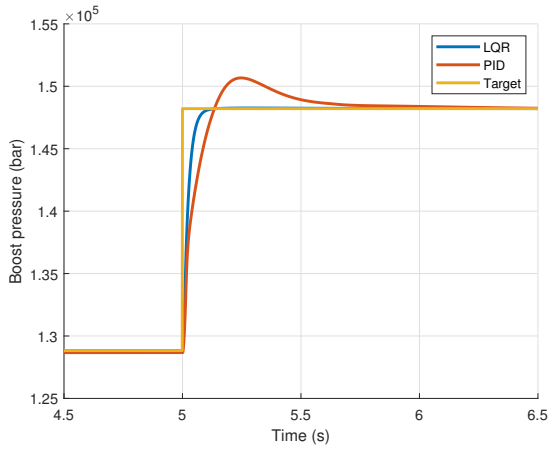

(a) Boost pressure tracking

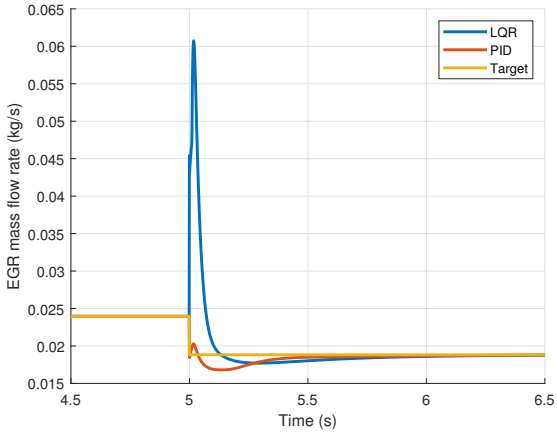

(b) EGR mass flow rate tracking

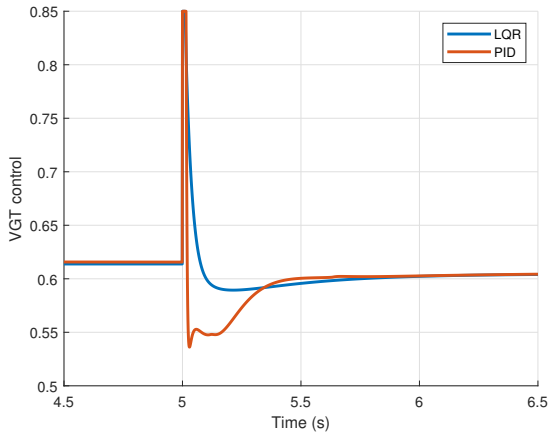

(c) VGT control

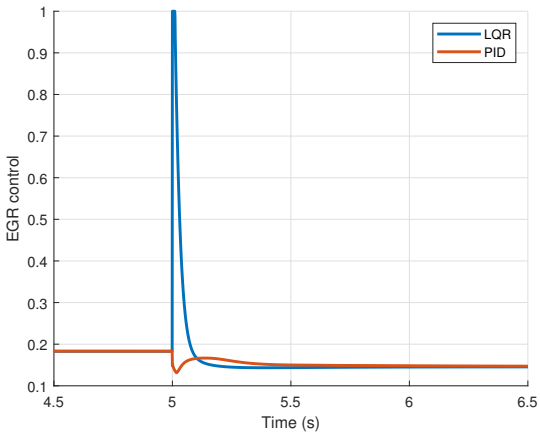

(d) EGR control

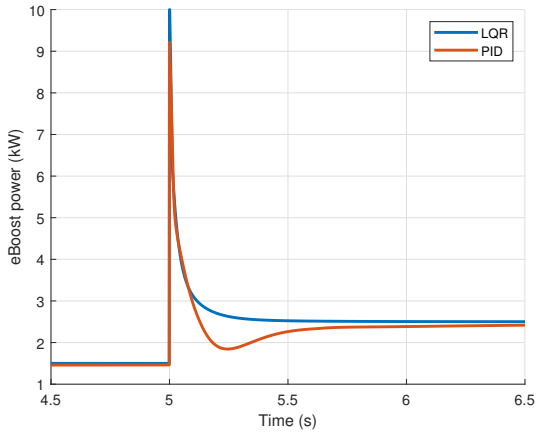

(e) eBoost power

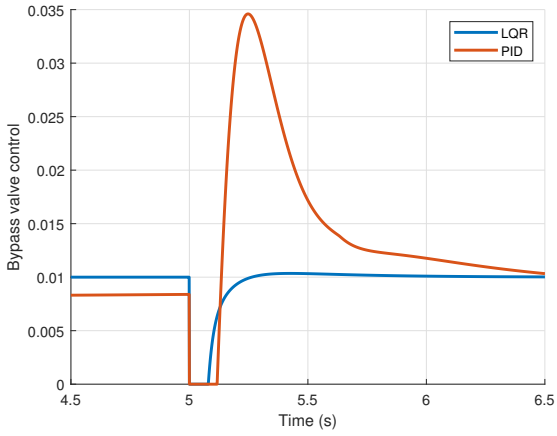

(f) Bypass valve control

Figure 4.31: Tracking performance

control is less aggressive and eBoost control is more aggressive, leading to much faster boost pressure response. The overshoot is also greatly reduced.

Due to the limitation of experimental setup, a full-order LQR controller is not possible because VGT and EGR valves are controlled by engine control module (ECM) while eBoost and bypass valve are controlled by the MotoTron module. Therefore, an alternative LQR controller is designed explicitly for eBoost (see Figure 4.32 for the control system architecture). The eBoost controller is designed based on the extended system including VGT and EGR controllers. A simulation of the eBoost controller at 2000 r/min with 250 N-m is performed and the results are shown in Figure 4.33. The fast rising of boost pressure with eBoost control is expected due to fast response of the electric motor.

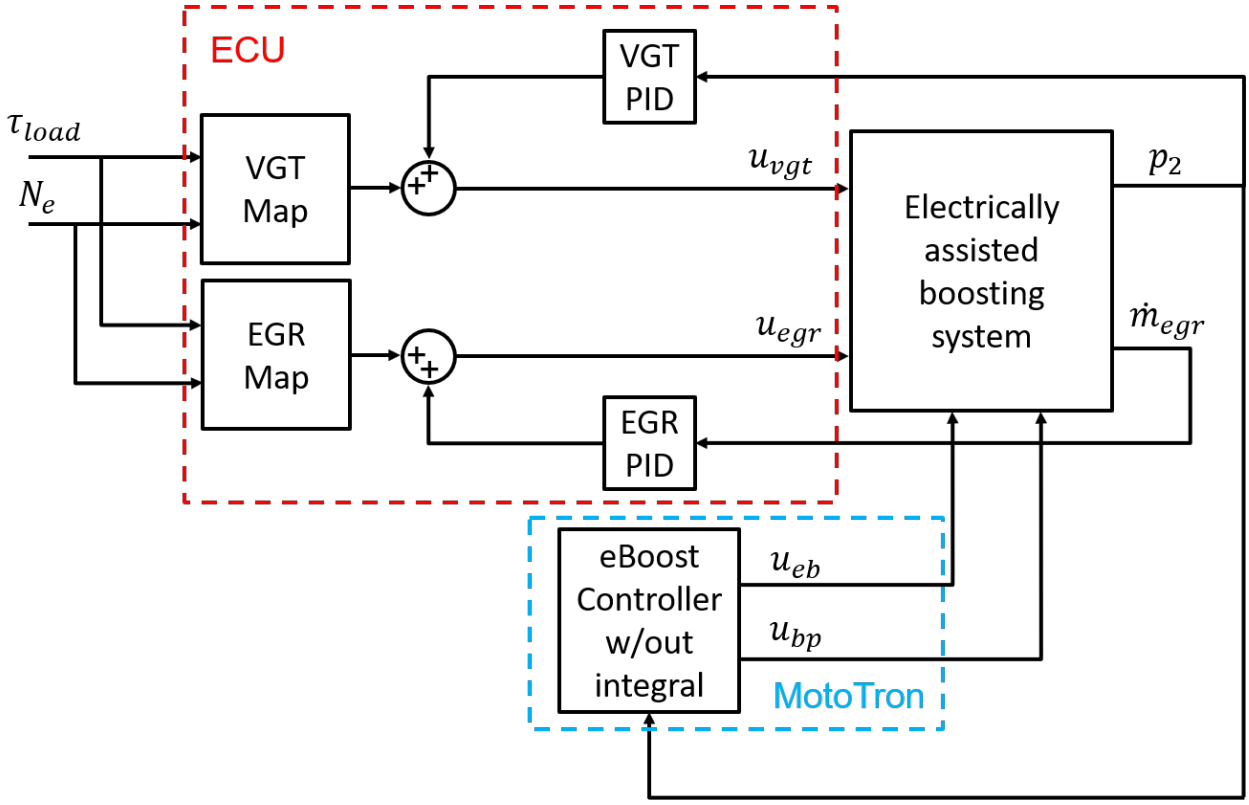

Figure 4.32: Control architecture for experimental implementation

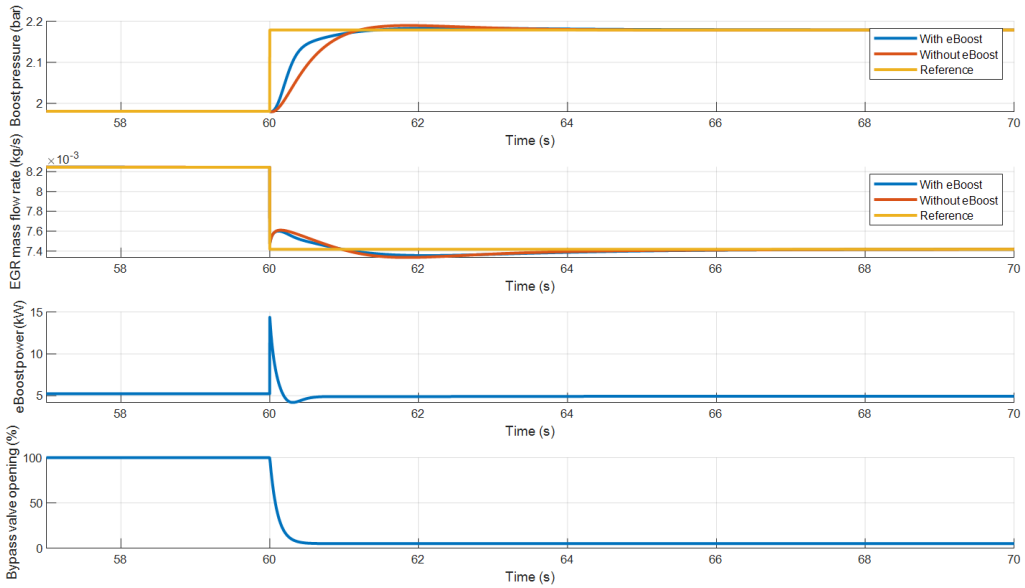

Figure 4.33: LQR for eBoost control

4.6 Experimental validation

4.6.1 Engine test setup

To validate the numerical study and control design, engine test has been performed at MSU Energy and Automotive Research Laboratory. The tested engine is provided by Ford Motor Company and the specifications are given in Table 4.13.

Table 4.13: Specifications of Ford diesel engine

Item	Value
Engine Type	Diesel, 4-Cycle
Configuration	V8
Displacement	6.7 L
Bore	99 mm
Stroke	108 mm
Compression Ratio	15.7:1
Combustion System	High Pressure Common Rail Direct Injection

The experiments are made possible by comprehensive instrumentation of the engine in-

stalled onto the MSU dynamometer. An alternating current (AC) dynamometer (dyno), coupled with engine crankshaft through a 1:2.75 gearbox, is used to supply and absorb engine power and maintain the engine speed. The dyno is capable of holding engine speed up to 3200 r/min. On the measurement side, Cylinder pressure is measured by 8 pressure transducers installed in each cylinder head. The signals pass through AVL charge amplifiers and are fed to an A&D Combustion Analysis System (CAS) for data visualization and recording. Regular pressure signals such as manifold absolute pressure (MAP), compressor inlet pressure, turbine outlet pressure, etc., are measured by Druck pressure sensors and fed into CAS. All the temperature signals such as ambient temperature, intake manifold temperature, coolant temperature, exhaust temperature, etc., are measured by thermal couples and the data are recorded by the dyno NI Data Acquisition (DAQ) system. On the control side, the engine comes with a production ECM whose calibration can be accessed and modified using ETAS INCA software through ES600.1 interface. The ECM outputs the control signals such as fuel injection quantity, injection timing, VGT position, EGR valve position based on current engine speed and pedal position. An open engine control unit (ECU), MotoTron, is used to sending control signals to peripheral devices, such as cooling tower, fuel pump, eBoost motor, and bypass valve. MotoTron module is also responsible to send the commanded pedal position signal to the ECM for the desired engine load. The control algorithm for the eBoost and bypass valve is programmed in MotoTron. To sync the recorded data across multiple devices, CAN communication is implemented among MotoTron module, NI DAQ, and INCA computer. In this way, data can be shared on the CAN bus and INCA software can be used for data recording. The layout of the engine test setup is shown in Figure 4.34.

4.6.2 Test bench validation and engine baseline

It is important to make sure all the sensors, actuators, controllers and communications work properly before performing any test. A testing matrix, shown in Figure 4.35, has been

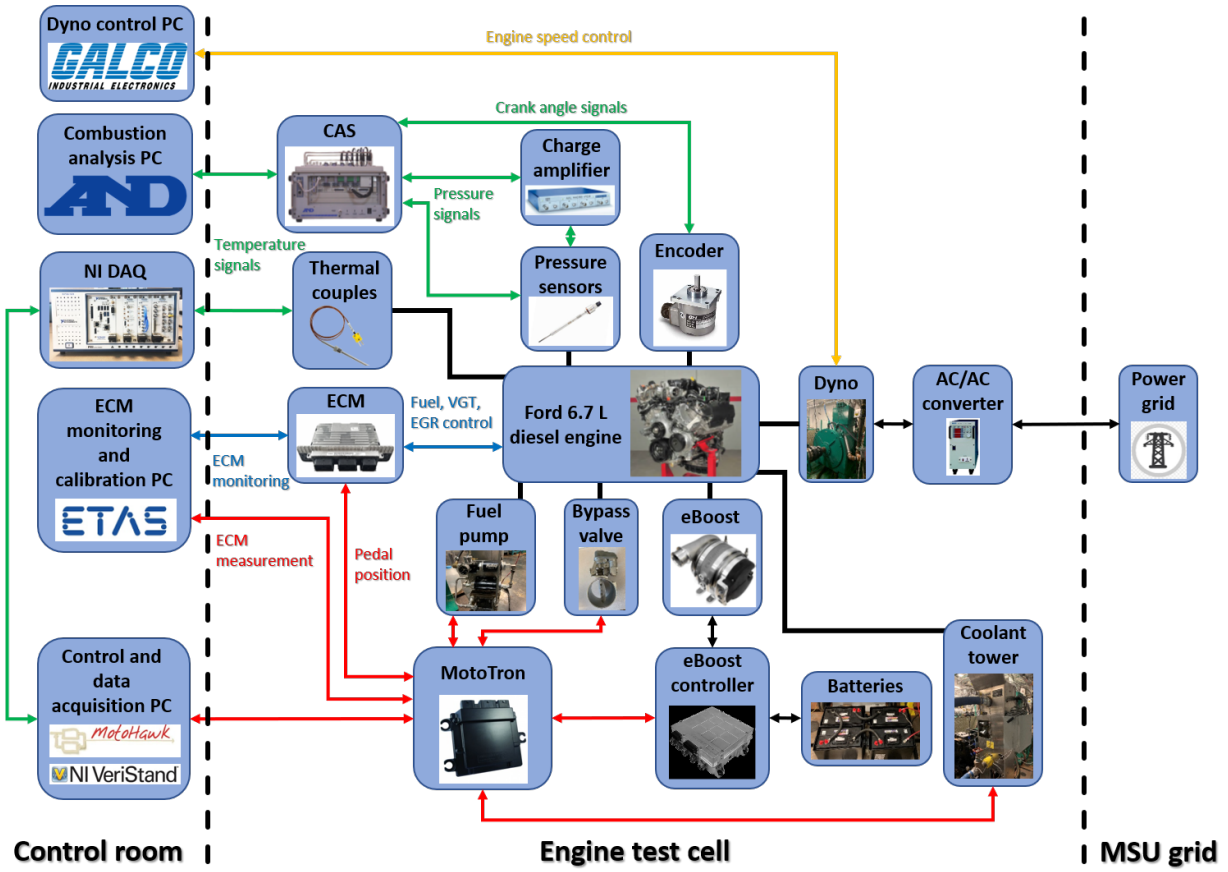

Figure 4.34: Engine test setup layout

generated based on simulation results. The selected range of engine speed and load is where eBoost activation is most desired. At each operational condition, the engine was run for 5 minutes after it reaches steady-state.

An important goal for the engine baseline test is to match the back pressure. Back pressure is the pressure at the turbine outlet, before the aftertreatment system. Back pressure is generally higher than ambient pressure due to the hydraulic resistance from the exhaust system (exhaust manifold, catalytic converter, muffler, and connecting pipes). Back pressure has a negative effect on engine efficiency, leading to decrement of engine power output. Since there is no production aftertreatment system in the current engine setup, the back pressure has to be simulated using a restriction plate. As shown in Figure 4.36, two plates with 15 0.5 inch holes are fixed to the exhaust pipe. By rotating the outer plate, the effective area

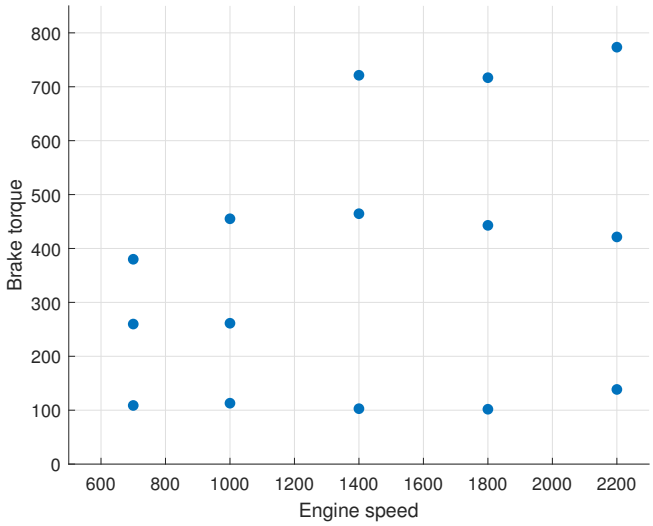

Figure 4.35: Engine test matrix

can be changed to match back pressure at different engine operating conditions. As shown in Figure 4.37, the back pressure is matched for all tested points, with less than 2% error.

Figure 4.36: Exhaust restriction plate

4.6.3 Steady-state validation

It has been shown that for mid speed and load conditions, eBoost is able to achieve up to 9% fuel efficiency improvement at steady state. This number could be overestimated

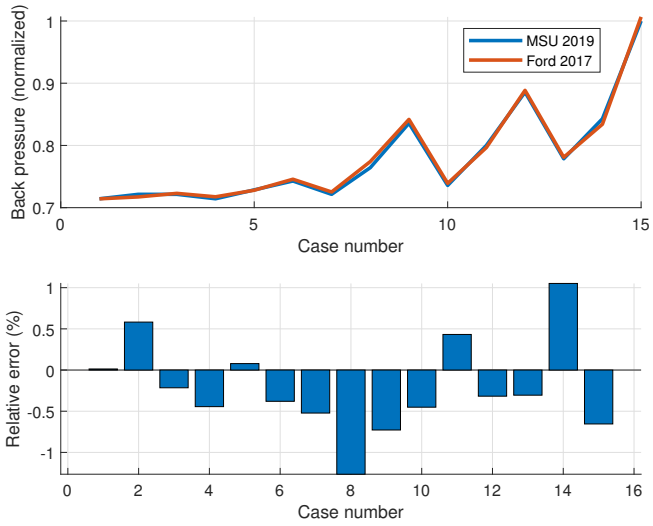

Figure 4.37: Back pressure matching

due to unmodeled losses in the physical system. In the engine test, eBoost speed was commanded through MotoTron and was controlled in a closed-loop by the eBoost controller. The commanded eBoost motor speed is based on simulation results with the best engine efficiency.

As expected, the activation of eBoost increases the boost energy. As the boost pressure is maintained at the same level, VGT position opening increases to reduce the turbocharger speed. This change leads to decreased exhaust manifold pressure. With the same engine boost pressure, decreased exhaust pressure reduces the pumping loss, which improves engine efficiency, as reflected by reduced fuel injection amount. Since the pressure drop is decreased from exhaust to intake manifold, EGR valve position is increased to maintain the EGR rate. It can be concluded that the general trend of all the parameters are reasonably validated. However, the improvement in fuel efficiency is not as high as predicted by the model. This could be due to three reasons. First, the model may not completely match the physical system because, eBoost, bypass and the connecting pipes models are not validated due to lack of data. Second, even if the model is accurate, fine tuning of the eBoost speed is still required to find the optimal operating conditions. Finally, the leakage of the bypass valve

could reduce the eBoost efficiency.

Tests have been performed for the entire engine test matrix. Detailed results with engine speed at 1000 r/min are presented as an example. Three load conditions are investigated: 113 N-m, 261.3 N-m, and 445.1 N-m. At each load condition, eBoost is maintained at different speed (20000 r/min to 55000 r/min) to provide different boost level. Note that for all conditions, the bypass air path is blocked with a solid scaled pipe to prevent any leakage caused by the bypass valve. At each engine load condition, the effective BSFC changes with eBoost speed effectively (see Figure 4.38a). There is an optimal eBoost speed for best BSFC. With properly tuned eBoost speed, the overall BSFC benefit can be improved compared to the baseline system (see Figure 4.38b)

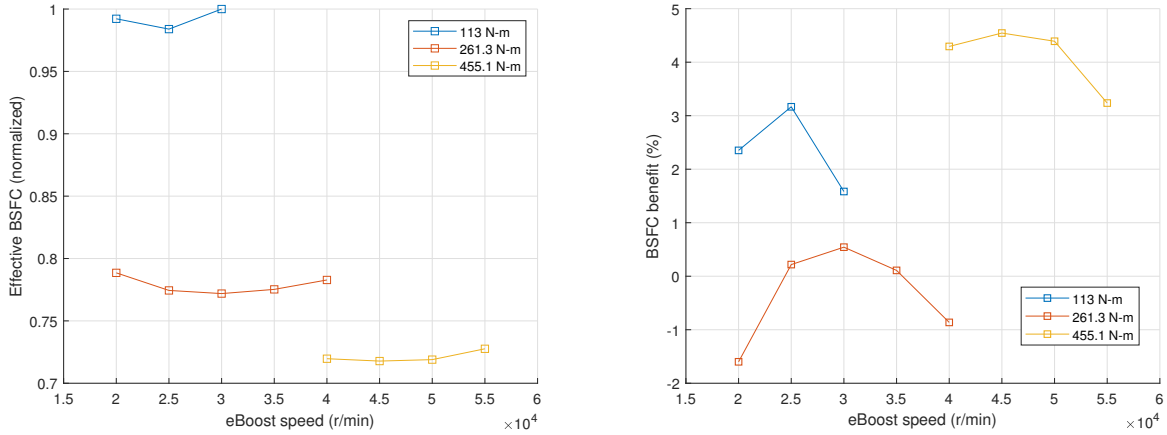

(a) Effective BSFC (b) BSFC benefit

Figure 4.38: BSFC improvement at 1000 r/min

The VGT and EGR valve positions are significantly changed with different eBoost speed (see Figure 4.39). With higher eBoost speed, VGT opening is increased to maintain the same boost pressure. EGR increased opening to maintain the same EGR mass flow rate. This observation is consistent with simulation results.

Considering the direct effect of eBoost, the compressor inlet pressure is investigated. As expected, the compressor inlet pressure is almost linear to eBoost speed (see Figure 4.40a).

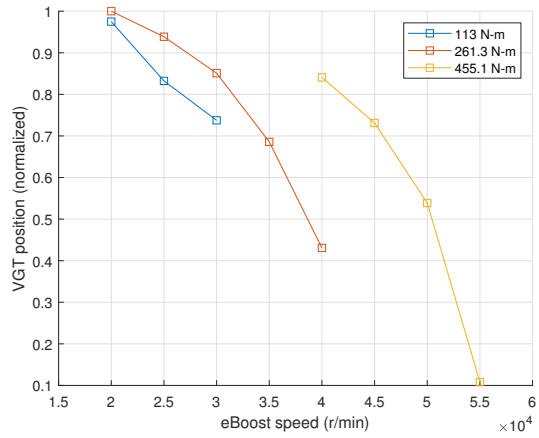

(a) VGT position

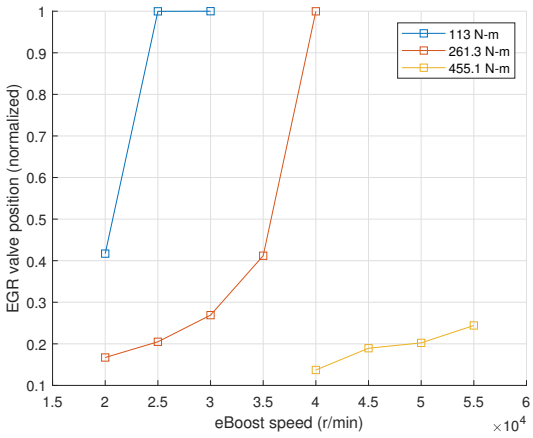

(b) EGR valve position

Figure 4.39: VGT and EGR operation with engine speed at 1000 r/min

The increase in compressor inlet pressure leads to increased VGT position and reduced turbocharger speed, as shown in Figure 4.40b.

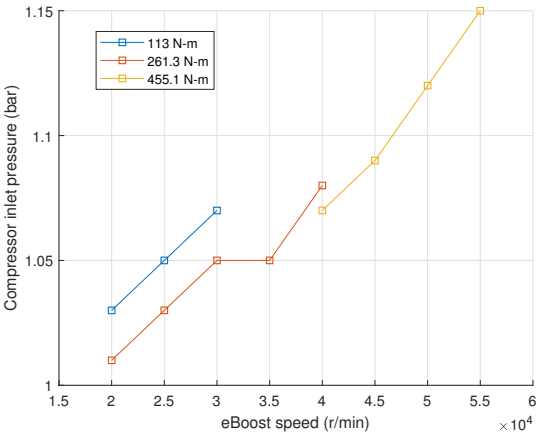

(a) Compressor inlet pressure

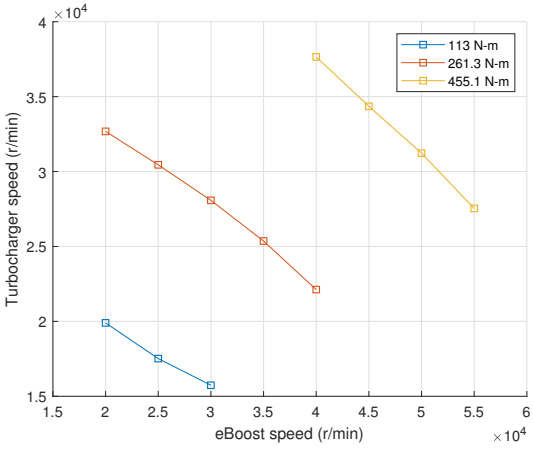

(b) Turbocharger speed

Figure 4.40: Compressor inlet pressure and turbocharger speed with engine speed at 1000 r/min

The reduction in exhaust manifold pressure is significant due to increased opening of VGT (see Figure 4.41a). The decreased exhaust manifold pressure is beneficial because of reduced pumping loss, leading to the reduced fuel consumption (see Figure 4.41b)

The BSFC benefits, predicted from simulation results, have been validated with test

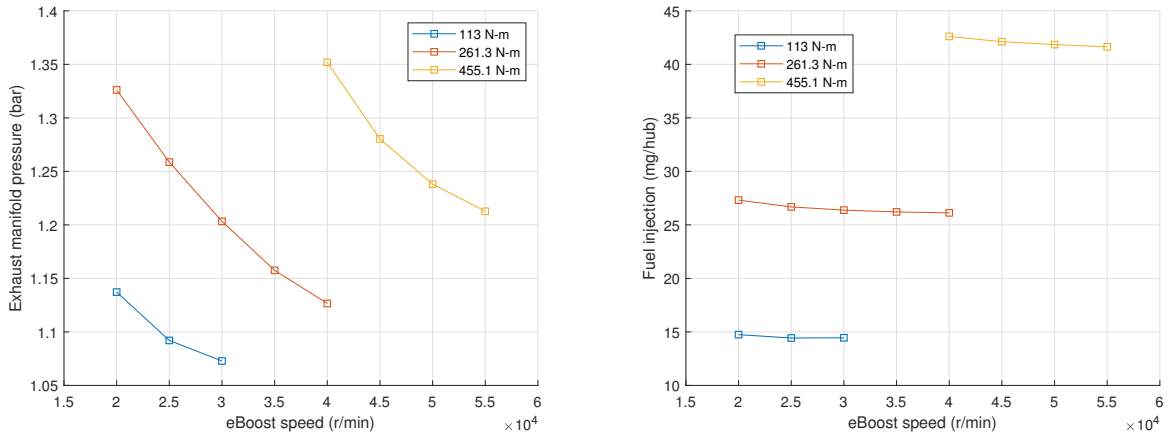

(a) Exhaust manifold pressure (b) Turbocharger speed

Figure 4.41: Exhaust manifold pressure and fuel injection with engine speed at 1000 r/min

results for three engine load conditions at 1000 r/min. Major engine parameters have been investigated and the trend is consistent with simulation results. In addition, the test results indicate that the standard EGR valve may not be suitable for bypass valve due to undesired leakage (see Figure 4.42).

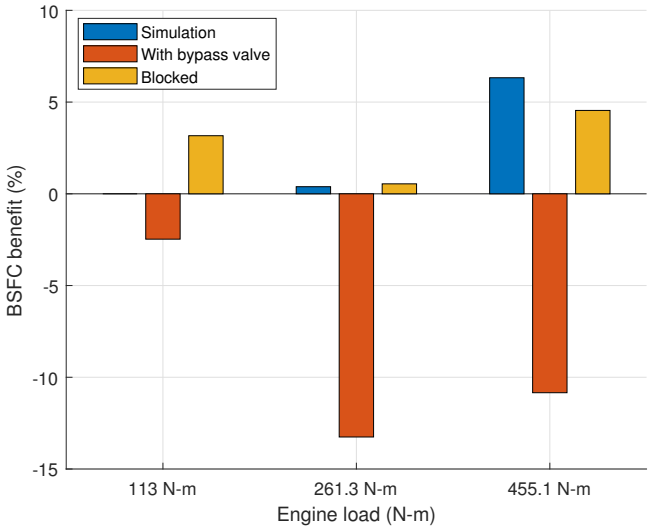

Figure 4.42: BSFC benefit from simulation and test results

Test results for the entire engine test matrix are shown in Figure 4.43. From the BSFC benefit map (Figure 4.43a) it is confirmed that steady-state fuel economy can be improved

by applying eBoost power. Greater improvement is achieved at lower speed conditions. The test results also provides guidelines for eBoost operation (see Figure 4.43b).

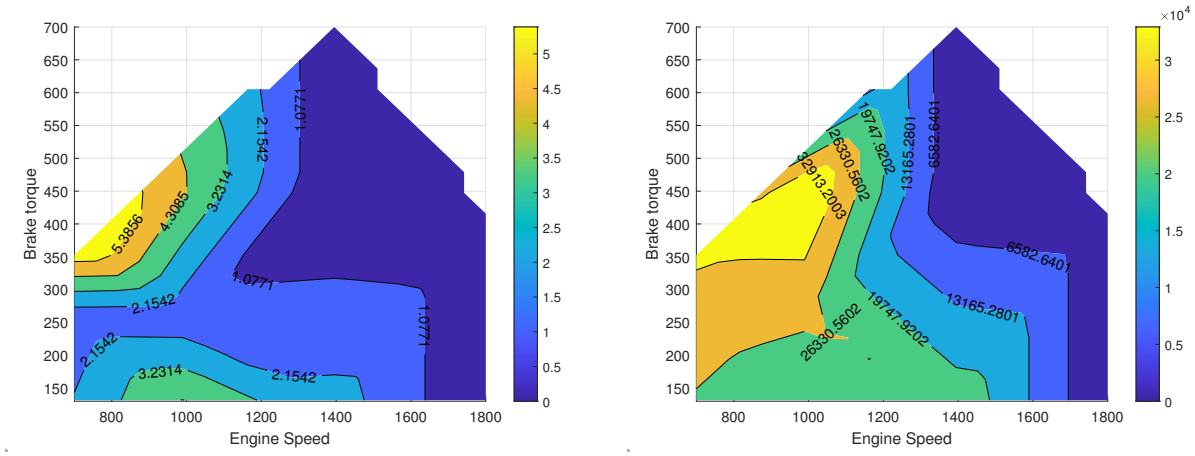

(a) BSFC benefit (%)

(b) eBoost speed (r/min)

Figure 4.43: Test results over the entire matrix

4.6.4 Transient validation

Transient tests were conducted for step load inputs at constant engine speed. The dyno maintained engine speed at 700 r/min, 1000 r/min, and 1400 r/min. With closed-loop control of pedal position, the torque can be maintained at the target initial level (100 N-m). Under the transient tests, the pedal position is stepped up to 100% for maximum brake torque. A step speed command is applied to the eBoost controller to enhance the boost pressure tracking. As a result, improvement in engine torque response is expected. Different levels of eBoost speed are commanded to investigate the effectiveness of eBoost. Baseline results (without eBoost) are included for comparison. The study is carried out with air block and with bypass valve to evaluate the loss of efficiency due to valve leakage.

As shown in Figure 4.44, with engine speed of 700 r/min, eBoost is able to slightly reduce response time, but significantly increase maximum torque. With engine speed of 1000 r/min, eBoost slightly increases maximum brake torque, but greatly reduces response

time (see Figure 4.45). With engine speed of 1400 r/min, eBoost reduces torque response time moderately, with no improvement in maximum torque (see Figure 4.46).

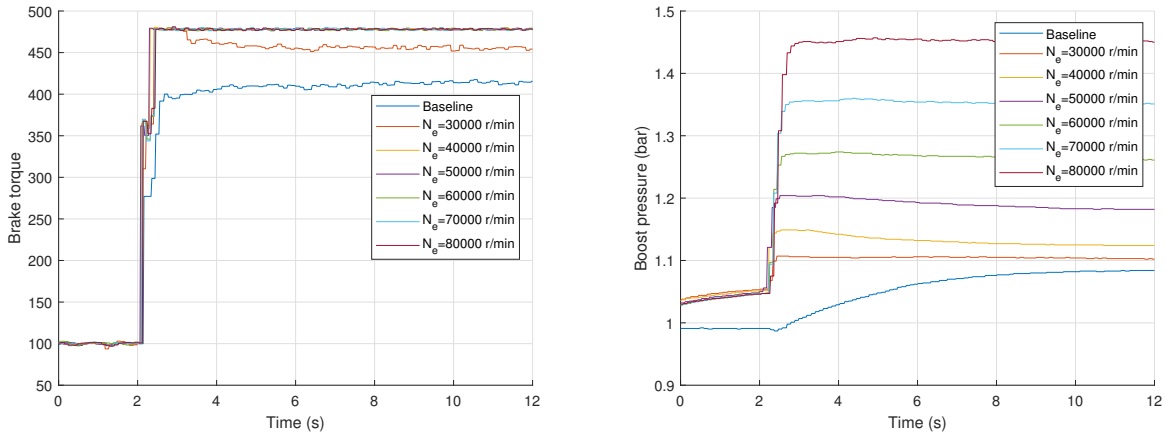

(a) Brake torque (b) Boost pressure

Figure 4.44: Transient response at 700 r/min with air block

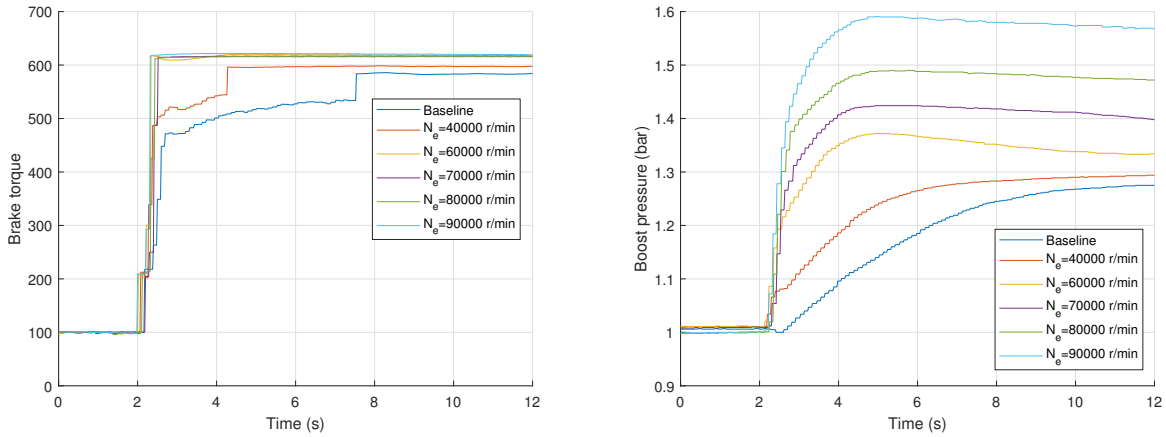

(a) Brake torque (b) Boost pressure

Figure 4.45: Transient response at 1000 r/min with air block

Testing results with bypass valve are shown in Figure 4.47, 4.48, and 4.49. Due to the fact that the bypass valve is not able to be fully closed, the loss of torque increase and response reduction is significant.

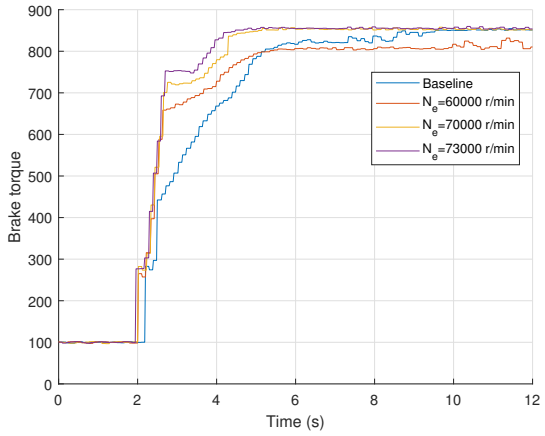

(a) Brake torque

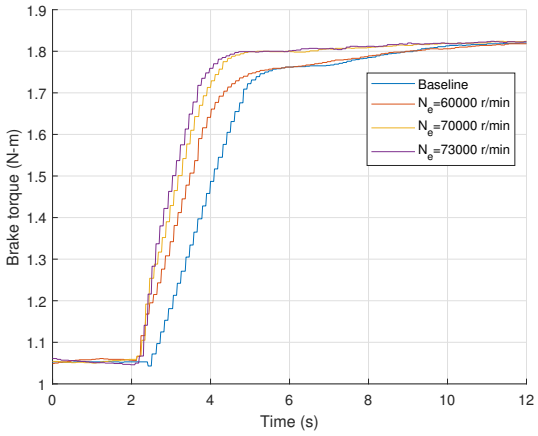

(b) Boost pressure

Figure 4.46: Transient response at 1400 r/min with air block

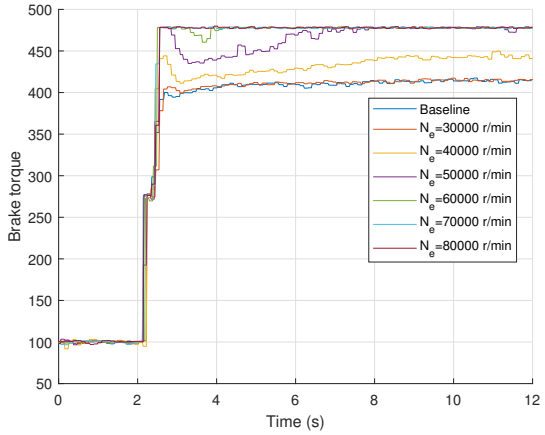

(a) Brake torque

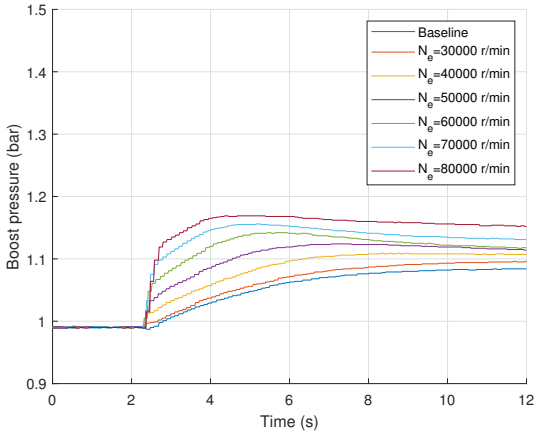

(b) Boost pressure

Figure 4.47: Transient response at 700 r/min with bypass valve

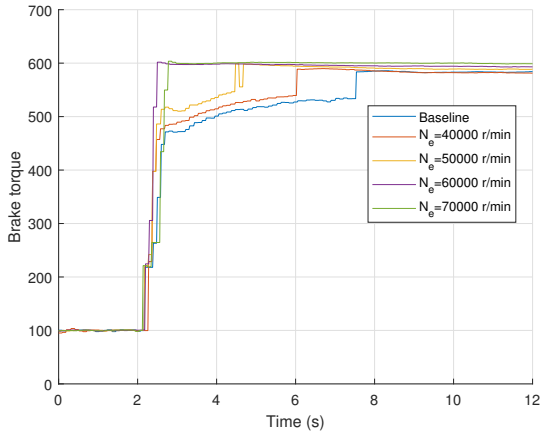

(a) Brake torque

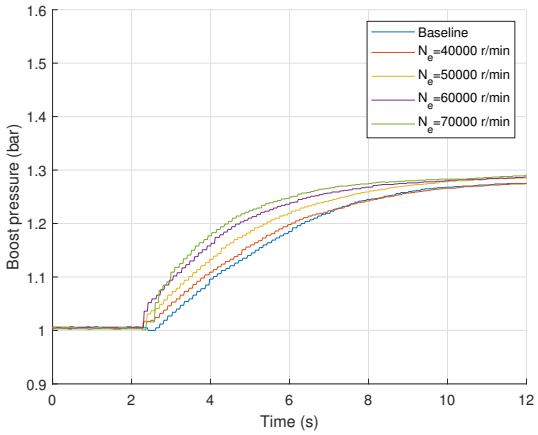

(b) Boost pressure

Figure 4.48: Transient response at 1000 r/min with bypass valve

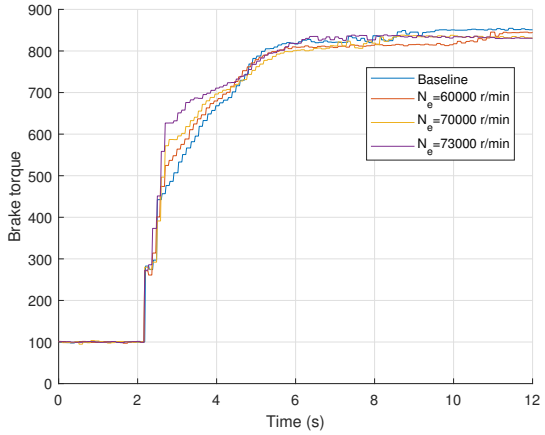

(a) Brake torque

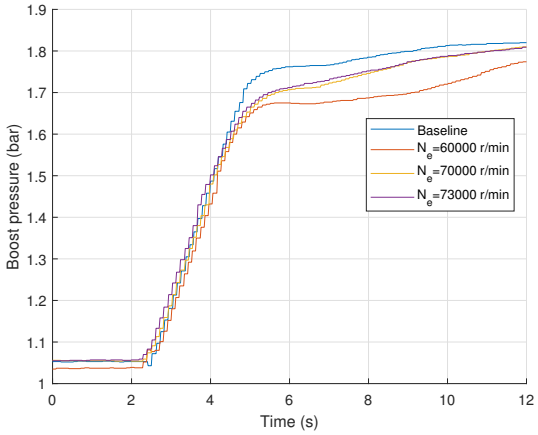

(b) Boost pressure

Figure 4.49: Transient response at 1400 r/min with bypass valve

4.7 Conclusions

The research on electrically assisted boosting system is still in early stage. In this chapter, the eBoost system was studied both numerically and experimentally. Some conclusions are summarized as follows:

1) A control-oriented engine air-path model has been developed for eBoost control. The model is validated on a component base with steady-state engine test data.

2) The performance improvement is first studied based on a GT-SUITE model with added eBoost. Both steady-state and transient performance is shown to be improved by properly controlling the eBoost speed.

3) Steady-state tests were performed to validate the simulation results. According to steady-state experimental data, the eBoost is able to improve the overall BSFC with the optimized eBoost speed command. The actual BSFC benefit is close to simulation results.

4) Transient test results confirm that the eBoost is able to reduce the response time of boost tracking.

5) To improve eBoost efficiency, the bypass valve cannot have any leak. As a result, a special bypass valve is needed.

CHAPTER 5

CONCLUSIONS AND FUTURE WORK

5.1 Conclusions

The conclusions of this dissertation can be summarized as follows:

1. A reaction-based modeling methodology has been formulated and implemented in diesel combustion model. The proposed model successfully predicts the in-cylinder pressure with acceptable error. The sensitivity study shows that only two calibration parameters are required to accurately calibrate the model. A calibration structure has been developed so that the number of required lookup tables is reduced significantly. The finalized model can be a potential candidate to replace the current Wiebe function.

2. A multi-zone modeling approach has been proposed specifically for diesel combustion. The developed model improves the prediction accuracy and eliminates the lookup tables, which are the main drawbacks of the single-zone model, especially with multiple fuel injections. The three-zone reaction-based model increases in computational time slightly but still can be implemented for model-based control and real-time simulations. It is a promising model for future combustion control.

3. A physics-based engine air charge system model with eBoost has been developed. The proposed model has been validated with steady-state engine test data and standard cycle data. The system behavior has been studied through 1-D simulations. It is found that eBoost improves both steady-state and transient performance. A complete test bench for turbocharged diesel engine has been set up. Baseline tests have been performed to validate the instrumentation and generate baseline parameters. Tests have been performed under different operating conditions to validate the eBoost's capability of improving steady-state fuel economy and transient response.

5.2 Recommendations for future work

The following future work is recommended for the reaction-based modeling and study on the eBoost system:

1. Future work for reaction-based modeling includes replacing the two-step mechanism with a more detailed mechanism that improves chemical delay model. A systematic method, that determines the optimal number of zones and/or reaction steps depending on the application, is an open problem to be solved.

2. For eBoost operations, it is possible for the eBoost to create too much boost, causing the main compressor to operate as a turbine (upstream pressure greater than downstream pressure). This could happen at the beginning of each tip-in process. An accurate model for this process is important to understand the behavior of eBoost under transient operations as well as improve eBoost control.

3. Model predictive control is a promising method for eBoost system because it handles control constraints very well. The challenge is to develop an accurate system model and develop the controller implementable for real-time control.

BIBLIOGRAPHY

BIBLIOGRAPHY

[1] A. Santos, N. McGuckin, H. Y. Nakamoto, D. Gray, and S. Liss, "Summary of travel trends: 2009 national household travel survey," tech. rep., Federal Highway Administration, 2011.

[2] A. Sieminski *et al.*, "International energy outlook," *Energy Information Administration (EIA)*, vol. 18, 2014.

[3] T. V. Johnson, "Review of CO_2 emissions and technologies in the road transportation sector," *SAE International Journal of Engines*, vol. 3, no. 1, pp. 1079–1098, 2010.

[4] M. Adams and A. Lükewille, *The European Environment-state and outlook 2010*. European Environment Agency, 2010.

[5] F. Payri, J. M. Luján, C. Guardiola, and B. Pla, "A challenging future for the ic engine: New technologies and the control role," *Oil & Gas Science and Technology–Revue d'IFP Energies nouvelles*, vol. 70, no. 1, pp. 15–30, 2015.

[6] A. G. Stefanopoulou, I. Kolmanovsky, and J. S. Freudenberg, "Control of variable geometry turbocharged diesel engines for reduced emissions," *IEEE transactions on control systems technology*, vol. 8, no. 4, pp. 733–745, 2000.

[7] J. Ghojel, "Review of the development and applications of the wiebe function: a tribute to the contribution of ivan wiebe to engine research," *International Journal of Engine Research*, vol. 11, no. 4, pp. 297–312, 2010.

[8] E. Toulson, C. M. Allen, D. J. Miller, J. McFarlane, H. J. Schock, and T. Lee, "Modeling the autoignition of fuel blends with a multistep model," *Energy & Fuels*, vol. 25, no. 2, pp. 632–639, 2011.

[9] E. Toulson, C. M. Allen, D. J. Miller, and T. Lee, "Modeling the auto-ignition of oxygenated fuels using a multistep model," *Energy & Fuels*, vol. 24, no. 2, pp. 888–896, 2009.

[10] Y. Ra and R. D. Reitz, "A reduced chemical kinetic model for ic engine combustion simulations with primary reference fuels," *Combustion and Flame*, vol. 155, no. 4, pp. 713–738, 2008.

[11] G. Micklow and W. Gong, "A multistage combustion model and soot formation model for direct-injection diesel engines," *Proceedings of the Institution of Mechanical Engineers, Part D: Journal of Automobile Engineering*, vol. 216, no. 6, pp. 495–504, 2002.

[12] V. Tandra and N. Srivastava, "A control-oriented two zone thermo-kinetic model of a single cylinder hcci engine," in *ASME 2008 International Design Engineering Technical Conferences and Computers and Information in Engineering Conference*, pp. 825–834, American Society of Mechanical Engineers, 2008.

[13] S. R. Turns *et al.*, *An introduction to combustion*, vol. 287. McGraw-hill New York, 1996.

[14] G. M. Shaver, J. C. Gerdes, P. Jain, P. Caton, and C. Edwards, "Modeling for control of hcci engines," in *American Control Conference, 2003. Proceedings of the 2003*, vol. 1, pp. 749–754, IEEE, 2003.

[15] C. K. Westbrook and F. L. Dryer, "Simplified reaction mechanisms for the oxidation of hydrocarbon fuels in flames," *Combustion science and technology*, vol. 27, no. 1-2, pp. 31–43, 1981.

[16] B. Franzelli, E. Riber, M. Sanjosé, and T. Poinsot, "A two-step chemical scheme for kerosene–air premixed flames," *Combustion and Flame*, vol. 157, no. 7, pp. 1364–1373, 2010.

[17] W. Jones and R. Lindstedt, "Global reaction schemes for hydrocarbon combustion," *Combustion and flame*, vol. 73, no. 3, pp. 233–249, 1988.

[18] D. Hautman, F. Dryer, K. Schug, and I. Glassman, "A multiple-step overall kinetic mechanism for the oxidation of hydrocarbons," *Combustion Science and Technology*, vol. 25, no. 5-6, pp. 219–235, 1981.

[19] D. Hamby, "A review of techniques for parameter sensitivity analysis of environmental models," *Environmental monitoring and assessment*, vol. 32, no. 2, pp. 135–154, 1994.

[20] T. F. Coleman and Y. Li, "An interior trust region approach for nonlinear minimization subject to bounds," *SIAM Journal on optimization*, vol. 6, no. 2, pp. 418–445, 1996.

[21] L. Zhang, "A study of pilot injection in a di diesel engine," tech. rep., SAE Technical Paper, 1999.

[22] X. Yang and G. G. Zhu, "A mixed mean-value and crank-based model of a dual-stage turbocharged si engine for hardware-in-the-loop simulation," in *American Control Conference (ACC), 2010*, pp. 3791–3796, IEEE, 2010.

[23] X. Yang and G. G. Zhu, "A control-oriented hybrid combustion model of a homogeneous charge compression ignition capable spark ignition engine," *Proceedings of the Institution of Mechanical Engineers, Part D: Journal of Automobile Engineering*, vol. 226, no. 10, pp. 1380–1395, 2012.

[24] S. Zhang, G. Zhu, and Z. Sun, "A control-oriented charge mixing and two-zone hcci combustion model," *IEEE transactions on vehicular technology*, vol. 63, no. 3, pp. 1079–1090, 2014.

[25] R. Finesso and E. Spessa, "Ignition delay prediction of multiple injections in diesel engines," *Fuel*, vol. 119, pp. 170–190, 2014.

[26] S. Zhang, G. G. Zhu, Y. Yoon, and Z. Sun, "A control oriented charge mixing and hcci combustion model for internal combustion engines," in *ASME 2012 5th Annual Dynamic Systems and Control Conference joint with the JSME 2012 11th Motion and Vibration Conference*, pp. 321–327, American Society of Mechanical Engineers, 2012.

[27] C. Barba, C. Burkhardt, K. Boulouchos, and M. Bargende, "A phenomenological combustion model for heat release rate prediction in high-speed di diesel engines with common rail injection," tech. rep., SAE Technical Paper, 2000.

[28] Y. Men, I. Haskara, Y.-Y. Wang, C.-F. Chang, and G. G. Zhu, "Model-based calibration of the reaction-based diesel combustion dynamics," in *American Control Conference (ACC), 2017*, pp. 4735–4740, IEEE, 2017.

[29] I. Arsie, F. Di Genova, A. Mogavero, C. Pianese, G. Rizzo, A. Caraceni, P. Cioffi, and G. Flauti, "Multi-zone predictive modeling of common rail multi-injection diesel engines," tech. rep., SAE Technical Paper, 2006.

[30] K. Zhang, M. Xu, J. Wei, Y. Cui, and K. Deng, "Phenomenological two-phase multi-zone combustion model for direct-injection diesel engines," *International Journal of Automotive Technology*, vol. 17, no. 5, pp. 895–907, 2016.

[31] M. Ates, R. D. Matthews, and M. J. Hall, "A full-cycle multi-zone quasi-dimensional direct injection diesel engine model based on a conceptual model developed from imaging experiments," tech. rep., SAE Technical Paper, 2017.

[32] A. P. Dobos and A. T. Kirkpatrick, "Quasidimensional modeling of diesel combustion using detailed chemical kinetics," *Journal of Engineering for Gas Turbines and Power*, vol. 139, no. 8, p. 081502, 2017.

[33] E. Neshat, D. Honnery, and R. K. Saray, "Multi-zone model for diesel engine simulation based on chemical kinetics mechanism," *Applied Thermal Engineering*, no. 121, pp. 351–360, 2017.

[34] E. Neshat and R. K. Saray, "Development of a new multi zone model for prediction of hcci (homogenous charge compression ignition) engine combustion, performance and emission characteristics," *Energy*, vol. 73, pp. 325–339, 2014.

[35] E. Neshat, R. K. Saray, and V. Hosseini, "Effect of reformer gas blending on homogeneous charge compression ignition combustion of primary reference fuels using multi zone model and semi detailed chemical-kinetic mechanism," *Applied Energy*, vol. 179, pp. 463–478, 2016.

[36] M. Bissoli, A. Frassoldati, A. Cuoci, E. Ranzi, M. Mehl, and T. Faravelli, "A new predictive multi-zone model for hcci engine combustion," *Applied Energy*, vol. 178, pp. 826–843, 2016.

[37] M. Baratta, A. E. Catania, A. Ferrari, R. Finesso, and E. Spessa, "Premixed-diffusive multizone model for combustion diagnostics in conventional and pcci diesel engines," *Journal of Engineering for Gas Turbines and Power*, vol. 133, no. 10, p. 102801, 2011.

[38] S. S. Goldsborough, C. Banyon, and G. Mittal, "A computationally efficient, physics-based model for simulating heat loss during compression and the delay period in rcm experiments," *Combustion and Flame*, vol. 159, no. 12, pp. 3476–3492, 2012.

[39] D. Wilson and C. Allen, "Application of a multi-zone model for the prediction of species concentrations in rapid compression machine experiments," *Combustion and Flame*, vol. 171, pp. 185–197, 2016.

[40] S. Rajkumar and J. Thangaraja, "Multi-zone phenomenological combustion modeling of biodiesel fueled compression ignition engine," *International Journal of Engine Research*, vol. 17, no. 9, pp. 934–956, 2016.

[41] Y. Yamasaki, R. Ikemura, M. Takahashi, F. Shimizu, and S. Kaneko, "Simple combustion model for a diesel engine with multiple fuel injections," *International Journal of Engine Research*, vol. 20, no. 2, pp. 167–180, 2019.

[42] T. Katrašnik, "An advanced real-time capable mixture controlled combustion model," *Energy*, vol. 95, pp. 393–403, 2016.

[43] S. Rajkumar, P. S. Mehta, and S. Bakshi, "Phenomenological modeling of combustion and emissions for multiple-injection common rail direct injection engines," *International Journal of Engine Research*, vol. 13, no. 4, pp. 307–322, 2012.

[44] B. Jochim, M. Korkmaz, and H. Pitsch, "Scalar dissipation rate based multi-zone model for early-injected and conventional diesel engine combustion," *Combustion and Flame*, vol. 175, pp. 138–154, 2017.

[45] Y. Men and G. G. Zhu, "A multi-zone reaction-based diesel combustion model for model-based control," in *ASME 2017 Dynamic Systems and Control Conference*, pp. V003T27A003–V003T27A003, American Society of Mechanical Engineers, 2017.

[46] G. Woschni, "A universally applicable equation for the instantaneous heat transfer coefficient in the internal combustion engine," tech. rep., SAE Technical paper, 1967.

[47] Y. Men, I. Haskara, Y.-Y. Wang, C.-F. Chang, and G. Zhu, "Model-based calibration of reaction-based diesel combustion dynamics," *Proceedings of the Institution of Mechanical Engineers, Part D: Journal of Automobile Engineering*, vol. 232, no. 12, pp. 1611–1622, 2018.

[48] J. F. Moody, "Variable geometry turbocharging with electronic control," tech. rep., SAE Technical Paper, 1986.

[49] J. G. Hawley, F. Wallace, A. Cox, R. Horrocks, and G. Bird, "Reduction of steady state nox levels from an automotive diesel engine using optimised vgt/egr schedules," tech. rep., SAE Technical Paper, 1999.

[50] H. Sun, D. Hanna, P. Niessen, B. Fulton, L. Hu, E. W. Curtis, and J. Yi, "Experimental evaluation of advanced turbocharger performance on a light duty diesel engine," *SAE International Journal of Engines*, vol. 6, no. 2013-01-0920, pp. 788–796, 2013.

[51] I. Kolmanovsky, P. Morall, M. Van Nieuwstadt, and A. Stefanopoulou, "Issues in modelling and control of intake flow in variable geometry turbocharged engines," *Chapman and Hall CRC research notes in mathematics*, pp. 436–445, 1999.

[52] D. A. Singer, "Comparison of a supercharger vs. a turbocharger in a small displacement gasoline engine application," tech. rep., SAE Technical Paper, 1985.

[53] M. Jankovic and I. Kolmanovsky, "Constructive lyapunov control design for turbocharged diesel engines," *IEEE Transactions on Control Systems Technology*, vol. 8, no. 2, pp. 288–299, 2000.

[54] M. Ammann, N. P. Fekete, L. Guzzella, and A. H. Glattfelder, "Model-based control of the vgt and egr in a turbocharged common-rail diesel engine: theory and passenger car implementation," *SAE transactions*, pp. 527–538, 2003.

[55] T. Dong, F. Zhang, B. Liu, and X. An, "Model-based state feedback controller design for a turbocharged diesel engine with an egr system," *Energies*, vol. 8, no. 6, pp. 5018–5039, 2015.

[56] H. Xie, K. Song, S. Yang, J. Tatsumi, Q. Zheng, H. Zhang, and Z. Gao, "On decoupling control of the vgt-egr system in diesel engines: a new framework," *IEEE Transactions on Control Systems Technology*, vol. 24, no. 5, pp. 1788–1796, 2016.

[57] S. Timoney, "Turbochargers with hydraulic assist," tech. rep., SAE Technical Paper, 1983.

[58] S. G. Timoney, "A review of ideas for improving transient response in vehicle diesel engines," tech. rep., SAE Technical Paper, 1986.

[59] D. Kapich, "Hydraulic turbine-pump hybrid turbocharger system," July 19 2012. US Patent App. 12/930,870.

[60] H. H. Sun, D. R. Hanna, M. Levin, E. W. Curtis, and F. Z. Shaikh, "Regenerative assisted turbocharger system," Dec. 23 2014. US Patent 8,915,082.

[61] T. Zeng, D. Upadhyay, H. Sun, E. Curtis, and G. G. Zhu, "Regenerative hydraulic assisted turbocharger," *Journal of Engineering for Gas Turbines and Power*, vol. 140, no. 10, p. 102602, 2018.

[62] T. Zeng and G. Zhu, "Modeling and control of a diesel engine with regenerative hydraulic-assisted turbocharger," *Journal of Engineering for Gas Turbines and Power*, vol. 141, no. 5, p. 051004, 2019.

[63] J. Panting, K. Pullen, and R. Martinez-Botas, "Turbocharger motor-generator for improvement of transient performance in an internal combustion engine," *Proceedings of the Institution of Mechanical Engineers, Part D: Journal of Automobile Engineering*, vol. 215, no. 3, pp. 369–383, 2001.

[64] T. Katrašnik, S. Rodman, F. Trenc, A. Hribernik, and V. Medica, "Improvement of the dynamic characteristic of an automotive engine by a turbocharger assisted by an electric motor," *Journal of engineering for gas turbines and power*, vol. 125, no. 2, pp. 590–595, 2003.

[65] T. Katrašnik, F. Trenc, V. Medica, and S. Markič, "An analysis of turbocharged diesel engine dynamic response improvement by electric assisting systems," *Journal of engineering for gas turbines and power*, vol. 127, no. 4, pp. 918–926, 2005.

[66] B. C. Glenn, D. Upadhyay, and G. N. Washington, "Control design of electrically assisted boosting systems for diesel powertrain applications," *IEEE Transactions on Control Systems Technology*, vol. 18, no. 4, pp. 769–778, 2010.

[67] A. L. Carpenter, T. L. Beechner, B. E. Tews, and P. E. Yelvington, "Hybrid-electric turbocharger and high-speed sic variable-frequency drive using sensorless control algorithm," in *ASME 2017 Internal Combustion Engine Division Fall Technical Conference*, pp. V002T05A001–V002T05A001, American Society of Mechanical Engineers, 2017.

[68] P. Dimitriou, R. Burke, Q. Zhang, C. Copeland, and H. Stoffels, "Electric turbocharging for energy regeneration and increased efficiency at real driving conditions," *Applied Sciences*, vol. 7, no. 4, p. 350, 2017.

[69] K. Song, D. Upadhyay, and H. Xie, "Control of diesel engines with electrically assisted turbocharging through an extended state observer based nonlinear mpc," *Proceedings of the Institution of Mechanical Engineers, Part D: Journal of Automobile Engineering*, p. 0954407017744145, 2017.

[70] K. Song, D. Upadhyay, and H. Xie, "An assessment of performance trade-offs in diesel engines equipped with regenerative electrically assisted turbochargers," *International Journal of Engine Research*, p. 1468087418762170, 2018.

[71] A. Lefebvre and S. Guilain, "Transient response of a turbocharged si engine with an electrical boost pressure supply," *SAE transactions*, pp. 1310–1318, 2003.

[72] Y. Liu, R. Vijayakumar, and R. Burke, "Analysis of the opportunities and trade-offs for an 48v electrified air path," in *ASME 2018 Internal Combustion Engine Division Fall Technical Conference*, pp. V002T05A007–V002T05A007, American Society of Mechanical Engineers, 2018.

[73] G. Tavčar, F. Bizjan, and T. Katrašnik, "Methods for improving transient response of diesel engines–influences of different electrically assisted turbocharging topologies," *Proceedings of the Institution of Mechanical Engineers, Part D: Journal of Automobile Engineering*, vol. 225, no. 9, pp. 1167–1185, 2011.

[74] A. Darlington, D. Cieslar, N. Collings, and K. Glover, "Assessing boost-assist options for turbocharged engines using 1-d engine simulation and model predictive control," tech. rep., SAE Technical Paper, 2012.

[75] L. Eriksson, T. Lindell, O. Leufven, and A. Thomasson, "Scalable component-based modeling for optimizing engines with supercharging, e-boost and turbocompound concepts," *SAE International Journal of Engines*, vol. 5, no. 2012-01-0713, pp. 579–595, 2012.

[76] R. D. Burke, "A numerical study of the benefits of electrically assisted boosting systems," *Journal of Engineering for Gas Turbines and Power*, vol. 138, no. 9, p. 092808, 2016.

[77] W. Lee, E. Schubert, Y. Li, S. Li, D. Bobba, and B. Sarlioglu, "Overview of electric turbocharger and supercharger for downsized internal combustion engines," *IEEE Transactions on Transportation Electrification*, vol. 3, no. 1, pp. 36–47, 2017.

[78] D. Zhao, E. Winward, Z. Yang, R. Stobart, B. Mason, and T. Steffen, "An integrated framework on characterization, control, and testing of an electrical turbocharger assist," *IEEE Transactions on Industrial Electronics*, vol. 65, no. 6, pp. 4897–4908, 2018.

[79] R. Aymanns, T. Uhlmann, C. Nebbia, and T. Plum, "Electric supercharging new opportunities with higher system voltage," *MTZ worldwide*, vol. 75, no. 7-8, pp. 4–11, 2014.

[80] B. Xiao, E. Hellstrom, T. Kelly, T. Stolzenfeld, D. Bell, M. Jankovic, J. Buckland, and J. Rollinger, "Dynamic pressure ratio allocation for electric supercharger and turbocharger coordination," in *2018 Annual American Control Conference (ACC)*, pp. 2455–2460, IEEE, 2018.

[81] Y. Liu, Y.-Y. Wang, and M. Canova, "Distributed model predictive control of an electrically boosted diesel engine air path system," in *2018 Annual American Control Conference (ACC)*, pp. 2461–2466, IEEE, 2018.

[82] J. B. Heywood *et al.*, *Internal combustion engine fundamentals*. Mcgraw-hill New York, 1988.

[83] N. Watson and K. Banisoleiman, "A variable–geometry turbocharger control system for high output diesel engines," *SAE transactions*, pp. 152–167, 1988.

[84] X. Fang, W. Chen, Z. Zhou, and Y. Xu, "Empirical models for efficiency and mass flow rate of centrifugal compressors," *International journal of refrigeration*, vol. 41, pp. 190–199, 2014.

[85] K. Song, D. Upadhyay, H. Sun, H. Xie, and G. Zhu, "A physics-based control-oriented model for compressor mass flow rate," in *2016 IEEE 55th Conference on Decision and Control (CDC)*, pp. 6733–6738, IEEE, 2016.

[86] N. S. Nise, *Control systems engineering*. John Wiley & Sons, 2007.